

Clemson University

TigerPrints

All Theses

Theses

5-2022

Near-Earth Ion Irradiation Effects on Functional Ceramic Materials: A Combined Experimental-Monte Carlo Approach

William J. Sands
wsands@clemson.edu

Follow this and additional works at: https://tigerprints.clemson.edu/all_theses



Part of the [Ceramic Materials Commons](#), and the [Semiconductor and Optical Materials Commons](#)

Recommended Citation

Sands, William J., "Near-Earth Ion Irradiation Effects on Functional Ceramic Materials: A Combined Experimental-Monte Carlo Approach" (2022). *All Theses*. 3754.

https://tigerprints.clemson.edu/all_theses/3754

This Thesis is brought to you for free and open access by the Theses at TigerPrints. It has been accepted for inclusion in All Theses by an authorized administrator of TigerPrints. For more information, please contact kokeefe@clemson.edu.

Clemson University

TigerPrints

All Theses

Theses

5-2022

Near-Earth Ion Irradiation Effects on Functional Ceramic Materials: A Combined Experimental-Monte Carlo Approach

William Sands

Follow this and additional works at: https://tigerprints.clemson.edu/all_theses



Part of the [Ceramic Materials Commons](#), and the [Semiconductor and Optical Materials Commons](#)

NEAR-EARTH ION IRRADIATION EFFECTS ON FUNCTIONAL CERAMIC MATERIALS:
A COMBINED EXPERIMENTAL-MONTE CARLO APPROACH

A Thesis
Presented to
the Graduate School of
Clemson University

In Partial Fulfillment
of the Requirements for the Degree
Master of Science
Materials Science and Engineering

by
William Joseph Sands
May 2022

Accepted by:
Dr. Luiz G. Jacobsohn, Committee Chair
Dr. Rajendra Bordia
Dr. Ming Tang

ABSTRACT

The near-Earth space radiation environment is a complex system that creates a harmful environment for materials to operate in. Motivated by the search for using optical defects as an indicator of radiation damage, five single-crystal functional ceramic materials were selected to undergo ion irradiation at conditions found in the near-Earth space environment. Due to the complex nature of ion irradiation effects in ceramic materials, a host of calculations and experimental characterization methods were used. Calculations using the 2013 SRIM code were used to evaluate the ion projected range and the type and number of defects (vacancies) created by ion irradiation. Structural characterization by Raman spectroscopy was combined with results from UV-visible spectroscopy, radioluminescence, and thermoluminescence to determine changes induced by ion irradiation. This work revealed that the structure and optical properties are sensitive to ion irradiation and can be experimentally characterized by the methods used.

ACKNOWLEDGEMENTS

More than anyone, I would like to thank my advisor Dr. Luiz Jacobsohn for his teaching, guidance, and assistance throughout my graduate studies here at Clemson University. I greatly appreciate his willingness and eagerness to answer any of the questions that I have to further my understanding in the field of Materials Science. I would also like to thank my committee members Dr. Ming Tang and Dr. Rajendra Bordia for their advice and support in improving the content of this thesis. I am also appreciative of Kim Ivey for her support and advice, as well as the use of her lab space and equipment.

I would like to thank the entire Clemson Materials Science and Engineering department faculty and staff for their continued assistance and support during the duration of my studies.

I am grateful to my fellow group member, Robin Connor, for her advice, assistance, and friendship over the past year. I wish her the best of luck in her continued education and research.

Furthermore, I would like to thank Professor Lin Shao, Zhihan “Jimmy” Hu, and the faculty of the Accelerator Laboratory at Texas A&M for their support in this project.

Finally, I would like to thank both of my parents and Kelly Bevan. To my parents, you have always encouraged and supported me throughout my entire academic career, and I could not have made it this far without you. To Kelly Bevan, thank you for always believing in me and encouraging me after long days in the lab or writing.

This material is based upon work supported by the NASA South Carolina REAP Grant number 521383-RP-CM005.

TABLE OF CONTENTS

	Page
TITLE PAGE.....	i
ABSTRACT.....	ii
ACKNOWLEDGEMENTS.....	iii
LIST OF TABLES.....	ix
LIST OF FIGURES.....	xi
LIST OF EQUATIONS.....	xvi
CHAPTERS	
1. INTRODUCTION.....	1
1.1 – Near-Earth Orbit Radiation Environment.....	1
1.1.1 – Galactic Cosmic Radiation.....	5
1.1.2 – Solar Particle Events.....	7
1.1.3 – Trapped Particles.....	9
1.2 – Interactions Between Energetic Ions and Matter.....	10
1.2.1 – Penetration of Ions in Matter and the Projected Range of Ions.....	11
1.2.2 – Nuclear Stopping Power.....	12
1.2.3 – Electronic Stopping Power.....	13
1.2.4 – Straggling.....	14
1.2.5 – The Primary Knock-On Atom.....	14
1.2.6 – Displacement per Atom.....	17
1.2.7 – Displacement Threshold.....	17
1.2.8 – Radiation Damage Models.....	18

Table of Contents (continued)

	Page
1.3 – Ion Irradiation Damage Effects.....	20
1.3.1 – Displacement Damage.....	21
1.3.2 – Sputtering Effects.....	21
1.3.3 – Amorphization.....	22
1.4 – Motivation.....	23
2. EXPERIMENTAL PROCEDURES.....	25
2.1 – Materials.....	25
2.2 – Computational and Experimental Characterization Methods.....	30
2.2.1 – Computational Calculations.....	31
2.2.2 – Raman Spectroscopy.....	33
2.2.3 – UV-Visible Optical Spectroscopy.....	36
2.2.4 – Radioluminescence.....	39
2.2.5 – Thermoluminescence.....	42
3. 2013 SRIM MONTE CARLO RESULTS AND DISCUSSION.....	47
3.1 – Projected Range of Ions.....	47
3.2 – Sputtering Effects.....	48
3.3 – Damage Created by Ion Irradiation.....	50
4. MAGNESIUM ALUMINATE SPINEL RESULTS AND DISCUSSION.....	53
4.1 - 2013 SRIM Calculations.....	53
4.1.1 - Calculated Range of Ions.....	53
4.1.2 - Nuclear and Electronic Energy Loss.....	54

Table of Contents (continued)

	Page
4.1.3 - Damage Depth Distribution.....	55
4.2 - Raman Spectroscopy.....	56
4.3 - UV-Visible Spectroscopy.....	59
4.4 – Radioluminescence.....	62
4.5 – Thermoluminescence.....	64
4.6 - Summary of Results.....	68
5. YTTRIUM ALUMINUM GARNET RESULTS AND DISCUSSION.....	69
5.1 - 2013 SRIM Calculations.....	69
5.1.1 - Calculated Range of Ions.....	69
5.1.2 - Nuclear and Electronic Energy Loss.....	70
5.1.3 - Damage Depth Distribution.....	71
5.2 - Raman Spectroscopy.....	72
5.3 - UV-Visible Spectroscopy.....	75
5.4 – Radioluminescence.....	76
5.5 – Thermoluminescence.....	78
5.6 - Summary of Results.....	82
6. ZINC OXIDE RESULTS AND DISCUSSION.....	83
6.1 - 2013 SRIM Calculations.....	83
6.1.1 - Calculated Range of Ions.....	83
6.1.2 - Nuclear and Electronic Energy Loss.....	84
6.1.3 - Damage Depth Distribution.....	85

Table of Contents (continued)

	Page
6.2 - Raman Spectroscopy.....	86
6.3 - UV-Visible Spectroscopy.....	89
6.4 – Radioluminescence.....	91
6.5 – Thermoluminescence.....	93
6.6 - Summary of Results.....	96
7. YTTRIUM VANADATE RESULTS AND DISCUSSION.....	97
7.1 - 2013 SRIM Calculations.....	97
7.1.1 - Calculated Range of Ions.....	97
7.1.2 - Nuclear and Electronic Energy Loss.....	98
7.1.3 - Damage Depth Distribution.....	99
7.2 - Raman Spectroscopy.....	100
7.3 - UV-Visible Spectroscopy.....	103
7.4 – Radioluminescence.....	104
7.5 - Thermoluminescence.....	106
7.6 - Summary of Results.....	108
8. LITHIUM NIOBATE RESULTS AND DISCUSSION.....	109
8.1 - 2013 SRIM Calculations.....	109
8.1.1 - Calculated Range of Ions.....	109
8.1.2 - Nuclear and Electronic Energy Loss.....	110
8.1.3 - Damage Depth Distribution.....	111
8.2 - Raman Spectroscopy.....	112

Table of Contents (continued)

	Page
8.3 - UV-Visible Spectroscopy.....	115
8.4 – Radioluminescence.....	116
8.5 – Thermoluminescence.....	117
8.6 - Summary of Results.....	120
9. SUMMARY, CONCLUSIONS, AND FUTURE WORK.....	121
REFERENCES.....	123

LIST OF TABLES

Table		Page
1.1	Range of near-Earth orbital regions from Earth's surface.....	2
1.2	Summary of the near-Earth radiation environment sources.....	3
1.3	Displacement energies for common ceramic materials.....	18
2.1	Summary of physical properties of ceramic materials investigated in this work.....	25
2.2	Sample irradiation conditions.....	29
2.3	Parameters for obtaining Raman spectra of all samples.....	35
2.4	Additional parameters for UV-Vis spectroscopy.....	39
2.5	RL spectra integration time by crystal.....	41
2.6	X-ray irradiation time for TL measurements by material.....	44
2.7	Experimental parameters for TL spectroscopy measurements.....	45
3.1	Projected range of ions [μm] from 2013 SRIM calculations.....	48
3.2	Number of monolayers removed due to sputtering.....	49
3.3	Total dpa and the contribution of the element most contributing to vacancy creation.....	51
4.1	Differentiating moving and stopped MgAl_2O_4 atoms by color.....	53
4.2	Changes in peak position and FWHM for MgAl_2O_4 Raman spectra.....	58
4.3	Intensity ratio of RL peaks in pristine and irradiated MgAl_2O_4 samples.....	63
4.4	Intensity ratio of TL peak I to peak II for MgAl_2O_4 samples.....	65
5.1	Differentiating moving and stopped $\text{Y}_3\text{Al}_5\text{O}_{12}$ atoms by color.....	69
5.2	Identification of the vibrational modes of $\text{Y}_3\text{Al}_5\text{O}_{12}$	73

List of Tables (continued)

	Page
5.3 Changes in the peak location and peak FWHM for $Y_3Al_5O_{12}$ Raman spectra.....	74
5.4 Peak (P) and shoulder (S) temperatures observed in the glow curve of $Y_3Al_5O_{12}$ in this work.....	79
5.5 Intensity ratio of glow curve peaks in pristine and irradiated $Y_3Al_5O_{12}$ samples.....	79
6.1 Differentiating moving and stopped ZnO atoms by color.....	83
6.2 Detected vibrations from Raman in all ZnO samples.....	87
6.3 Changes in peak position and FWHM for ZnO Raman spectra.....	88
6.4 Intensity ratio of TL peaks for ZnO samples.....	94
7.1 Differentiating moving and stopped YVO_4 atoms by color.....	97
7.2 Detected vibrational modes from Raman in all YVO_4 samples.....	101
7.3 Changes in peak position and FWHM for YVO_4 Raman spectra.....	102
8.1 Differentiating moving and stopped $LiNbO_3$ atoms by color.....	109
8.2 Identified Raman vibrations of $LiNbO_3$	113
8.3 Changes of the Raman peak position and FWHM for irradiated $LiNbO_3$	114

LIST OF FIGURES

Figure		Page
1.1	Different types of radiation including origin and location around the near-Earth orbital environment.....	3
1.2	Transistor that has failed due to a heavy-ion induced SEE.....	4
1.3	Arc damage sustained from ESD on the EURECA satellite solar panel.....	4
1.4	Solar cycle effect on the GCR energy spectrum for hydrogen, helium, oxygen, and iron.....	6
1.5	Calculations of the integral fluence-energy spectra for protons, alpha particles, oxygen, iron, and summed spectra for $Z > 28$ elements.....	8
1.6	Several severe solar proton event energy spectra in solar cycles 19-22.....	8
1.7	Omnidirectional integrated proton and electron fluxes.....	10
1.8	An ion incident on a semiconductor.....	11
1.9	Electronic, nuclear, and total energy loss as a function of ion energy for O^+ ion irradiation of $MgAl_2O_4$	12
1.10	Snapshots of a molecular dynamics computer simulation of a collision cascade in Au induced by a 10 keV Au self-recoil.....	15
1.11	Displacement cascade model.....	16
1.12	2013 SRIM calculation of 10,000 1 MeV O^+ irradiation-induced damage distributions as a function of penetration depth.....	20
1.13	Primary radiation damage events in materials.....	21
1.14	Temperature dependence of amorphization dose of 1.5 MeV Xe^+ irradiation for indicated phases.....	23
2.1	Complete ensemble of samples investigated in this work.....	27
2.2	General view of the Accelerator Laboratory at TAMU.....	28
2.3	Iono-luminescence of the crystals under ion irradiation.....	30

List of Figures (continued)

	Page
2.4 Rastering of H_2^+ beam onto crystals and consequent iono-luminescence.....	30
2.5 Example of 2013 SRIM setup window for 60 keV H^+ irradiation of $MgAl_2O_4$	32
2.6 Raman spectra of H^+ irradiated $Y_3Al_5O_{12}$ with neon lamp line reference.....	34
2.7 Raman spectrometer setup with neon lamp reference.....	36
2.8 UV-Vis Spectrometer and stage.....	37
2.9 Optical absorption spectrum of pristine ZnO crystal.....	38
2.10 RL spectra of H^+ irradiated ZnO.....	40
2.11 Photograph of the Freiburg Instruments Lexsyg spectrofluorometer and sample wheel.....	42
2.12 Glow curve of the pristine $Y_3Al_5O_{12}$ crystal.....	43
2.13 TL spectra of pristine $Y_3Al_5O_{12}$ crystal.....	46
4.1 Ion trajectories in $MgAl_2O_4$ calculated using 2013 SRIM.....	53
4.2 Electronic, nuclear, and total energy loss in $MgAl_2O_4$	54
4.3 Damage depth distribution of a) H^+ , b) He^+ and c) O^+ ion irradiations in $MgAl_2O_4$	55
4.4 Raman spectra of pristine and irradiated $MgAl_2O_4$ samples offset by intensity.....	56
4.5 Overlay of pristine and irradiated $MgAl_2O_4$ Raman spectra after normalization and correction.....	58
4.6 Optical absorption spectra of pristine and irradiated $MgAl_2O_4$ samples.....	60
4.7 Offset RL spectra of pristine and irradiated $MgAl_2O_4$ samples.....	62
4.8 Glow curves of pristine and irradiated $MgAl_2O_4$ samples.....	64
4.9 TL spectroscopy results of pristine $MgAl_2O_4$	66

List of Figures (continued)

	Page
4.10 TL reproducibility measurements of pristine MgAl ₂ O ₄	67
5.1 Ion trajectories in Y ₃ Al ₅ O ₁₂ calculated using 2013 SRIM.....	69
5.2 Electronic, nuclear, and total energy loss in Y ₃ Al ₅ O ₁₂	70
5.3 Damage depth distribution for a) H ⁺ , b) He ⁺ , and c) O ⁺ ion in Y ₃ Al ₅ O ₁₂	71
5.4 Raman spectra of pristine and irradiated Y ₃ Al ₅ O ₁₂ samples offset by Intensity.....	72
5.5 Overlay of pristine and irradiated Y ₃ Al ₅ O ₁₂ Raman spectra after normalization and position correction.....	74
5.6 Optical absorption spectra of pristine and irradiated Y ₃ Al ₅ O ₁₂ samples.....	75
5.7 Offset RL spectra for pristine and irradiated Y ₃ Al ₅ O ₁₂ samples.....	77
5.8 Glow curves of pristine and irradiated Y ₃ Al ₅ O ₁₂ samples.....	78
5.9 TL spectroscopy results of pristine Y ₃ Al ₅ O ₁₂	80
5.10 TL reproducibility measurements of pristine Y ₃ Al ₅ O ₁₂	82
6.1 Ion trajectories in ZnO calculated using 2013 SRIM.....	83
6.2 Electronic, nuclear, and total energy loss in ZnO.....	84
6.3 Damage depth distribution of a) H ⁺ , b) He ⁺ and c) O ⁺ ion irradiations in ZnO.....	85
6.4 Raman spectra of pristine and irradiated ZnO samples offset by Intensity.....	86
6.5 Overlay of selected Raman bands of pristine and irradiated ZnO Raman spectra after position correction and normalization at 440cm ⁻¹	88
6.6 Optical absorption spectra of pristine and irradiated ZnO samples.....	90
6.7 Offset RL spectra of pristine and irradiated ZnO samples.....	91

List of Figures (continued)

	Page
6.8	Glow curves of the pristine and irradiated ZnO samples..... 93
6.9	TL spectroscopy results of pristine ZnO..... 94
6.10	TL reproducibility measurements of pristine ZnO..... 95
7.1	Ion trajectories in YVO ₄ calculated using 2013 SRIM..... 97
7.2	Electronic, nuclear, and total energy loss in YVO ₄ 98
7.3	Damage depth distribution of a) H ⁺ , b) He ⁺ and c) O ⁺ ions in YVO ₄ 99
7.4	Raman spectra of pristine and irradiated YVO ₄ samples offset by Intensity..... 100
7.5	Overlay of pristine and irradiated YVO ₄ Raman spectra after normalization and position correction..... 102
7.6	Optical absorption spectra of pristine and irradiated YVO ₄ samples..... 103
7.7	Offset RL spectra of pristine and irradiated YVO ₄ samples..... 105
7.8	Glow curves of pristine and irradiated YVO ₄ samples..... 106
7.9	TL spectroscopy results of pristine YVO ₄ 107
7.10	TL reproducibility measurements of pristine YVO ₄ 108
8.1	Ion trajectories in LiNbO ₃ calculated using 2013 SRIM..... 109
8.2	Electronic, nuclear, and total energy loss in LiNbO ₃ 110
8.3	Damage depth distribution of a) H ⁺ , b) He ⁺ and c) O ⁺ ion irradiations in LiNbO ₃ 111
8.4	Raman spectra of pristine and irradiated LiNbO ₃ samples offset by Intensity..... 112
8.5	Overlay of pristine and irradiated LiNbO ₃ Raman spectra after normalization and position correction..... 114
8.6	Optical absorption spectra of pristine and irradiated LiNbO ₃ samples..... 115

List of Figures (continued)

	Page
8.7 Offset RL spectra for pristine and irradiated LiNbO ₃ samples.....	117
8.8 Glow curves of pristine and irradiated LiNbO ₃ samples.....	118
8.9 TL spectroscopy results of pristine LiNbO ₃	119
8.10 TL reproducibility measurements of pristine LiNbO ₃	120

LIST OF EQUATIONS

Equation	Page
1.1 Range of ions in solids.....	11
1.2 Total stopping power.....	11
1.3 Reduced energy for nuclear stopping power.....	13
1.4 Nuclear stopping power for $\epsilon \leq 30$	13
1.5 Nuclear stopping power for $\epsilon > 30$	13
1.6 Electronic stopping power.....	13
1.7 Calculation of dpa.....	17
1.8 Kinchin-Pease model derivation for $T < E_d$	19
1.9 Kinchin-Pease model derivation for $E_d < T < 2.5 E_d$	19
1.10 Kinchin-Pease model derivation for $2.5 E_d < T < E_c$	19
1.11 Kinchin-Pease model derivation for $T \geq E_c$	19
2.1 Induced dipole moment.....	33
2.2 Beer-Lambert's law.....	37
2.3 Absorption intensity from transmittance.....	37
3.1 Crystalline atomic density per monolayer.....	49
3.2 Removal of atomic layers from sputtering.....	49
3.3 Energy transferred from nuclear collisions.....	51
4.1 Rayleigh scattering of light.....	61

CHAPTER ONE

INTRODUCTION

In the last century, human exploration past Earth's atmosphere and into "the final frontier" has resulted in major scientific discoveries about our neighboring planets and the entire universe. Explorations into space have also supported important technological advances such as computerized axial tomography (CAT) scanners, wireless headsets, and light-emitting diode (LED) technology.¹ However, the conditions in space produce one of the most harmful and dangerous habitats for both electronics and humans to survive.^{2,3} These harmful conditions are largely due to the extreme radiation conditions surrounding the Earth's atmosphere.⁴

Before the era of space exploration began, humanity had little evidence for the presence of radiation in space, such as the ionized tails of comets and the aurora borealis.⁵ Then, the beginning of the space exploration era in 1958 resulted in the discovery of the Van Allen Belts surrounding Earth, containing high energy charged particles.^{5,6,7} Beyond the natural protection offered by the Earth's atmosphere, various radiation environments exist wherein different types of radiation can be encountered with different origins and distributions.⁸⁻¹⁰ These radiation environments can result in the disruption of electronic systems and also cause radiobiological hazards for humans on manned space flights.^{5,11}

1.1– Near-Earth Orbit Radiation Environment

For the scope of this research, we will focus on the radiation conditions found in the near-Earth orbit environment. The near-Earth orbit is described in terms of three different regions, which include low-Earth orbit (LEO), middle-Earth orbit (MEO), and geostationary orbit (GEO).

Differentiation of these radiation environments is done in terms of the orbital distance from the Earth’s surface, and the altitudes used to represent the different orbits are shown in *Table 1.1*.¹² As further references, the Earth’s radius is roughly 6,400 km¹³, the nearly circular orbit of the international space station (ISS) has a mean altitude of 400 km¹⁴ (LEO), and geostationary satellites orbit at a mean altitude of 36,000 km above Earth’s equator¹⁵ (GEO).

Table 1.1: Range of near-Earth orbital regions from Earth’s surface.¹²

Low-Earth Orbit (LEO)	Middle-Earth Orbit (MEO)	Geostationary Orbit (GEO)
200 – 2,000 km	2,000 – 32,000 km	32,000 – 38,000 km

In order to better understand the near-Earth orbit radiation environment, each source of particle radiation will be examined and their individual contributions to the total radiation damage evaluated. The radiation environment in the near-Earth orbit results from a combined effect of galactic cosmic radiation (GCR), solar particle events (SPE), and trapped particles in the Van Allen Belts (also known as ‘radiation belts’).^{3-6,16} Each of these sources contribute to the radiation damage that impacts satellite electronics and harms astronauts in the near-Earth space environments.¹⁷ They are discussed in the next sections, and a summary of the characteristic of radiation sources in the near-Earth orbit can be found in *Table 1.2*.^{4,5,9} A diagram illustrating the different types of radiation and their location around the Earth is shown in *Figure 1.1*.¹⁸

Table 1.2: Summary of the near-Earth radiation environment sources.^{4,5,9,16}

Radiation Category		Composition	Energies	Max Flux/ Fluence
GCRs		Protons (87%) Alphas (12%) Heavier elements (1%)	Up to $\sim 10^{11}$ GeV Most probable ~ 1 GeV Most probable ~ 1 GeV/nucleon	10/cm ² /s (total)
SPEs	Solar Flares	Electron-rich	Up to 100 MeV	---
	CMEs	Protons 96.4% Alphas 3.5% Heavier atoms 0.1%	0.1 – 100 MeV 0.1 – 100 MeV 0.1 – 100 MeV/nucleon	$\sim 10^5$ /cm ² /s
Radiation Belts		Protons 95%	1 keV – 500 MeV	$\sim 10^5$ /cm ² /s
		Electrons	1 keV – 10 MeV	$\sim 10^6$ /cm ² /s

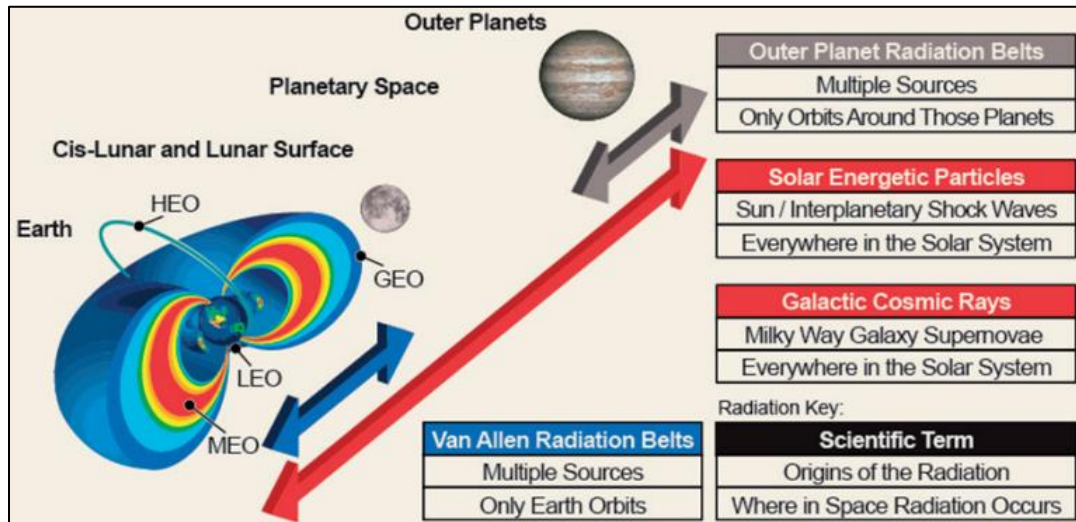


Figure 1.1: Different types of radiation including origin and location around the near-Earth orbital environment.¹⁸

Effects of space radiation on materials can be classified in different categories: i) transient effects such as single event effects (SEE), ii) cumulative effects including total ionizing dose (TID) and displacement damage (DD), and iii) charging and electrostatic discharges (ESD).⁵ Some of these effects are illustrated in *Figure 1.2*¹⁹ and *1.3*²⁰. In this work, we will focus on displacement

damage created by ion irradiation. This is of relevance since displacement damage can affect microelectronics and the performance of semiconductor devices in space.²¹⁻²² For example, atomic displacements can degrade solar cells performance by increasing their resistance and thus reducing their capacity for power generation.²²⁻²⁶

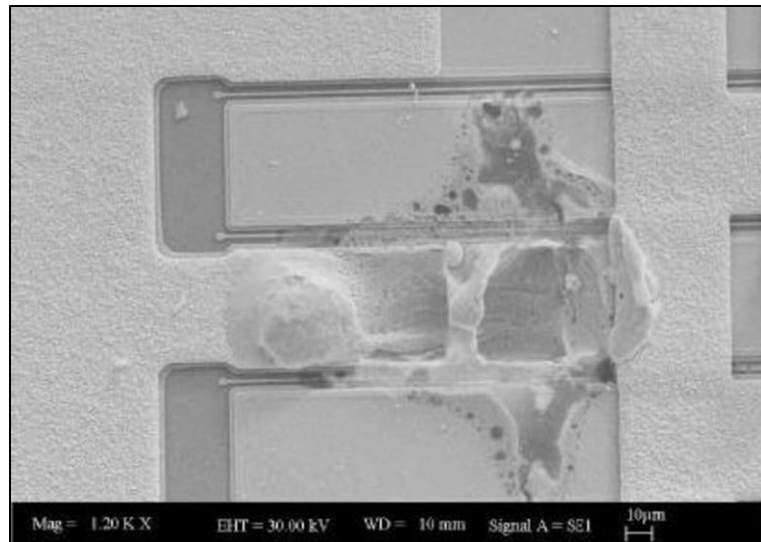


Figure 1.2: Close up of a transistor that has catastrophically failed due to a heavy-ion induced SEE. The track melted due to an unwanted high current situation caused by the charge of the heavy ion inducing a runaway short circuit or “latch-up”.¹⁹

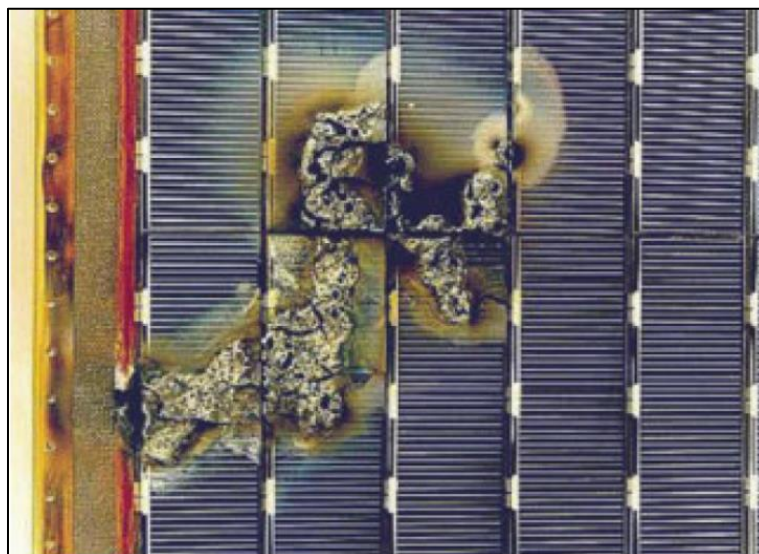


Figure 1.3: Arc damage sustained from ESD on the EURECA satellite solar panel.²⁰

1.1.1 – Galactic Cosmic Radiation

GCRs originate from outside our solar system and correspond to the low-level flux of highly energetic ions seen in interplanetary space and near-Earth orbit.^{4,5} They are believed to be created from stars exploding in the Milky Way and are carried by the shock waves of the collapse throughout the interstellar medium.⁵ The GCR spectrum is composed of protons (ionized hydrogen, $Z = 1$) at an abundance of $\sim 87\%$ and ionized helium ($Z = 2$) at an abundance of $\sim 12\%$, with the ions from lithium ($Z = 3$) to nickel ($Z = 28$) at an abundance of almost 1% .^{5,27} Higher atomic mass elements ($Z > 28$) are also present, but only account for 0.00003% of collected GCR particles.^{4-6,27} The energy of GCR particles range from around 1 MeV/nucleon to more than $10^{14} \text{ MeV/nucleon}$.^{16,18}

In the near-Earth radiation environment, GCRs are believed to have an isotropic distribution with a maximum energy peak of 1 GeV/nucleon (*Figure 1.4*).¹⁶ For GCRs with energies less than 10 GeV/nucleon , the Sun's 11-year cycle will affect the resulting flux due to the increase of emitted solar flares and coronal mass ejections.^{16,28} As the solar winds become calmer due to fewer emissions of solar flares, GCRs are able to propagate further into the inner solar system due to less interference from the Sun and penetrate the Earth's atmosphere easier.¹⁸ This phenomenon is inversely affected by the solar cycle, decreasing the penetration of GCR's with the increase of emitted solar radiation as shown in *Figure 1.4*.^{16,29}

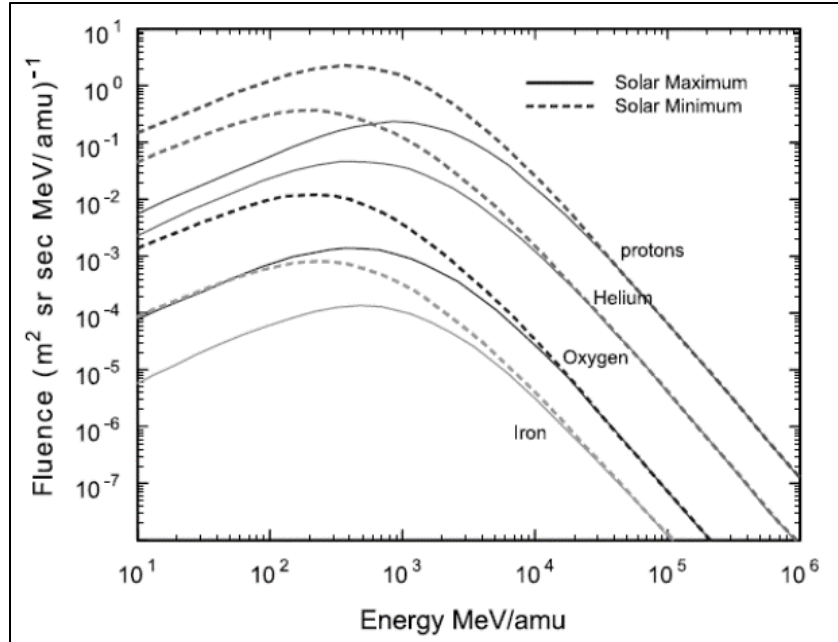


Figure 1.4: Solar cycle effect on the GCR energy spectrum for hydrogen, helium, oxygen, and iron.¹⁶

GCR spectra in the LEO differ from the spectra in MEO and GEO space environments due to the deflection of the low-energy GCR particles by the Earth's magnetic field.^{16,27} A maximum energy of around 1 GeV/nucleon is observed, with flux variations depending on the energy of the particles. The charged particles tend to follow the Earth's geomagnetic field lines allowing deeper penetration at the Earth's poles and minimal amounts at the equator.²⁷ Interestingly, although the contribution of heavy ions to GCR radiation is only 1%, their influence on electronics and humans is often more significant than that of the protons and helium.⁴ Due to their high energies, difficult to obtain experimentally, and low fluxes, the effect of GCRs in the near-Earth space will not be studied in this work.

1.1.2 – Solar Particle Events

Solar particle events (SPEs) refers to two distinct categories of events that accelerate charged particles in different manners throughout the solar system: solar flares and coronal mass ejections (CMEs cf. *Table 1.2*).^{4,5,18} Solar flares are dominated by electrons with energies up to 100 MeV³⁰ and thus not of relevance to this work. The second category refers to CMEs, which occur from large plasma eruptions on the surface of the Sun that drive shock waves outward.⁴ They are the primary SPE responsible for the major geomagnetic disturbances at Earth when impacting the magnetic field and disturbances in interplanetary space.⁵ CMEs have been determined to be most active during the period of maximum solar activity resulting in a phenomenon known as space weather.³¹ These events have been observed to last for several days at a time and are typically proton rich in particle emissions with small contents of ³He.^{4,31} They can reach speeds of up to 3000 km/s, resulting in an impact with the Earth's magnetic field after only 12 hours after emission.^{4,5,31,32} These events are spontaneous and continuous, with their probability increasing during the maximum of solar activity from the solar cycle.^{5,30} Relative measurements of the composition of CMEs, shown in *Figure 1.5*⁴, reveal that they contain roughly 96.4% protons, 3.5% alpha particles, and <0.1% heavier ions.^{4,5} The energies of these CMEs are typically around 0.1 - 100 MeV/nucleon with peak fluences higher than 10¹² cm⁻² ^{4,5,31,32}, similar to the ion irradiation conditions used in this work.

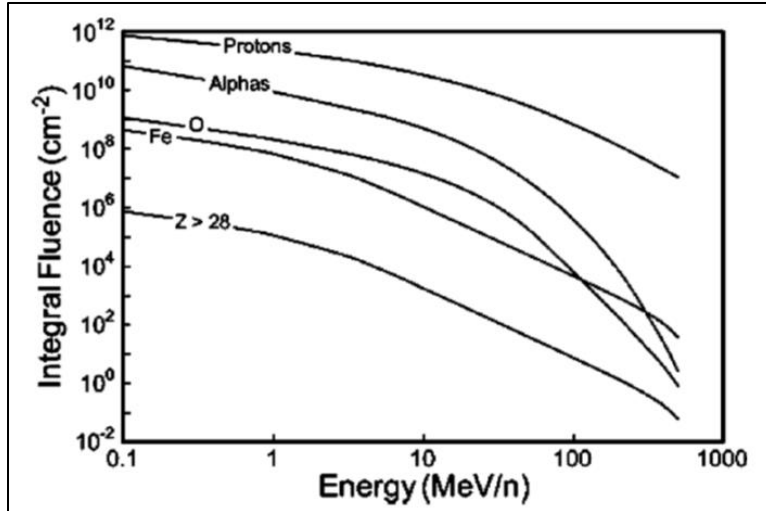


Figure 1.5: Calculations of the integral fluence-energy spectra for protons, alpha particles, oxygen, iron, and summed spectra for $Z > 28$ elements.⁴

Severe SPE events occur once or twice per solar cycle with possible proton fluences greater than $10^{10}/\text{cm}^2$.^{16,33} Several of these phenomena are illustrated in *Figure 1.6*.⁴

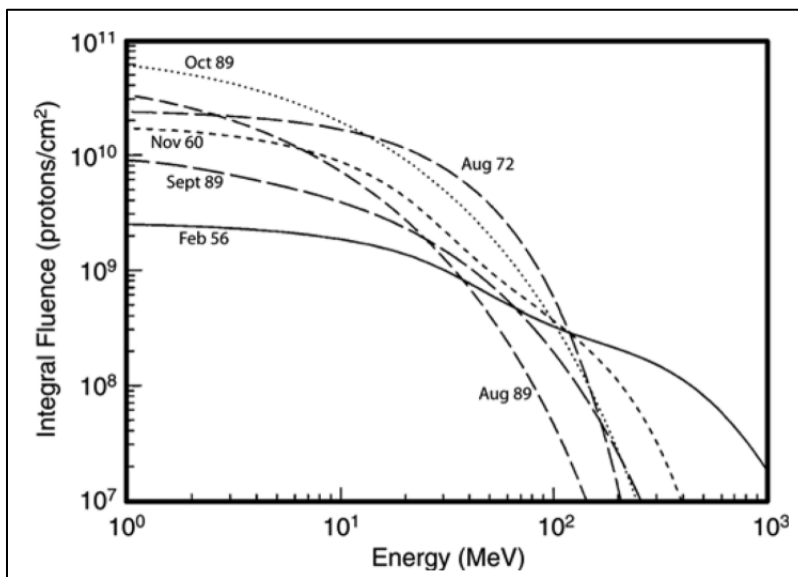


Figure 1.6: Several severe solar proton event energy spectra in solar cycles 19-22. Curves labeled with the event month and year.⁴

1.1.3 – Trapped Particles

Surrounding the Earth are regions of magnetically trapped energetic particles, mostly electrons and protons, known as the Van Allen Belts that were first discovered by the Explorer 1 satellite in 1958.^{4,5,34} As shown in *Figure 1.1*¹⁸ and *Figure 1.7*³⁴, there are two main belts, with the inner belt being within altitudes from 1,000 to 12,000 km (within LEO and MEO) and the outer belt within 13,000 to 60,000 km (within MEO and GEO). In these belts, the trapped energetic particles move up and down along magnetic field lines while simultaneously drifting around the Earth. The particle drift generates an electrical current known as the "ring current". Interestingly, electromagnetic radiation can free some of the trapped particles that precipitate down the magnetic field lines into the ionosphere around the magnetic poles creating the auroras (polar lights).

The energies of these particles range from 1 keV to 10 MeV for electrons and 1 keV to 500 MeV for protons^{4,5} with the outer belt being composed essentially by electrons and the inner belt by protons, electrons and, to a minor extent, ionized He, O and other elements. Protons constitute 95% of the radiation belts and the contribution of the other ions depend on their altitude, energy, and the magnitude of the magnetic field.⁹ Due to the tilt of the Earth's dipole, the inner radiation belt dips to a low altitude in the South Atlantic possibly affecting satellites in the LEO.^{5,34} The outer region belt, which extends up to and past GEO, is more complex and varies due to influences from CMEs and the solar cycle.³⁴

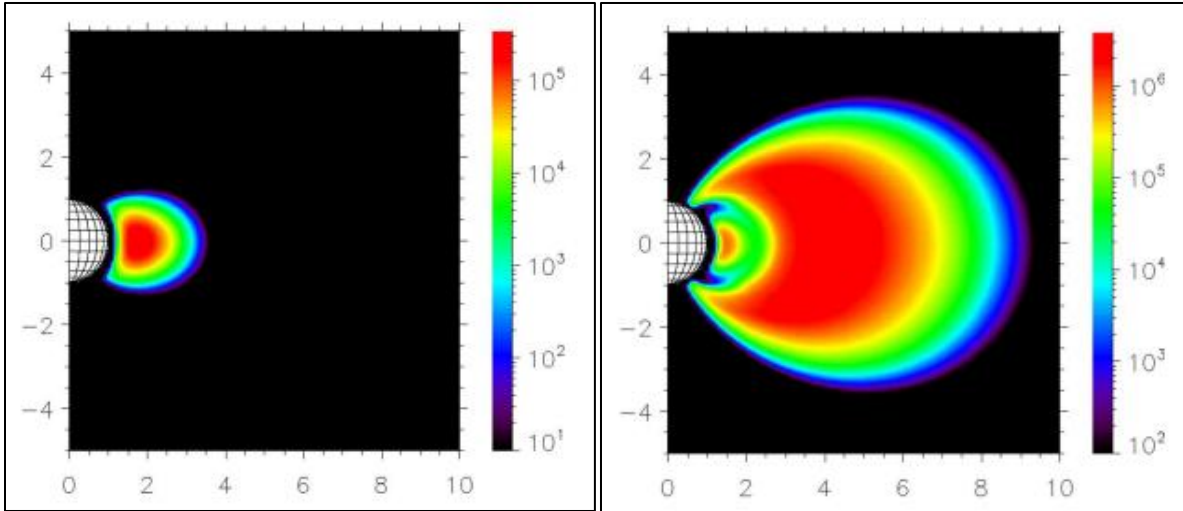


Figure 1.7: a) Omnidirectional integrated proton fluxes and b) Omnidirectional integrated electron fluxes as a function of earth radii (energy >1 MeV).³⁴

In this work, we will restrict the investigation to ion irradiation displacement damage focusing on the most common ions found in the near-Earth orbital environment: H^+ and He^+ , while using O^+ as a representative for the heavier elements (*cf. Table 1.2* and *Figures 1.4* and *1.5*).^{4,5,9,16}

1.2 – Interactions Between Energetic Ions and Matter

Interactions between energetic electrons and ions with crystal structures result in defects and imperfections³⁵ These defects can, in turn, produce changes in the physical, mechanical, and chemical properties of the material.^{35,36} In order to better understand the concept of radiation damage, the mechanisms of radiation damage caused by these particles and their corresponding effects will be discussed. Due to the scope of this research, we will mainly focus on the mechanisms related to energetic ions and their interactions with the crystalline structure of ceramic materials.

1.2.1 – Penetration of Ions in Matter and the Projected Range of Ions

The trajectory of ions in solids is conveniently described as a sequence of straight tracks where electronic energy loss occurs. These are separated by nuclear collisions, where nuclear energy loss and large angular deflection occur. The projected range of an ion refers to the average of the maximum depth that the incident ions reach in the material. However, since the path of the ions is not a straight line but a “zig-zag” trajectory due to nuclear collisions with the material’s atoms, the total path length is longer than the projected range.³⁷ In other words, the projected range corresponds to the projection of the total path on an axis perpendicular to the surface as illustrated in *Figure 1.8*.²¹

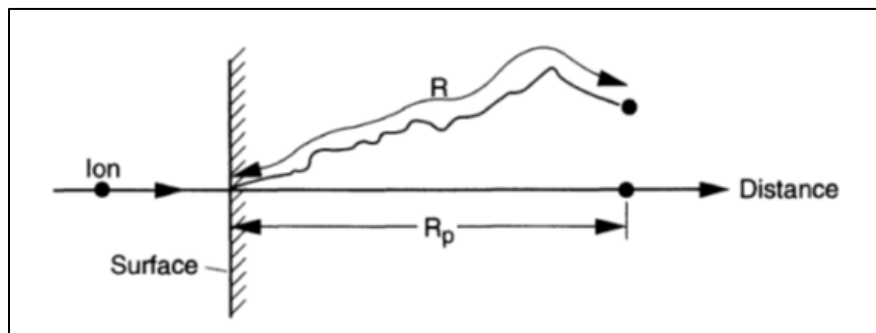


Figure 1.8: An ion incident on a semiconductor penetrates with a total path length R , which gives a projected range, R_p , along the direction parallel to the incident ion.²¹

The general expression³⁸ for the range of ions in solids is given by:

$$\Delta x = \int_0^{E_0} \frac{1}{S(E)} dE \quad (1.1)$$

where E_0 is the initial kinetic energy of the particle, Δx is the total distance traveled by the ion such that its final energy is zero, and $S(E)$ is the stopping power. The total stopping power³⁸ is given by:

$$S = S_n + S_e \quad (1.2)$$

where S_n is the nuclear stopping power and S_e is the electronic stopping power. The relative importance of these energy loss mechanisms (*i.e.*, electronic or nuclear) depends mostly on the velocity of the ion. For velocities lower than the velocity of the atomic electrons, nuclear energy loss dominates. For higher projectile velocities, electronic energy loss dominates. *Figure 1.9* illustrates S , S_n , and S_e , for the irradiation of magnesium aluminate spinel crystal by O^+ ions.

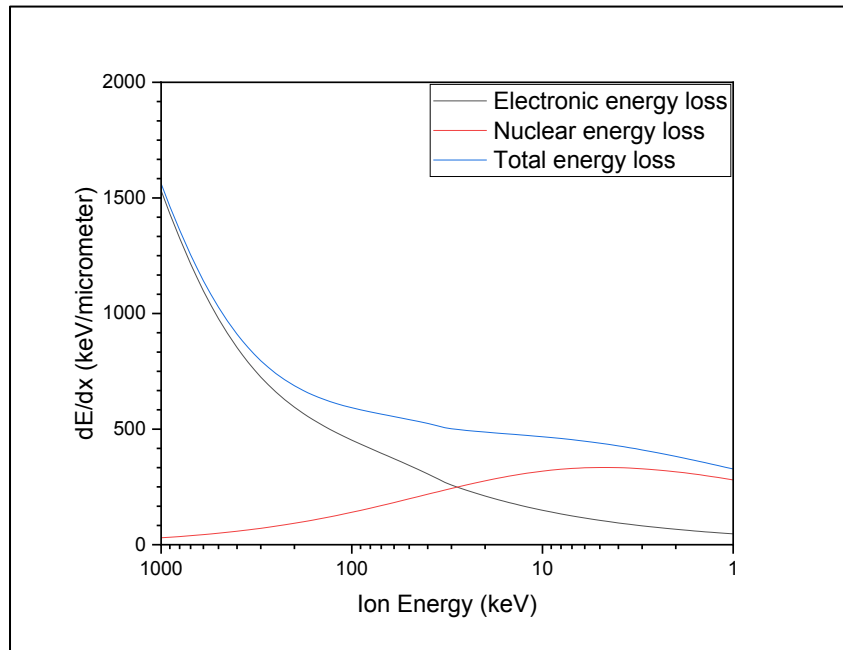


Figure 1.9: Electronic, nuclear, and total energy loss as a function of ion energy for O^+ ion irradiation of $MgAl_2O_4$.

1.2.2 – Nuclear Stopping Power

The nuclear stopping power (S_n) refers to the nuclear energy loss of the incident ion due to collisions with the target atoms.³⁷ These collisions cause large energy losses and considerable changes in the original trajectory (angular deflection) of the ion. This is the primary mechanism for the creation of damage in solids as it will be discussed later. An universal expression for determining the nuclear stopping power S_n can be given in terms of the reduced energy (ϵ):³⁷

$$\varepsilon = \frac{32.53 M_2 E_0}{Z_1 Z_2 (M_1 + M_2) (Z_1^{23} + Z_2^{23})} \quad (1.3)$$

where $Z_{1,2}$ and $M_{1,2}$ are the charges and masses of the ion and scattering atoms respectively. This then leads to the determination of the nuclear stopping power depending on the reduced energy.³⁷

$$\text{For } \varepsilon \leq 30: \quad S_n = \frac{\ln(1+1.1383\varepsilon)}{2(\varepsilon+0.01321\varepsilon^{0.21226} + 0.1959\varepsilon^{0.5})} \quad (1.4)$$

$$\text{For } \varepsilon > 30: \quad S_n = \frac{\ln(\varepsilon)}{2(\varepsilon)} \quad (1.5)$$

1.2.3 – Electronic Stopping Power

The electronic stopping power S_e refers to the energy loss of the incident ion due to inelastic collisions with atomic electrons.³⁷ In these collisions, the ion trajectory is not significantly changed. A material's electronic stopping power is calculated independently of its nuclear stopping power and assumes that each volume element of the solid target contains an independent electron cloud. The electron density in each individual volume depends on its location in relation to the nuclei, the chemical nature of the target elements, and the density of the material. The total electronic stopping power is the integral of all individual volume's stopping power given by:³⁷

$$S_e = \int I(v, \rho) (Z_1^*(v))^2 \rho dx^3 \quad (1.6)$$

where $I(v, \rho)$ is the stopping interaction function of the projectile of unit charge with velocity v and charge Z_l in an electron cloud of density, ρ . Since the electronic stopping power is integrated over the entire volume, it considers each density interaction by accounting for the probability of that density occurring in the solid.

1.2.4 – Straggling

Straggling refers to the variation of the ion range due to variations of energy loss of ions in the target material.³⁷ Straggling can be expressed in terms of longitudinal or lateral straggling. Longitudinal straggling refers to the deviation of the ions at a parallel plane relative to the incident beam, resulting in different distributions of penetration depth. Lateral straggling refers to the deviation of the ions at a normal plane relative to the incident beam, resulting in different distributions of penetration width.

1.2.5 – The Primary Knock-On Atom

The “primary knock-on atom” (PKA) typically refers to the first atom that is displaced by the incoming high-energy ion, usually at or near the surface of the material.³⁵ Depending on the energy transfer between the incident ion and the PKA, the PKA can then propagate throughout the structure and in turn create secondary knock-on atoms before stopping (*i.e.*, a collision cascade).^{35,36} A molecular dynamic simulation of a collision cascade is illustrated in *Figure 1.10*³⁹ (the whole video of the molecular dynamic simulation can be seen here: https://en.wikipedia.org/wiki/Collision_cascade). Noticeable is the remaining damage at the end of the simulation after all kinetic energy is dispersed.

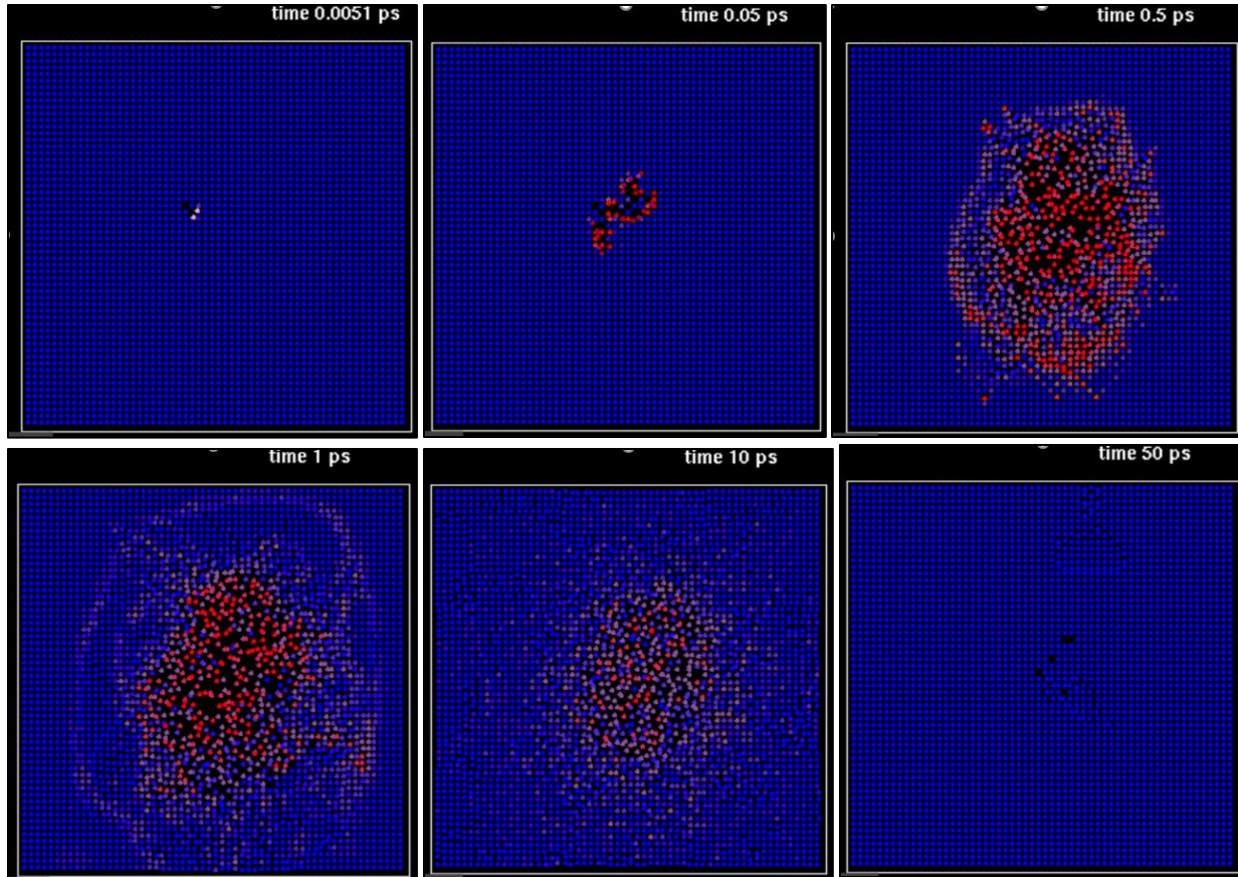


Figure 1.10: Snapshots of a molecular dynamics computer simulation of a collision cascade in Au induced by a 10 keV Au self-recoil.³⁹

This can result in the creation of multiple vacant lattice sites and agglomeration of point defects which are collectively known as a “displacement cascade”.³⁵ During these collision processes, thermal spikes may also be created by the nuclei entering into higher energy states at their lattice position. The idea of a “displacement cascade” then led to the creation of a displacement spike model, as shown in *Figure 1.11*. The model consists of the creation of several vacant sites, commonly referred to as depleted zones, surrounded by a higher number of interstitials.³⁵

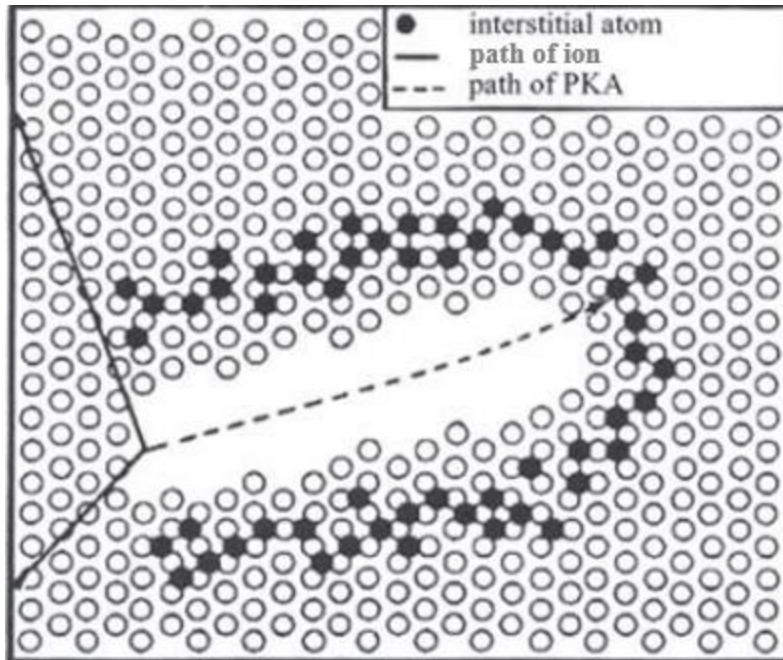


Figure 1.11: Displacement cascade model. Adapted from ref [35].

In summary, ion irradiation can lead to the formation of the following radiation defects in ceramic crystal structures:^{35,36,40}

- Vacancies
- Interstitials
- Impurity atoms – produced by transmutation
- Thermal spikes – resulting from atoms in high-energy states
- Displacement zones – contain displaced atoms, vacancies, and self-interstitials
- Voids – large regions containing no atoms
- Bubbles – voids stabilized by gases
- Replacement collisions – scattered interstitial atoms that fall into vacant sites

1.2.6 – Displacement per Atom

A useful and widespread measure of radiation damage is the “displacements per atom” (dpa). Dpa corresponds to the total number of atoms displaced from their original position due to interactions between incident ions and the target atoms and between the PKA and the target atoms.^{35,40} The dpa is calculated as the number of vacancies created, in addition to replacement collisions. A replacement collision occurs when the incident ion knocks a target atom out of its structure position. This target atom will then undergo more nuclear collisions with target atoms, until it transfers the remainder of its energy to knock out a similar target atom. Then, it can replace the target atom it knocked out, resulting in a correct arrangement in the structure but a change from initial position. Dpa serves as a unit of measurement for radiation damage and is affected by the material’s atomic density, structure, and ion fluence. A general expression for the calculation of dpa is given by:³⁷

$$dpa = \frac{\Phi N_d}{\rho} \quad (1.7)$$

where Φ is the ion fluence, N_d is the number of defects created, and ρ is the atomic density, *i.e.*, the number of atoms per volume unit. Dpa values were obtained from 2013 SRIM calculations as discussed later.

1.2.7 – Displacement Threshold

The displacement threshold or displacement energy (denoted by E_d) is defined as the minimum energy that must be transferred to displace an atom from its structure site and produce a stable defect.³⁵ E_d is affected by the location of the target atom and thus depends on the crystallographic plane containing that atom. The value of a crystallographic plane’s displacement energy depend on the mechanism of the momentum transfer, the trajectory of the PKA, the

crystallographic structure, and the thermal energy of the atoms.^{35,36,40} If the energy transferred to the lattice atom is lower than the displacement energy, the atom will not be removed from its equilibrium position.³⁵ Instead, the atom will vibrate around its equilibrium position, thereby transferring energy to neighboring and dissipating heat.^{35,36} *Table 1.3*⁴¹ illustrates elemental displacement energies for several common ceramic materials. For unknown thresholds, a general displacement energy of 25-40 eV can be used as an average of all of the displacement energies along different crystallographic planes in a given material.^{35,40} E_d values used in this work are discussed in Chapters 2 and 3.

Table 1.3: Displacement energies for common ceramic materials.⁴¹

Recommended threshold displacement energies in ceramics			
Material	Threshold displacement energy (eV)		Comments
Al ₂ O ₃	$E_d^{Al} \sim 20$	$E_d^O = 50$	previous 'standard' value for E_d^O was 76 eV
MgO	$E_d^{Mg} = 55$	$E_d^O = 55$	good agreement among five studies
MgAl ₂ O ₄		$E_d^O = 60$	only one known measurement
ZnO	$E_d^{Zn} \sim 50$	$E_d^O = 55$	moderate uncertainty in E_d^{Zn}
BeO	$E_d^{Be} \sim 25$	$E_d^O \sim 70 ?$	large uncertainty in data
UO ₂	$E_d^U = 40$	$E_d^O = 20$	only one known measurement
SiC	$E_d^{Si} \sim 40 ?$	$E_d^C = 20$	large uncertainty in E_d^{Si}
Graphite	$E_d^C = 30$		extensive data base
Diamond	$E_d^C = 40$		four known measurements

1.2.8 – Radiation Damage Models

Radiation damage models offer useful calculations in order to determine the amount of defects created by the source particle. The simplest model for calculating the number of atomic displacements due to an incident particle is known as the Kinchin-Pease model.^{35,42} In the model, the energy of the knock-on atoms is given as (T) with the number of atomic displacements represented as $\nu(T)$.^{35,42,43} Its basic assumptions are:^{35,37,43}

1. The cascade is created due to elastic collisions based on the hard sphere approximation.

2. Atomic displacements occur when $T > E_d$.
3. No energy is passed to the structure (only between incident ions and target atoms).
4. Energy loss by electronic stopping is calculated by an electronic cutoff energy (E_c) which is the maximum energy transferred from inelastic collisions.
5. Atomic arrangement is randomly orientated.
6. No annihilation of defects occurs.

The Kinchin-Pease model derivation ends with the resulting equations

$$v(T) = 0 \quad \text{for} \quad T < E_d \quad (1.8)$$

$$v(T) = 1 \quad \text{for} \quad E_d < T < 2.5 E_d \quad (1.9)$$

$$v(T) = \frac{T}{2E_d} \quad \text{for} \quad 2.5 E_d < T < E_c \quad (1.10)$$

$$v(T) = \frac{E_c}{2E_d} \quad \text{for} \quad T \geq E_c \quad (1.11)$$

Modern computer software programs, such as the Stopping Range of Ions in Matter (SRIM) software, use the Norgett-Robinson-Torrens (NRT) modification of the Kinchin-Pease model for defect production. This modification used binary collision computer simulations of ion collisions in solid to demonstrate that about 20% of the sites from where an atom is kicked out are then refilled by another atom.⁴⁰ This resulted in a prefactor of 0.8 being introduced to the Kinchin-Pease equation.

SRIM software currently remains the most common software for the analysis of ion beam radiation interactions with either monoatomic or multiatomic targets.⁴² The SRIM software can quickly output computational data of the interaction between the selected ions and target and generate results on the probable damage cascade, defects produced, and depth of damage.^{42,43}

General calculations by the 2013 SRIM code output detailing the irradiation-induced vacancy distribution in different materials is shown in *Figure 1.12*.

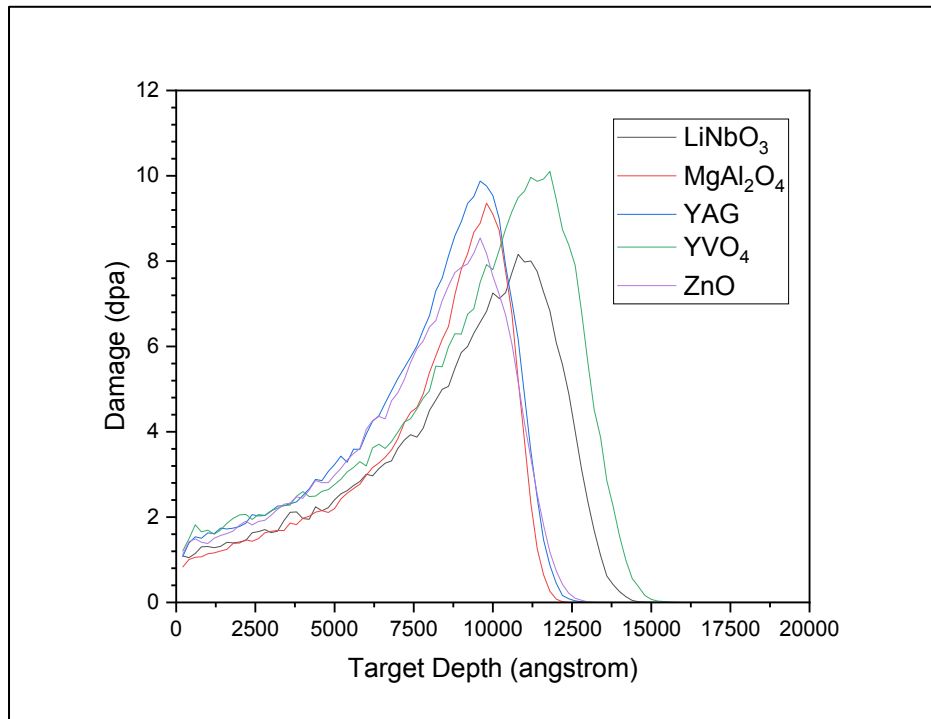


Figure 1.12: 2013 SRIM calculations of 10,000 1 MeV O⁺ irradiation-induced damage distributions as a function of penetration depth for multiple materials.

1.3 – Ion Irradiation Damage Effects

As mentioned before, ion irradiation damage can create permanent changes to a material's structural, physical, and chemical properties.⁴ For the scope of this project, the effects of ion irradiation damage on crystalline ceramic materials will be discussed. Special emphasis will be placed on changes in the structural and optical property changes, due to the characterization methods discussed in the following chapter.

1.3.1 – Displacement Damage

When hit by high energy ions, ceramic materials undergo displacement damage (DD) through the creation of vacancies, interstitials (Frenkel defects), and dislocation loops.⁴ These can result in changes of material properties such as the surface potential, surface conductivity, and mobility.^{35,44} Displacement damage for ceramic materials occurs in functional ceramics due to nuclear collisions.⁴⁴ However, as illustrated in *Figure 1.10*³⁹ showing the results of molecular dynamics, considerable recovery of displacement damage in ceramics occur due to the mobility of point defects and atoms.⁴⁵ *Figure 1.13*³⁵ further illustrates several primary radiation damage events that occur.

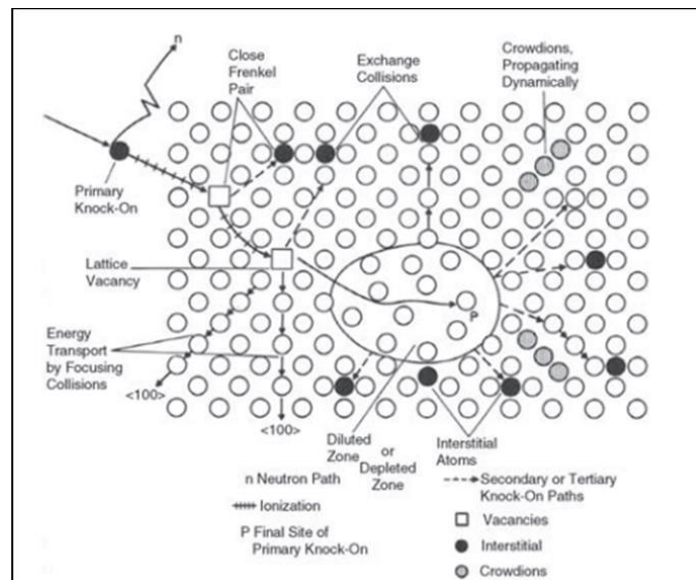


Figure 1.13: Primary radiation damage events in materials.³⁵

1.3.2 – Sputtering Effects

Sputtering refers to the ejection of target atoms from the surface due to collision cascades created by the irradiation ion. It is common for a number of characterization techniques to use controlled sputtering for chemical analysis of the sputtered atoms or the new surface layers

underneath, *e.g.*, mass spectrometry and X-ray photoelectron spectroscopy (XPS).⁴⁶ However, sputtering can also remove some of the damage created by ion irradiation and modify the irradiation and defect depth distributions. The amount of sputtering due to irradiation varies by material, irradiation ion, and ion energy. The surface binding energy E_s gives the required energy needed to remove a target atom from the material's surface. Since this value is only known for a few materials, 2013 SRIM calculations use the heat of sublimation as a close estimate.³⁷

1.3.3 – Amorphization

Amorphization refers to the global response of a material under irradiation in which the translational symmetry of the crystalline structure and the identity of individual defects are lost, and the entire solid shifts to a uniformly defective state.⁴⁶ Amorphization can occur at low temperatures and low displacement values (~ 1 dpa), resulting in both swelling and compaction.⁴⁶ The amorphization dose [eV/atom] transferred to the material depends on both the incident ion, ion energy, and the temperature. A critical amorphization temperature (T_c) can be reached where amorphization can no longer occur due to enhanced thermal annealing and the consequent structural healing as shown in *Figure 1.14*.⁴⁷

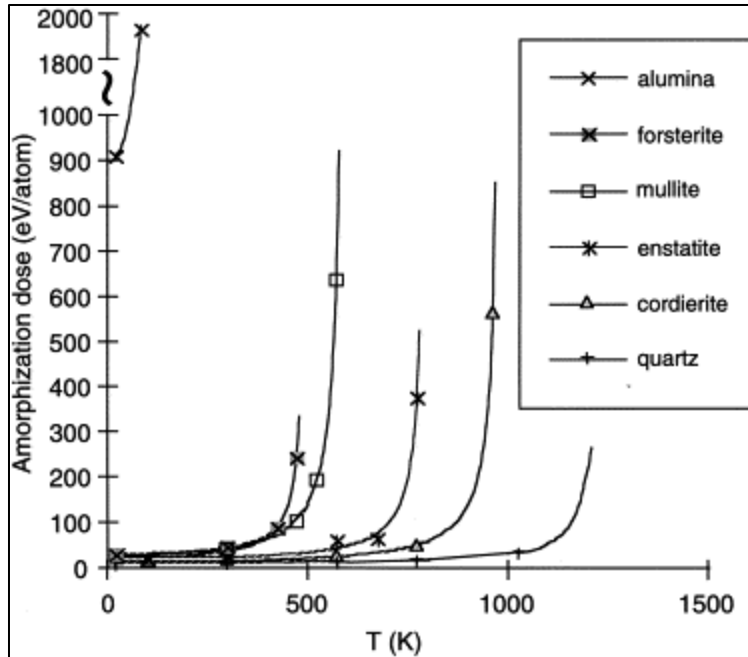


Figure 1.14: Temperature dependence of amorphization dose of 1.5 MeV Xe^+ irradiation for indicated phases.⁴⁷

1.4 – Motivation

In April 2010, the Galaxy 15 satellite used for telecommunications suddenly lost contact with ground control and began to drift from its orbit path. This drift lasted for eight months and placed the satellite in danger of impacting other satellites or potentially interfering with their transmissions. Researchers suggested that this loss of contact was due to spacecraft charging due to the ionizing dose of electrons in the radiation belts. When the buildup exceeded a certain limit, an electrostatic discharge occurred that knocked out Galaxy 1's communications systems. While the satellite was able to be recovered, other satellites such as the Advanced Earth Observing Satellite 2 (ADEOS -II) in 2003 were not as fortunate.⁴⁸

The loss of a satellite due to radiation damage from charged electrons and ions results in a massive loss of resources for the mission and places other satellites in harm's way. This project's

aim is to better understand the effects of near-Earth ion irradiation damage on selected functional ceramic materials. The goals of the research are to gain insight into

- 1) How optical functionalities are affected by ion irradiation
- 2) How effective optically active defects are as probes for radiation damage

Since radiation damage is a complex phenomenon that is affected by the energy and chemical nature of the projectile as well as the characteristics of the target, a suite of characterization techniques covering different and complementary aspects will be used in this work. These techniques are discussed in Chapter 2.

CHAPTER TWO
EXPERIMENTAL PROCEDURES

2.1 – Materials

Five different single-crystal ceramic materials were chosen to undergo ion-irradiation in order to understand their structural and optical responses to ion irradiation. These materials are lithium niobate (LiNbO_3), a piezoelectric material used as an optical waveguide; magnesium aluminate spinel (MgAl_2O_4), used as a broad-range optical window; yttrium aluminum garnet ($\text{Y}_3\text{Al}_5\text{O}_{12}$), used as a scintillator and a phosphor in LEDs when doped with Ce; yttrium vanadate (YVO_4), used as a polarizing prism and a display phosphor medium; and zinc oxide (ZnO), a wide band gap semiconductor used as a piezoelectric transducer, varistor, and phosphor. Each of these materials was selected due to their capabilities as functional ceramic materials and for having extensive literature about them than can be used in the interpretation of the irradiation effects.

Table 2.1 summarizes relevant properties of these materials.

Table 2.1: Summary of physical properties of the ceramic materials investigated in this work.¹⁻¹⁰

Property	LiNbO_3	MgAl_2O_4	YVO_4	$\text{Y}_3\text{Al}_5\text{O}_{12}$	ZnO
Crystal Structure	hexagonal	cubic	tetragonal	cubic	hexagonal
Growth Method	Czochralski	Czochralski	Czochralski	Czochralski	hydro-thermal
Mass Density (g/cm^3)	4.30	3.60	4.22	4.57	5.675
Atomic Density ($\times 10^{22}$ atm./ cm^3)	8.76	1.07	7.48	9.27	9.90

Melting point (°C)	1,250	2,130	1,825	1,970	1,975
Band gap (eV)	3.7	7.8	3.7	6.5	3.3
Displacement Energy (eV)	40	$E_d^O = 60$ $E_d^{Mg} = 30$ $E_d^{Al} = 30$	40	40	$E_d^O = 55$ $E_d^{Zn} = 50$
Lattice Energy (eV)	3	3	3	3	3
Surface Energy (eV)	$E_s^{Li} = 1.67$ $E_s^{Nb} = 7.59$ $E_s^O = 2$	$E_s^{Mg} = 1.54$ $E_s^{Al} = 3.36$ $E_s^O = 2$	$E_s^Y = 4.24$ $E_s^V = 5.33$ $E_s^O = 2$	$E_s^Y = 4.25$ $E_s^{Al} = 3.36$ $E_s^O = 2$	$E_s^{Zn} = 1.35$ $E_s^O = 2$

The samples were all purchased from MTI Corporation as 1 cm x 1 cm x 0.5mm 2-side polished plates. Each ceramic crystal was then manually cut into four *ca.* 5mm x 5mm x 0.5mm pieces (*cf.* Figure 2.1). This allowed the use of three out of the four crystal pieces to undergo ion irradiation, with the fourth piece being kept as a reference sample to determine material changes from radiation damage. All of the functional ceramic samples, except for zinc oxide, were grown using the Czochralski method as shown in Table 2.1. The Czochralski process is a controlled manufacturing method for producing bulk single crystals for optical and electronic materials.¹¹ It involves melting the feed material, usually through resistance heat, into a cylindrically shaped crucible. A seed crystal (typically a few mm) is then slightly dipped into the melt surface and slowly withdrawn from the feed material. The shape of the crystal can be controlled by adjusting either the heating power, the pulling rate, or the rotation rate of the mechanism.¹¹

Zinc oxide was synthesized using the hydro-thermal crystal growth method, which is mainly used to create large and dislocation-free single crystals.¹² In general, this method grows the

crystals within an autoclave (typically high-strength steel) that contains a liner to isolate the growth environment from the autoclave walls. The liner is divided into two chambers, with one containing solid nutrients and the other ZnO seed crystals. A temperature of 200-1000 °C is maintained in the nutrient chamber with a temperature gradient of 10-15 °C, allowing a convection current for seed crystals to be transported inwards. After 30 days at a pressure between 10-100 MPa, the growth process is typically complete.¹²


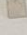













Material	H ⁺	He ⁺	O ⁺
MgAl ₂ O ₄			
YVO ₄			
LiNbO ₃			
Y ₃ Al ₅ O ₁₂			
ZnO			

Figure 2.1: Complete ensemble of samples investigated in this work.

Ion irradiation of the five materials was conducted at the Accelerator Laboratory of Texas A&M University (AL-TAMU; *Figure 2.2*¹³).

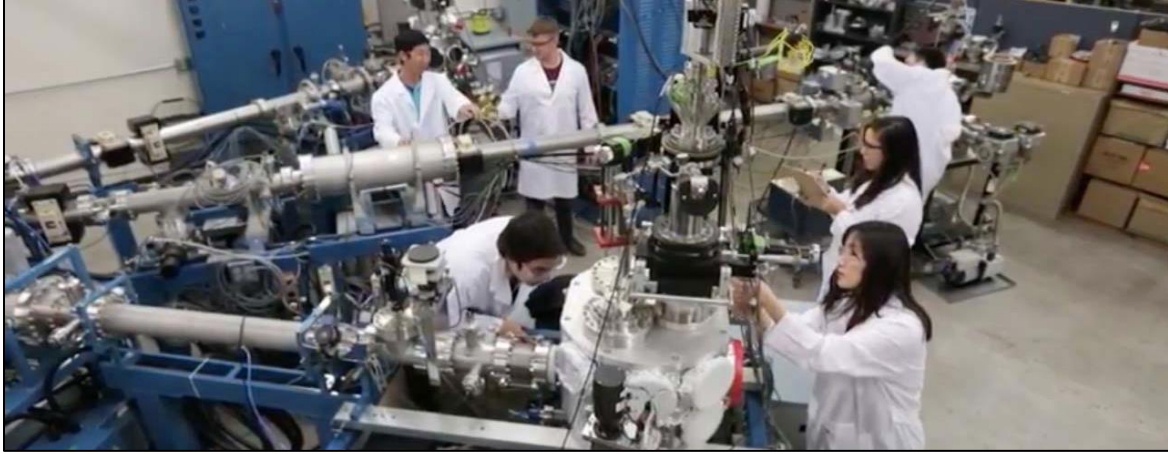


Figure 2.2: General view of the Accelerator Laboratory at TAMU.¹³

Three different ions (H_2^+ , He^+ , and O^+) were selected to irradiate the samples due to their abundance in the near-Earth space environment, as discussed in the previous chapter. In terms of irradiation conditions, it is noted that the 400 kV accelerator at AL-TAMU was not operational. In order to obtain irradiated samples within the period of execution of the Grant supporting this investigation, the original conditions (50 kV H^+ , 200 kV He^+ and 800 kV O^+) where all ions had the same 50 keV/nucleon were adjusted as needed according to equipment availability. The actual irradiation conditions of each ion can be found in *Table 2.2*. One set of samples was irradiated with 1 MeV O^+ ions using a 3 MV Tandem accelerator. The beam was rastered to cover an area of $1.1 \text{ cm} \times 1.7 \text{ cm}$, with an average flux of $3.3 \times 10^{12} \text{ ions/cm}^2\text{s}$. The vacuum level was 10^{-8} Torr. The other sets of samples were irradiated with 120 keV He^+ ions and 120 keV H_2^+ ions using a 140 kV accelerator. The beam was rastered over an area of $1.7 \text{ cm} \times 1.2 \text{ cm}$ for both irradiations. The average flux of the He^+ beam was $9.9 \times 10^{12} \text{ ions/cm}^2\text{s}$, and the average flux of the H^+ beam was $5.3 \times 10^{12} \text{ ions/cm}^2\text{s}$. The vacuum level was at low 10^{-7} Torr. It is noted that 120 keV H_2^+ ions will break into two 60 keV H^+ ions upon interacting with the crystals and, henceforth, hydrogen irradiation will be discussed in terms of 60 keV H^+ ions. The energy per nucleon values used in

this work are close to the lowest range of CMEs (~ 100 keV/n) and within the energy range found in the radiation belts. Ion beam rastering was used to irradiate the large enough area that contained all five crystals. *Figure 2.3* shows instantaneous images of the crystals while under ion irradiation and *Figure 2.4* illustrates ion beam rastering for the case of H_2^+ irradiation. In both cases, the consequent emission of ionluminescence is evident. *Figure 2.1* shows a photograph of all samples of all the five compounds under investigation in this work, including the non-irradiated ones used as references. According to the AL-TAMU staff who performed the irradiations, the temperature of the stage (sample holder) during O^+ irradiation reached 80 °C, so it was estimated that the crystals were at about 100 °C. For H_2^+ and He^+ irradiations, since the beam energy was lower, the temperature was estimated to be around 75 °C. No significant structural healing is expected at these temperatures. After irradiation, the samples were investigated at Clemson University using a suite of characterization techniques discussed below.

Table 2.2: Sample irradiation conditions.

Ion	Energy [keV]	Energy/nucleon [keV/n]	Fluence [ions/cm²]	Beam Current [μA]	Beam Flux [ions/cm²/s]
H_2^+	120	60	5×10^{16}	0.8	5.3×10^{12}
He^+	120	30	5×10^{16}	3.0	9.9×10^{12}
O^+	1000	62.5	5×10^{16}	1.0	3.3×10^{12}

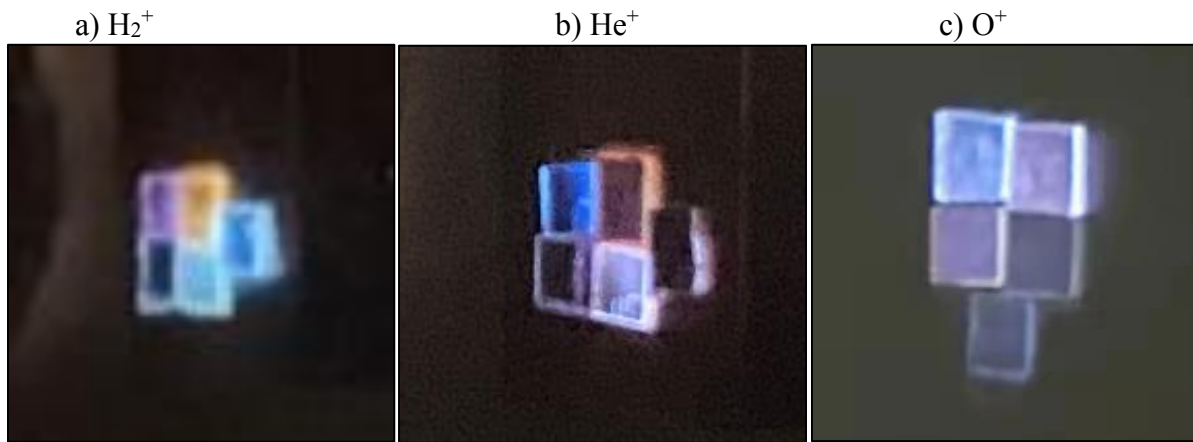


Figure 2.3: Iono-luminescence of the crystals under ion irradiation: a) H_2^+ , b) He^+ , and c) O^+

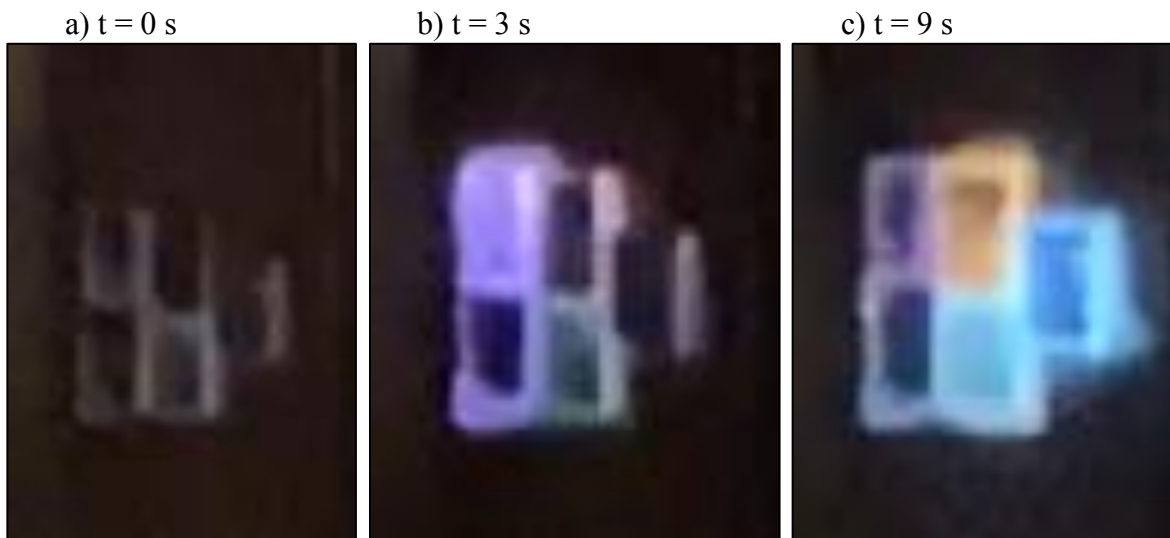


Figure 2.4: Rastering of H_2^+ beam onto crystals and consequent iono-luminescence at a) $t = 0$ s, b) $t = 3$ s, and c) $t = 9$ s .

2.2 – Computational and Experimental Characterization Methods

The effect of radiation damage on ceramic materials is best investigated using a combined approach consisting of structural and optical changes complemented by Monte Carlo calculations of the interaction of ion beams with solids. A brief overview of each characterization technique used, as well as their respective experimental parameters and analysis software will be discussed.

2.2.1 – Computational Calculations

Computational calculations were executed with the 2013 SRIM¹⁴ computer code. They were used for characterizing radiation damage due to ion-beam irradiation. The code is based on the Monte Carlo method that performs computational analysis by building models of possible outcomes by substituting a probability distribution for factors of inherent uncertainty. Then, it calculates a possible outcome multiple times by using a different set of random numbers as input in the probability functions.¹⁵ In the 2013 SRIM code, users can customize different target layers with specified chemical compositions and densities while controlling the nature of the ion, ion-beam energy, and incident angle.¹⁴ Distinctive values for elemental displacement, lattice, and surface energies can be selected with 2013 SRIM offering default values for each element, if needed. Output text files include information on the ion ranges in the material, backscattered ions, transmitted ions, sputtered atoms, and collision details with depth distribution of elemental vacancies created. For the calculations of each material, irradiation damage from a total of 10,000 ions was calculated for each ion. The general 2013 SRIM window for setting the irradiation conditions is illustrated in *Figure 2.5*¹⁴ for the 60 keV H⁺ irradiation of MgAl₂O₄.

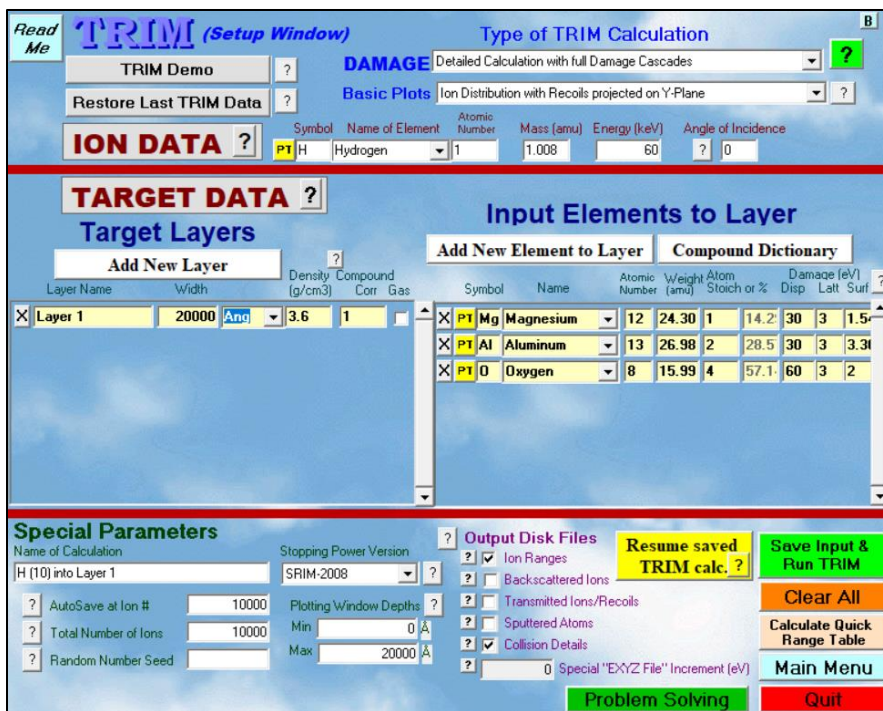


Figure 2.5: Example of 2013 SRIM setup window for 60 keV H^+ irradiation of $MgAl_2O_4$.¹⁴

There are several assumptions contained within the 2013 SRIM code. It assumes the incident ion beam as a flow of individual particles, without considering the dimensions of the ion beam or the spatial distribution of ions in the beam or any type of effects of an earlier ion with the new ion under calculation.⁶ Also, it assumes an amorphous structure, *i.e.*, no crystallographic effects are taken into account and assumes that ion irradiation occurs at 0 K. Therefore, no thermal effects from the incident beam energy are accounted for, *i.e.*, there is no diffusion and no self-healing of the structure. Also, 2013 SRIM assumes a constant displacement, lattice, and surface energy value during the process of irradiation.¹⁵

In order to calculate the effect of ion irradiation on the ceramic crystals, the detailed calculation with full damage cascades option was selected. The use of the full damage cascade option allows for advanced outputs of irradiation damage including specific vacancy production by target material elements and detailed sputtering calculations. These advanced outputs provide

a detailed picture of the calculated irradiation damage. The specific values used in 2013 SRIM for material density and displacement energies can be found in *Table 2.1*. For the lattice energy and surface energy, the values shown in *Table 2.1* were automatically generated by 2013 SRIM.

2.2.2 – Raman Spectroscopy

Raman spectroscopy is a technique based on the Raman scattering phenomenon, discovered in 1928, that corresponds to the light scattered by a material gaining or losing some of its energy.^{16,17} It is useful to examine the structure of a material by analyzing the different vibrational modes of molecular bonds (*i.e.*, stretching, bending, *etc.*).¹⁶ This is possible by using a monochromatic electromagnetic radiation source ($h\nu_o$), commonly a laser, to strike the sample, causing some of the radiation to scatter in all directions.¹⁷ The inelastic portion of the scattered irradiation ($h\nu$, typically 10^{-7} of the scattered light) will have a different frequency than the incident radiation. When it has a lower frequency than the source ($h\nu_o - h\nu$), it is referred to as a Stokes shift, and the opposite ($h\nu_o + h\nu$) is referred to as an anti-Stokes shift.¹⁶ In this work, the more probable Stokes shift was measured. A theoretical Raman peak should correspond to single line peak, with the spectrum corresponding to several lines that represent the different vibrational modes. In practice, broadening of peaks is observed with the line shape being determined by the materials intrinsic properties, including structural disorder, defects, amorphization, and inhomogeneities in the material.¹⁷

In order to be Raman active, the vibration mode must create *polarizability* (α) changes in the molecule. The polarizability results from the creation of an induced dipole moment (μ) from an electric field and is defined by¹⁷

$$\mu = \alpha E \tag{2.1}$$

where E is the strength of the electric field. Raman activity therefore requires that the first derivative of polarizability with respect to vibration is not zero when at its equilibrium position. Once the vibration mode is shown to be Raman active, the structural unit of the sample can be determined since each unit has unique vibrational energy states. The resulting Raman shift is typically displayed as a measure of intensity per cm^{-1} as shown in *Figure 2.6*. Raman spectroscopy can probe different depths, depending on the wavelength of the laser and the magnification of the objective used. Since the ion beam cannot penetrate through the entire depth, the irradiated samples were carefully examined to determine if the side being characterized was the same side previously irradiated.

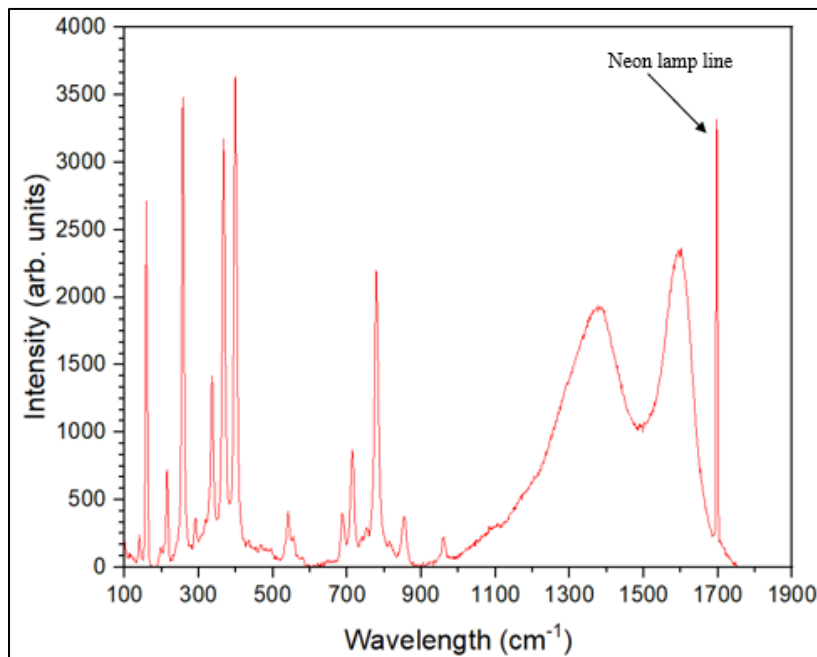


Figure 2.6: Raman spectra of H⁺ irradiated Y₃Al₅O₁₂ with neon lamp line reference.

Raman spectroscopy measurements were conducted using a LabRAM HR Evolution Raman Spectrometer confocal microscope equipped with an 800 mm focal length spectrograph and an air-cooled (-60 °C) back-illuminated deep-depleted 1024 x 256 pixels CCD detector. The

monochromatic source consisted of a 100 mW frequency doubled Nd:YAG laser emitting at 532 nm. The neutral filter density [%] used on the laser beam was material dependent to allow for high signal-to-noise ratios without allowing for laser-induced modifications of the material. Spectra were collected from 100 cm⁻¹ to 1750 cm⁻¹ and corrected by the pre-recorded instrument-specific response to a calibrated white light source (ICS) within the LabSpec6 software program.¹⁸ This software program was also used to conduct background corrections of the spectra and peak normalization. Background subtraction was done using the automated linear subtraction method within the software, with 20 points automatically selected across the spectral region of interest. After subtraction, all spectra were normalized to the intensity of a selected peak, which will be discussed in later chapters. All measurement conditions used can be found in *Table 2.3*.

Table 2.3: Parameters for obtaining Raman spectra of all samples.

Parameter	Value
Acquisition time [s]	20
Number of runs	10
Grating [nm]	600
Optical [magnification]	100x
Background correct type	Linear subtraction
Background correction points	20
Lasers Density (%)	MgAl ₂ O ₄ : 100 YVO ₄ : 3.2 Y ₃ Al ₅ O ₁₂ : 100 LiNbO ₃ : 5 ZnO: 50

Raman peak positions in ceramics have been shown to shift due to internal stresses after ion irradiation when compared to their stress-free references.^{19,20} A neon lamp source was

introduced into the experimental setup in order to allow for precise calculations of peak position shifts due to irradiation. The neon lamp has many sharp lines with well-known position. In this work, all spectra were corrected in relation to the neon line at 1696.8 cm^{-1} .²¹ An example of this peak is observed in *Figure 2.6*, and the experimental setup of the neon lamp is shown in *Figure 2.7*. It included a visible light beam splitter and an iris controlling the influx of neon light that was kept at a minimum to reduce signal intensity. Raman analysis was focused on determining shifts in peak locations after correction by the neon reference and changes in peak full width at half maximum (FWHM). This analysis was done using the OriginPro Graphing and Analysis software. The peak position corresponded to the intercept of the vertical axis that divided the band equally in two parts with the abscissa. The position of the axis was determined by visual inspection based on the shape and symmetry of the band.



Figure 2.7: a) Raman spectrometer setup with b) neon lamp reference.

2.2.3 – UV-Visible Optical Spectroscopy

This technique can be used to determine and quantify spectral regions of a material where light absorption and transmission occurs. In this technique, the intensity of light passing through

the sample and through the reference stage is recorded as I and I_0 , respectively, as a function of the wavelength of light.



Figure 2.8: UV-Vis Spectrometer (left) and stage (right) with a) reference and b) pair of identical customer-designed sample holders. The sample, a crystal, can be observed on the (b) sample holder.

The I/I_0 intensity ratio, that corresponds to the optical transmittance of a material, can be analyzed, and directly related to material properties. This is accomplished using the Beer-Lambert's law, which states that:²²

$$I/I_0 = e^{-\mu(x)} \quad (2.2)$$

where μ is the coefficient of extinction, and x is the sample thickness. Since scattering is assumed to be negligible from the polished faces of the crystals used in this work, the extinction coefficient can be approximated by the absorption coefficient. The absorption intensity can be determined from the formula:²³

$$A = -\log_{10} T \quad (2.3)$$

where T is the transmittance. An example of this measurement can be found in *Figure 2.9*.

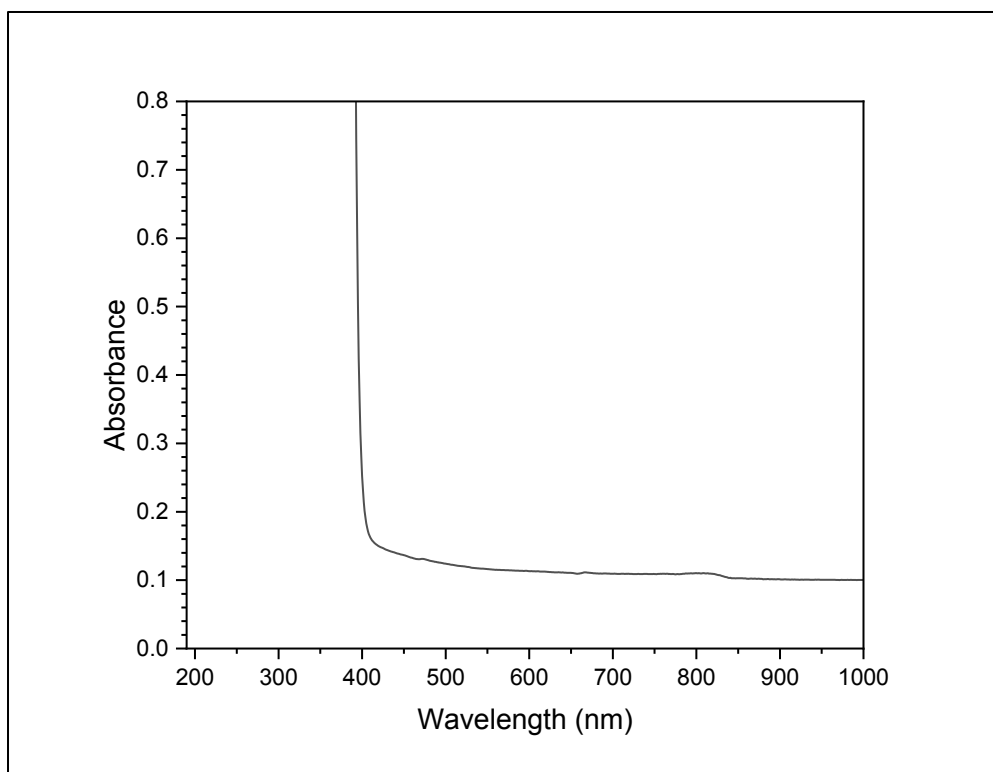


Figure 2.9: Optical absorption spectrum of pristine ZnO crystal.

Optical transmittance spectra were collected using the Shimadzu UV-3600 UV/Vis/NIR spectrometer (*Figure 2.8*) from 190-1000 nm with a step size of 1 nm. A background run was conducted before the experiments. A customer-designed sample holder was fabricated to guarantee that all light went through the sample (*Figure 2.8*). The reference holder hole was left empty; therefore, each sample was measured against a reference of ambient atmospheric conditions. Transmittance spectra were automatically collected and organized with the UV Probe 2.42 software before being exported as text files. Additional equipment parameters can be found in *Table 2.4* below. Optical absorbance results will focus on the analysis of changes of the intensity of the absorption bands and the possible creation of new bands due to irradiation as well as a function of dpa. In each spectrum, there is a general small shift in optical absorption magnitude at ~830 nm attributed to the detector change in this equipment.

Table 2.4: Additional parameters for UV-visible spectroscopy.

Parameter	Setting
Scan speed	medium
Scan mode	single
Measuring mode	transmittance
Slit width	5 nm
Time constant (s)	0.1
Light source wavelength change	282 nm
Detector wavelength change	830 nm

2.2.4 – Radioluminescence

Radioluminescence (RL) arises due to interactions between ionizing radiation, such as α or β particles or X-rays, and matter.^{24,25} The mechanism of RL excitation is initiated by the absorption of the X-ray photon by an electron thus creating an energetic photoelectron (*i.e.*, photoionization). As the photoelectron travels through the material, it transfers its energy to atomic electrons creating additional ionizations. The electron-hole pairs move through the material and eventually recombine at the luminescence center when light is emitted.^{22,24} This bombardment of ionizing radiation results in luminescence of the target material from its luminescence centers that can be dopants, defects, or molecular groups. A photodetector is then used to quantify the intensity of the luminescence as a function of the wavelength. It is noted that many unirradiated materials already contain luminescent defects, and thus the analysis of the luminescence relative intensity can reveal the creation or quenching of the luminescence centers due to radiation damage. A typical RL spectrum can be found in *Figure 2.10*.

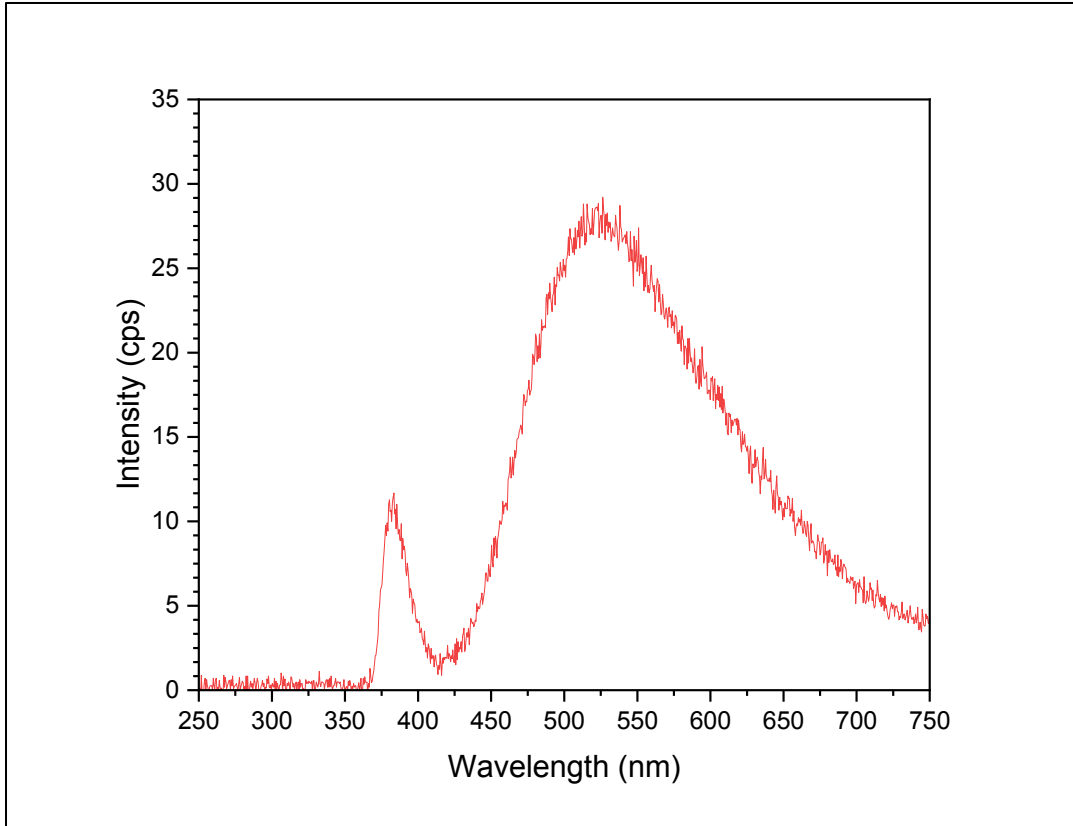


Figure 2.10: RL spectra of H⁺ irradiated ZnO.

Radioluminescence (RL) measurements were executed using a customer-designed configuration of the Freiberg Instruments Lexsyg spectrofluorometer equipped with a Varian Medical Systems VF-50J X-ray tube (40 kV, 1 mA) with a tungsten target. The X-ray source was coupled with a Crystal Photonics CXD-S10 photodiode for continuous radiation intensity monitoring. The light emitted by the sample was collected by an Andor Technology SR-OPT-8024 optical fiber connected to an Andor Technology Shamrock 163 spectrograph coupled to a cooled (-80 °C) Andor Technology DU920P-BU Newton CCD camera (spectral resolution of ~0.5 nm/pixel). An image of this setup can be found in *Figure 2.11*.

RL testing was done under continuous X-ray irradiation at room temperature. Different integration times were selected for each material to achieve good signal-noise ratios of the RL

intensity for reliable analysis. These integration times can be found in *Table 2.5*. During data acquisition, the random presence of cosmic rays passing through the CCD detector caused the appearance of sharp peaks (corresponding to a few data points) in the RL spectra. These peaks could not be avoided but were manually removed from the spectra using the OriginPro 2021 Graphing and Analysis software. Spectra were corrected by the built-in wavelength response of the system and an intensity background of 300 [arb. units] was subtracted for each spectrum before normalization. Each spectrum also had their intensities divided by the integration time resulting in counts per second (cps). It is noted, however, that RL intensities among samples cannot be compared because the samples had different shapes and thus different surface areas (*cf. Figure 2.1*), but the orientation of the samples in relation to the X-ray beam and to the optical fiber was not reproducible. Consequently, RL analysis will be limited to the observation of relative intensities within a same spectrum.

Table 2.5: RL spectra integration time by crystal.

Sample	LiNbO₃	MgAl₂O₄	YVO₄	Y₃Al₅O₁₂	ZnO
Integration time [s]	200	5	1	1	10



Figure 2.11: Photograph of the Freiburg Instruments Lexsyg spectrofluorometer showing the spectrograph (bottom) coupled to the CCD detector (top), the optical fiber, and the X-ray source in the back. The small cylinder at the center corresponds to the photomultiplier tube. The sample wheel is shown on the right.

2.2.5 – Thermoluminescence

Thermoluminescence (TL) refers to the light emitted by the moderate heating of a solid that has been previously exposed to ionizing radiation. It is not incandescence (blackbody radiation) and is related to electronic transitions between defects (traps) and luminescence (recombination) centers. TL measurements are limited to temperatures where the blackbody emission of the material is negligible, typically up to 400 °C.²⁵ Exposure to ionizing radiation (X-rays, high energy particles) at room temperature facilitates the capture of electrons by traps. When the sample is then heated, the trapped charge carriers are released and can undergo radiative recombination (at the luminescence center) that is known as thermoluminescence.²⁶ This emission of light can then be expressed as a function of temperature. These results are known as glow curves and their analysis can provide information on the energy depth of the traps. It is also possible to extract emission spectra while heating up the sample and these results are useful to identify the

recombination centers of the material involved in the TL process.^{25,26} An example of a glow curve obtained in this work can be found in *Figure 2.12*.

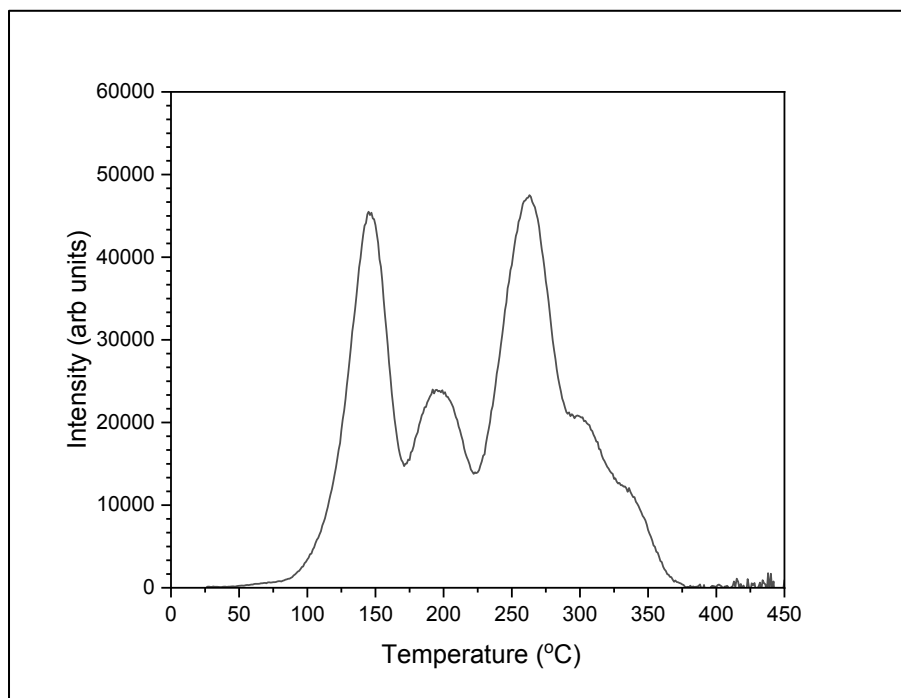


Figure 2.12: Glow curve of the pristine Y₃Al₅O₁₂ crystal.

TL measurements as a function of temperature were carried out using the same Lexsyg spectrofluorometer by Freiburg Instruments as described in Section 2.2.5 and shown in *Figure 2.11*. All emitted light intensities from the pristine and irradiated samples were collected using the Hamamatsu H7360-02 series photomultiplier tube. No filter was placed before the photomultiplier tube.

The procedure for these TL measurements involved an initial heating of each sample from 0 °C to 450 °C at a rate of 5 °C/s and holding it at 450 °C for 30 s in order to clear any traps. The samples were then cooled down to room temperature and X-ray irradiated at different times depending on the material in order to achieve high signal-to-noise ratios. After irradiating with the

X-ray source, as described in section 2.2.5, the intensity of the emitted light was collected from 25-400/450 °C at a heating rate of 1 °C/s. Then, the sample was measured again with the same experimental parameters but without any previous X-ray irradiation in order to check if traps were fully depopulated and to obtain the blackbody background for each sample. Specific irradiation times for each material can be found in *Table 2.6*. TL analysis will be limited to the observation of the relative behavior of the glow peaks within a same spectrum, with particular attention to check if glow peaks were created or eliminated.

It is possible that a material has traps at deeper energies than can be probed by thermal excitation. Consequently, these traps can ‘seep’ electrons to traps at lower energies making the TL glow curves change in time. In order to check for this effect, after these TL measurements were finished, TL ‘reproducibility’ measurements were conducted by performing the basic TL procedure described above two times in a row from 25-400 °C at a heating rate of 1 °C/s . This allowed for the analysis of changes in the relative intensity of the glow peaks. TL reproducibility analysis will be limited to determining the effect deeper traps have on luminescent intensities, if any.

Table 2.6: X-ray irradiation time for TL measurements per material.

Sample	LiNbO₃	MgAl₂O₄	YVO₄	Y₃Al₅O₁₂	ZnO
Irradiation time [s]	2500	20	2500	20	2500

Additional TL measurements were recorded as a function of both temperature and emitted wavelength, *Figure 2.13*, in order to determine the identity of the recombination centers in the material involved in the TL process. They are referred to as TL spectroscopy. Since no new glow peaks were observed in the ion irradiated samples, these measurements were executed on the

pristine samples only. Each sample was previously X-ray irradiated for the same times found in *Table 2.6*, and heated at either 0.5 or 1 °C/s up to 400 °C. However, changes were made to the integration time and channel time for each material. The channel time corresponds to the time between two consecutive measurements. The integration time was decided based on the TL glow curve such that the main TL glow peak would be fully integrated. This can be visualized by checking the TL glow curve of the material against the maximum readout temperature reached after the integration time. For example, for $Y_3Al_5O_{12}$ (*Figure 2.12*), TL emission was integrated within 25-95, 95-165 and 165-235 °C that correspond to the first, second and third glow peaks, in addition to 235-305 and 305-400 °C that correspond to the two high-temperature shoulders and the remaining of the glow curve, respectively. Also, a 500 s-long pause was included between the X-ray irradiation and the readout to eliminate any possible effect of afterglow. These specific parameters can be found in *Table 2.7*. Emitted light was detected as previously described in Section 2.2.5. TL spectroscopy analysis will be limited to determining the identity and contribution of luminescence centers in the TL process.

Table 2.7: Experimental parameters for TL spectroscopy measurements.

Material	LiNbO₃	MgAl₂O₄	YVO₄	Y₃Al₅O₁₂	ZnO
X-ray irradiation [s]	2500	100	2500	100	2500
Heat rate [°C/s]	1	0.5	1	1	1
Integration time [s]	245	20	125	70	375
Channel time [s]	0.1	30	0.1	0.1	1

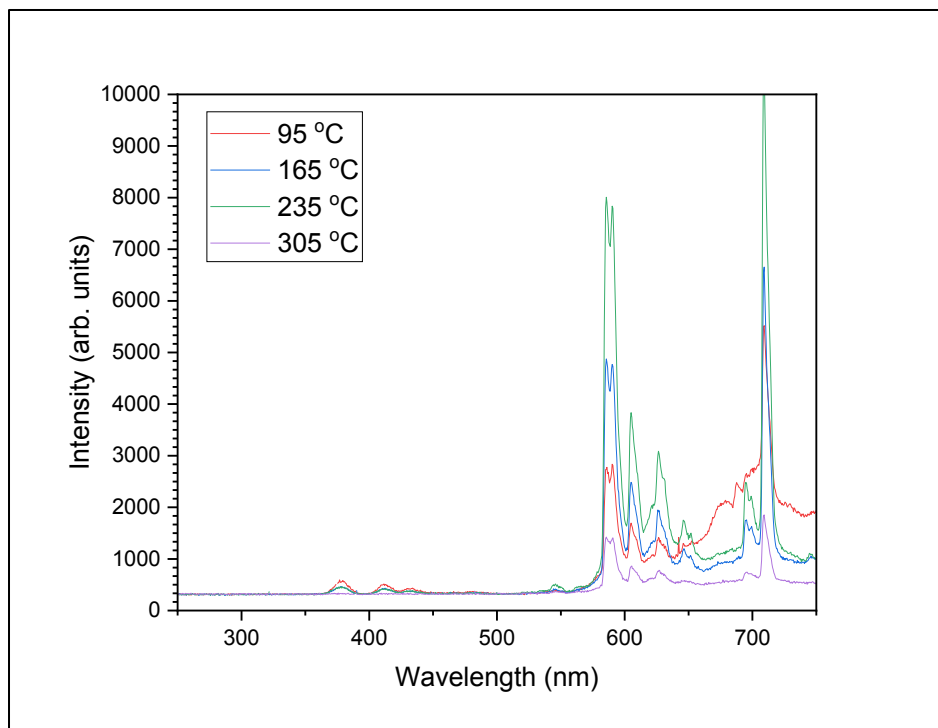


Figure 2.13: TL spectra of pristine $Y_3Al_5O_{12}$ crystal. Each spectrum was obtained over a temperature range that starts at the temperature indicated in the legend.

CHAPTER THREE

2013 SRIM MONTE CARLO RESULTS AND DISCUSSION

The goal of this chapter is to examine the results of Monte Carlo calculations using the 2013 SRIM software.¹ Additional 2013 SRIM calculations and outputs will be analyzed in the following chapters, however those are divided according to the materials investigated in this work due to the nature of their information.

3.1 – Projected Range of Ions

Knowing the projected range of the ions within the ceramic crystals is necessary in order to understand the location of the damage created. Any new defects created by the irradiation process will be located within this range.

In order to determine the depth of the layer affected by the ion irradiations wherein defects are created, the predicted range needs to be determined. Therefore, 2013 SRIM calculations were conducted using the software option “Stopping/Range Tables” that are based on the transport equation approach PRAL² (Projected RAnge ALgorithm) with the proper input parameters as shown in *Table 2.1*. These estimated values for the projected range along with the longitudinal straggling can be found in *Table 3.1* below.

Table 3.1: Projected range of ions [μm] from 2013 SRIM calculations. The longitudinal straggling is given in the form of \pm deviation.

Material	Density (g/cm^3)	60 keV H^+	120 keV He^+	1 MeV O^+
MgAl_2O_4	3.60	0.39 ± 0.06	0.49 ± 0.08	1.01 ± 0.11
YVO_4	4.22	0.46 ± 0.10	0.56 ± 0.14	1.17 ± 0.21
LiNbO_3	4.30	0.41 ± 0.09	0.52 ± 0.13	1.12 ± 0.20
$\text{Y}_3\text{Al}_5\text{O}_{12}$	4.57	0.38 ± 0.08	0.48 ± 0.10	0.99 ± 0.16
ZnO	5.675	0.41 ± 0.10	0.50 ± 0.14	1.03 ± 0.21

As show in *Table 3.1*, there is an observable increase of ion penetration depth for increasing ion energy. This is in general agreement with the theoretical expression³ for the projected range of an ion that considers the nuclear and electronic energy losses as discussed in Chapter 1. As observed from *expression 1.1* for the projected range of the ions, the distance is determined by integrating the inverse stopping power over the entire energy of the incident ion. Therefore, in general, an ion with a higher initial energy will result in a higher expected value for the projected range. On the other hand, this trend is not linear, and deviations are found since the nuclear and electronic stopping power expressions depend on the incident ion energy as well as the mass and charge of the incident ion, in addition to material characteristics. In all, the projected range was determined to be within $\sim 0.4\text{-}1.2 \mu\text{m}$.

3.2 – Sputtering Effects

In order to determine if sputtering played a major role on the depth distribution of the defects, the number of monolayers removed was estimated. 2013 SRIM outputs the sputtering coefficient Y_s (atoms/ion), which can then be used to estimate the number of monolayers removed

from the sample. Accordingly, the average areal atomic density per monolayer (N_s) needs to be calculated:⁴

$$N_s \cong N^{2/3} \quad (3.1)$$

where N is the material's atomic density. After determining the average areal atomic density per monolayer, the number of monolayers removed (N_m) can then be determined using:

$$N_m = \frac{Y_S \Phi}{N_s} \quad (3.2)$$

where Φ is the ion fluence given in number of impinging ions/cm². The calculated number of monolayers removed per ion by material can be found in *Table 3.2*.

Table 3.2: Number of monolayers removed due to sputtering.

Material	Atomic Density (atoms/cm³)	60 keV H⁺	120 keV He⁺	1 MeV O⁺
MgAl ₂ O ₄	1.07 x 10 ²³	0.0	0.0	2.3
YVO ₄	7.48 x 10 ²²	0.3	0.4	3.6
LiNbO ₃	8.76 x 10 ²²	0.0	0.4	3.8
Y ₃ Al ₅ O ₁₂	9.27 x 10 ²²	0.0	0.2	3.1
ZnO	9.90 x 10 ²²	0.0	0.6	4.7

From *Table 3.2*, a general increase in the number monolayers removed is seen with increasing ion energy and ion atomic mass. Out of all the calculations, the worst case scenario corresponded to a maximum of ~5 monolayers removed by the O⁺ irradiation of zinc oxide. The lattice parameters of a single crystal ZnO with a hexagonal crystal structure is $a = b = 3.252 \text{ \AA}$, $c = 5.313 \text{ \AA}$.⁵ With a total of ~5 monolayers removed from the surface; the total surface thickness removed is only on a scale of ~1-3 nm. These values are negligible compared to the projected

range of the ions found in *Table 3.1*, wherein the shortest range was 380 nm, and shows that sputtering is not a concern under the experimental conditions of this work.

3.3 – Damage Created by Ion Irradiation

In this work, the damage created by ion irradiation was described in terms of the total dpa. Dpa was calculated using the number of vacancies output from the 2013 SRIM calculations as discussed in Chapter 1. The 2013 SRIM output lists the number of vacancies of each target element created by the ion as a function of penetration depth.² In order to find the total dpa, the output was integrated over the entire penetration depth of the ions and added over all target elements.

While the total damage is due to both the vacancies created and also the amount of replacement collisions, it was determined that for the ion irradiation conditions used in this work the contribution of replacement collisions to the total damage was minimal, when compared to the number of vacancies created, and therefore ignored. For example, the 2013 SRIM output data for the calculation of dpa created by O⁺ irradiation of ZnO determined that 16 replacement collisions per ion occurred with total target displacements of 954 per ion. This leads to a replacement collision contribution of 1.7%. Consequently, in this work, total dpa refers to the total amount of vacancies created by ion irradiation.

Analysis of the number of vacancies created per target element revealed that in YVO₄, LiNbO₃, Y₃Al₅O₁₂, and ZnO oxygen was the main contributor to vacancy creation. In MgAl₂O₄, aluminum was the main contributor to vacancy creation with values ranging from 45% for 60 keV H⁺ calculations to 42% for 1 MeV O⁺ calculations. This result is supported by the higher displacement energy required for oxygen atoms in MgAl₂O₄ when compared to aluminum atoms

(cf. Table 2.1). The total dpa and the respective fraction in percent of the element most contributing to vacancy creation for each material can be found in Table 3.3.

Table 3.3: Total dpa and the relative contribution of the element most contributing to vacancy creation in parenthesis (%).

Material	Density (g/cm ³)	Most Contributing Element	60 keV H ⁺	120 keV He ⁺	1 MeV O ⁺
MgAl ₂ O ₄	3.60	Al	1.5 (45)	16 (43)	207 (42)
YVO ₄	4.22	O	1.9 (60)	23 (61)	325 (63)
LiNbO ₃	4.30	O	1.5 (61)	18 (61)	249 (63)
Y ₃ Al ₅ O ₁₂	4.57	O	1.5 (56)	19 (56)	257 (57)
ZnO	5.675	O	1.2 (51)	16 (52)	237 (54)

As shown in Table 3.3, there is a general increase in the total dpa created with increasing ion energy and mass. Overall, this increase is in agreement with the expected behavior since higher ion energies result in more transferable energy available during nuclear collisions, resulting in a greater likelihood of vacancy formation.⁴ In Table 3.3, for each ion, yttrium vanadate is shown to have the highest total dpa. This result can be explained in part by the theoretical expression for energy transferred (E_t) during every ion beam collision with target atoms⁶

$$E_t/E_0 = (4m_0M)/(m_0 + M)^2 \quad (3.3)$$

where E_0 is the incident energy, m_0 is the mass of the incident particle, and M is the mass of the host lattice atom. From this expression, it can be observed that the ratio of energy transferred is highest when the incident particle is striking a lower atomic weight lattice atom, and oxygen is the lowest atomic weight atom in every material. Furthermore, YVO₄ has the highest atomic percentage of oxygen atoms in its structure (66.6%). This highest atomic percentage of oxygen allows for the incident ions to have the greatest probability of undergoing nuclear collisions with

the oxygen atoms in YVO_4 . Therefore, an increase of probability of striking an oxygen atom in YVO_4 , along with the highest ratio of energy transferred during collisions with oxygen atoms, results in the most damage in YVO_4

CHAPTER FOUR

MAGNESIUM ALUMINATE SPINEL RESULTS AND DISCUSSION

4.1 – 2013 SRIM Calculations

4.1.1 – Calculated Range of Ions

Calculations of the projected longitudinal and latitudinal depth of irradiation ions in MgAl_2O_4 were executed with the 2013 SRIM code (*cf. Table 3.1*). 2013 SRIM Monte Carlo calculations of ion irradiation damage were also executed. In *Figure 4.1*, a total of 1000 ions were used to illustrate these calculations. 2013 SRIM assigns different colors to both the incident ion and the target elements in order to visually observe the effects of nuclear and electronic energy loss. For MgAl_2O_4 , the 2013 SRIM code color assignments for different target atoms that are moving and stopped can be found in *Table 4.1*.

Table 4.1: Differentiating moving and stopped MgAl_2O_4 atoms by color.

Target Atom	Mg	Al	O
Color	moving	orange	light blue
	stopped	green	dark blue
		dark blue	purple

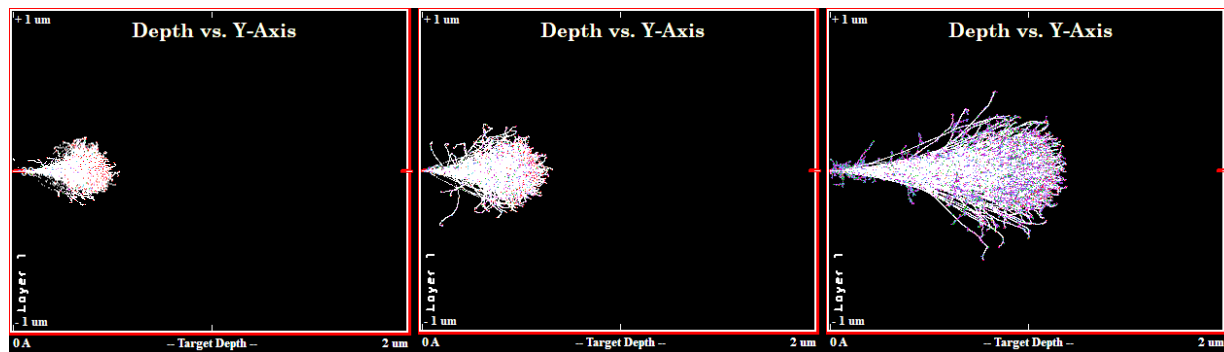


Figure 4.1: Ion trajectories in MgAl_2O_4 calculated using 2013 SRIM: H^+ (left), He^+ (middle), and O^+ (right).

4.1.2 – Nuclear and Electronic Energy Loss

The 2013 SRIM code was used to calculate the nuclear, electronic, and total energy loss of the incident ions in MgAl_2O_4 . These results can be found in *Figure 4.2* below.

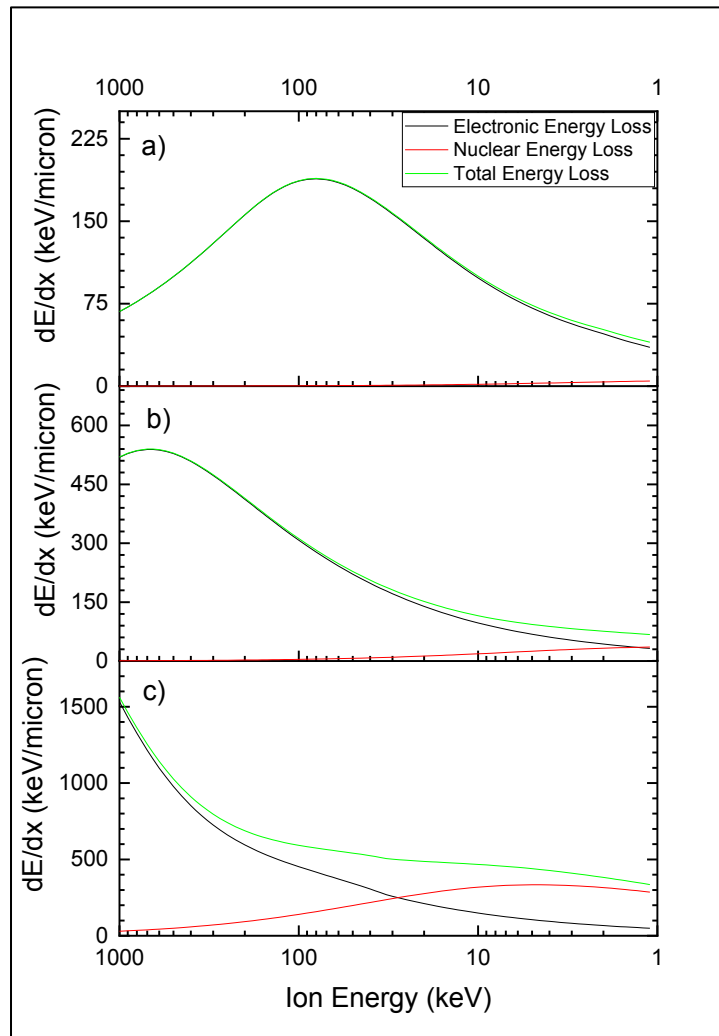


Figure 4.2: Electronic, nuclear, and total energy loss in MgAl_2O_4 for a) H^+ , b) He^+ , and c) O^+ ions.

From these results, it is apparent that O^+ ions in MgAl_2O_4 have the highest nuclear energy loss. For H^+ and He^+ , energy loss is dominated by the electronic energy loss for most of the energy range, while for O^+ nuclear energy loss dominates below about 30 keV. Also, as previously

mentioned in Chapter 1, nuclear collisions are responsible for the creation of defects in the target material. Therefore, these results explain the total dpa calculations for MgAl_2O_4 that list O^+ ions responsible for the most damage creation amongst all ions investigated (*cf. Table 3.3*).

4.1.3 – Damage Depth Distribution

The 2013 SRIM code was used to calculate damage depth distribution in terms of dpa for each target element of MgAl_2O_4 . These results can be found in *Figure 4.3*.

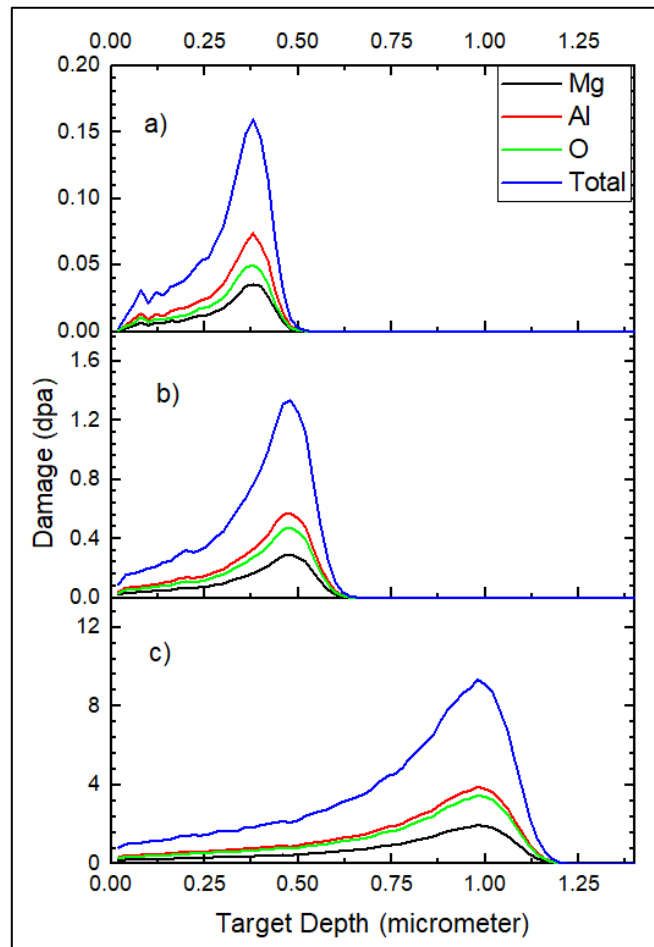


Figure 4.3: Damage depth distribution of a) H^+ , b) He^+ and c) O^+ ion irradiations in MgAl_2O_4 .

From these results, it is apparent that irradiation with O^+ ions leads to the furthest projected range in $MgAl_2O_4$, which supports previous calculations (*cf. Table 3.1*). For all three ions, it can be observed that the creation of vacancies from displaced aluminum target atoms is the leading cause of damage in $MgAl_2O_4$, with their percentages previously discussed in *Table 3.3*.

4.2 – Raman Spectroscopy

Raman spectroscopy measurements were obtained in order to evaluate the effects of ion irradiation on the structure of $MgAl_2O_4$. The results of these measurements can be found in *Figure 4.4*.

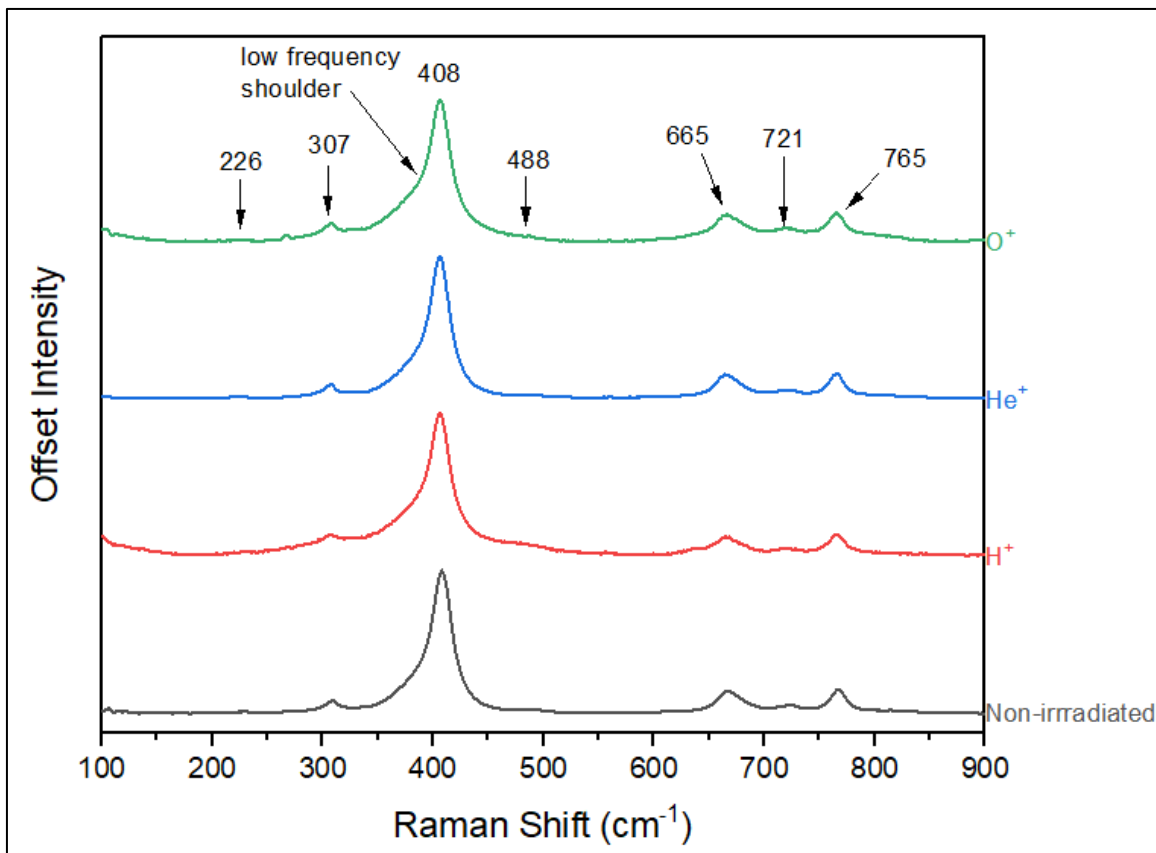


Figure 4.4: Raman spectra of pristine and irradiated $MgAl_2O_4$ samples offset by intensity.

From the Raman spectroscopy measurements, the presence of seven peaks was observed in each sample in addition to a low-frequency shoulder present on the peak at $\sim 408\text{ cm}^{-1}$. The seven observed peaks were compared with previous literature to determine the identity of the vibrational modes that were measured. It was determined that the following vibrational modes were present: 226 cm^{-1} is the translation of Al^{3+} in a tetrahedral site, 307 cm^{-1} is the translation of Mg^{2+} in a tetrahedral site, 408 cm^{-1} is related to internal vibrations of Al^{3+} in a octahedral site, 488 cm^{-1} (unknown vibration mode), 665 cm^{-1} is related to internal vibrations of Al^{3+} in a octahedral site, and 765 cm^{-1} is the symmetric Mg – O stretching vibration in a tetrahedral site. The 721 cm^{-1} peak is related to the symmetric Al – O stretching vibration in a tetrahedral site but is also from active photons in the disordered structure due to internal coupling with the Mg – O vibration. The low-frequency shoulder was attributed to the vibrational bending mode of Al^{3+} in tetrahedral sites.¹

Raman spectra for all MgAl_2O_4 samples were normalized to the peak of greatest intensity (408 cm^{-1}) in order to determine its possible shift in peak position and changes in its peak FWHM. Changes in the peak position after being corrected by the neon lamp reference can be found in *Table 4.2*. However, changes in the peak FWHM could not be determined, due to the presence of the low-frequency shoulder (*Figure 4.5*). Therefore, changes in the peak position and FWHM were also conducted after normalizing the spectra to the peak at 765 cm^{-1} . These results are also found in *Table 4.2*.

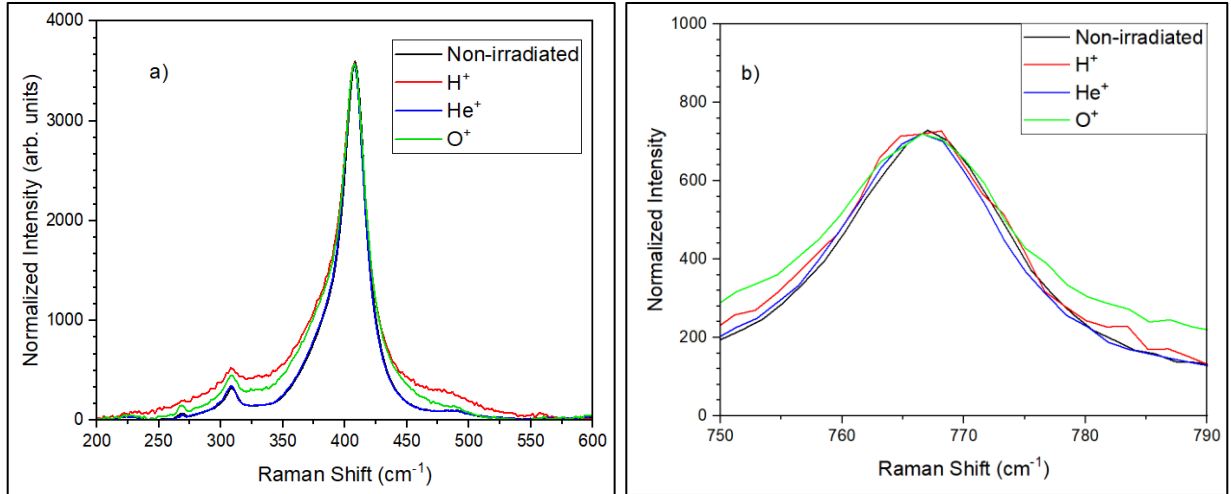


Figure 4.5: Overlay of pristine and irradiated MgAl_2O_4 Raman spectra after normalization and correction at a) 408 cm^{-1} and b) 765 cm^{-1} .

Table 4.2: Changes in peak position and FWHM for MgAl_2O_4 Raman spectra.

Sample	Peak Location (cm^{-1})		Peak FWHM
	408 cm^{-1}	765 cm^{-1}	
Non-irradiated	408.1	767.0	14.4
H^+	407.5	766.9	15.3
He^+	407.6	767.0	14.0
O^+	407.6	766.8	17.0

Analysis of the shifts in peak position due to ion irradiation of the MgAl_2O_4 samples revealed that the greatest shift was $\sim 0.6\text{ cm}^{-1}$ between the pristine sample and the H^+ irradiated sample at the 408 cm^{-1} peak. This shift in peak position was determined to be within the experimental uncertainty under the experimental conditions used in this work. For comparison, previous literature reported Raman spectra peak shifts of 3 cm^{-1} or greater due to structural strain induced by ion irradiation of ceramic samples.² Therefore, while it is possible that some peak shift may have happened in irradiated MgAl_2O_4 , the magnitude of the strain causing the shift is expected to be low, if any.

The observed change in the low-frequency shoulder for the H⁺ and O⁺ irradiated samples in *Figure 4.5a* was attributed to the creation of anti-site defects by the incident H⁺ and O⁺ ions. Both H⁺ and O⁺ are reactive chemical species, and displacement of a target atom can allow these ions to bond with the structure and stabilize the created defects. In agreement with this, no change in the intensity of the low frequency shoulder was observed for the He⁺ irradiated MgAl₂O₄ (it perfectly superimposes to the spectrum of the pristine sample) likely due to helium's non-reactive nature as a noble gas.

Analysis of the change in peak FWHM at the 765 cm⁻¹ peak shows an increase in peak width due to O⁺ and possible H⁺ irradiations. These results are in agreement with those related to the low-frequency shoulder of the peak at 408 cm⁻¹. This increase in peak FWHM is interpreted to being due to the creation of structural disorder and supports previous calculations that determined the irradiation of O⁺ ions results in the highest number of defects created (*i.e.*, highest dpa). It is also in agreement with the increasing presence of anti-site defects as per the analysis of the shoulder of the 408 cm⁻¹ peak.

4.3 – UV-Visible Optical Spectroscopy

UV–visible optical spectroscopy measurements were conducted in order to determine the effects of ion irradiation on the creation and intensity of the absorbance bands in MgAl₂O₄ and general transmittance of light. The results of these measurements can be found in *Figure 4.6*.

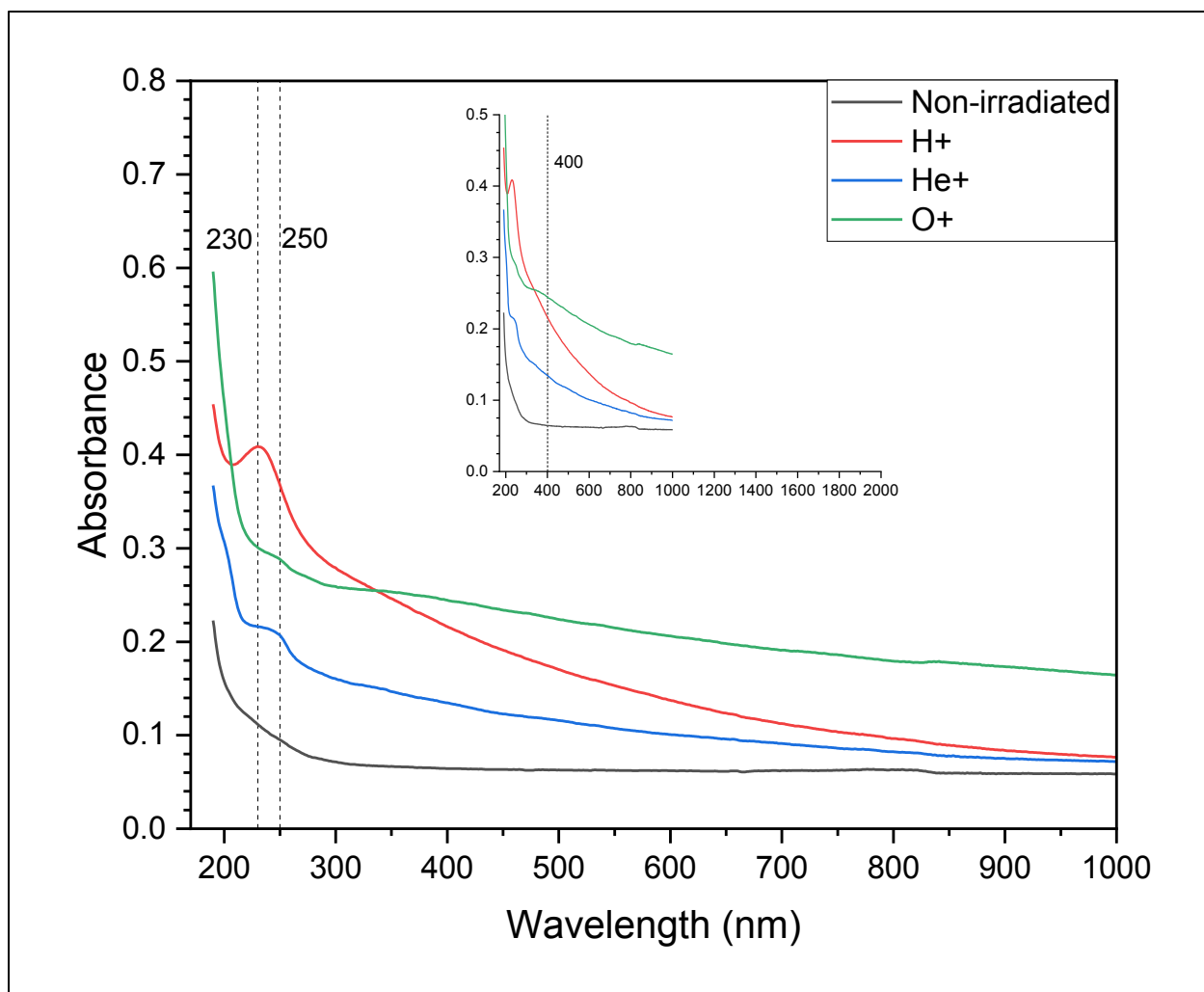


Figure 4.6: Optical absorption spectra of pristine and irradiated MgAl_2O_4 samples. The inset shows the same results at a difference scale to highlight the broad-band centered at ~ 400 nm.

From these results, there is clear evidence of the creation of an absorption band in the irradiated samples around 230 – 250 nm. Previous studies of irradiation effects on MgAl_2O_4 attribute this absorption band to the creation of F centers.³⁻⁵ The intensity of the absorption band is higher in both H^+ and He^+ irradiated samples than the O^+ irradiated sample, even though 2013 SRIM calculations showed the highest total dpa occurs for O^+ irradiation of MgAl_2O_4 (*cf. Table 3.3*). This discrepancy can be explained by the ability of the incident O^+ ion to recombine and “fill” F centers (an F center corresponds to an O vacancy containing two electrons), resulting in a lower

absorption band intensity. The inserted spectrum of the irradiated samples shows an additional absorption band due to O⁺ irradiation centered at ~400 nm. This band has been attributed to V-type defects (*i.e.*, related to vacancy creation in the MgAl₂O₄ structure).⁴ These results support the 2013 SRIM calculations that show O⁺ irradiation leads to the highest number of defects (vacancies).

An overall increase in the baseline absorption (loss of optical transparency) can be seen in all irradiated samples when compared to pristine MgAl₂O₄. This shift in absorption can be explained by an increase in Rayleigh scattering due to the creation of point defects (vacancies, interstitials, *etc.*) by ion irradiation that alter the index of refraction of the host locally. Rayleigh scattering is given by the general expression:⁶

$$I_s = I_0 \left(\frac{9\pi^2 V^2}{2r^2 \lambda^4} \right) \left(\frac{m^2 - 1}{m^2 + 2} \right)^2 (1 + \cos^2 \theta) \quad (4.1)$$

where V is the volume of the scattering center, λ is the wavelength of light, r is the distance from the scattering center, θ is the angle between the incident beam and the scattered beam, and m is a ratio between the index refraction of the scattering centers and that of the medium. The creation of point defects will result in an increase of scattering centers, thereby decreasing the intensity of light transmitted through the material. However, the spectrometer cannot differentiate if the loss of transparency was due to absorption or scattering, since it is only capable of determining the intensity of light reaching the detector not its cause. As per *equations 2.2 and 2.3*, this decrease in transmitted light is automatically attributed to absorption, thus requiring attention in the interpretation of the results. A trend of increasing number of defects caused by irradiation as determined from 2013 SRIM calculations (total dpa; *Table 3.3*) with an increasing shift in absorption for H⁺, He⁺, and O⁺ samples, respectively, further supports this analysis. Also, the

intensity of the Rayleigh scattering scales with $\frac{1}{\lambda^4}$ and thus absorption is expected to progressively increase for shorter wavelengths as it is observed in *Figure 4.6*.

4.4 – Radioluminescence

RL measurements were conducted to determine the identity and possible change of relative intensities of luminescence bands (and thus of the concentrations of luminescence centers) due to ion irradiation of MgAl_2O_4 . These measurements can be found in *Figure 4.7*.

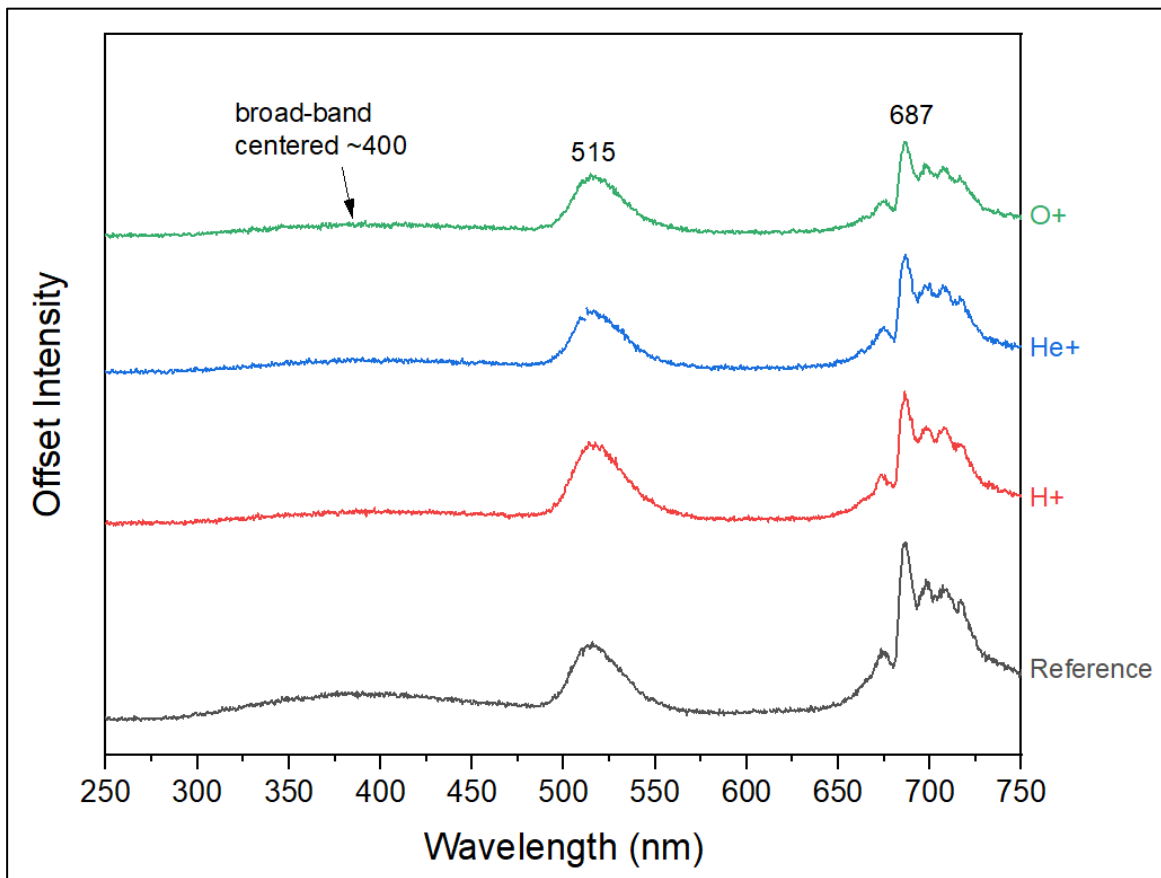


Figure 4.7: Offset RL spectra of pristine and irradiated MgAl_2O_4 samples.

From these results, three distinct luminescence bands were observed including a broad-band centered at ~400 nm, a narrower band at ~515 nm, and a series of sharp bands peaked at 687 nm. Previous literature on the identity of these luminescent bands determined that the following were present: the broad-band peak centered at 400 nm has been attributed to multiple defects such as F centers, F⁺ centers, and anti-site defects, the 515 nm band has been attributed to Mn²⁺ impurities in octahedral sites, and the peaks centered around 687 nm are attributed to a combination of defects including color centers from Mg vacancies and Cr³⁺ impurities.¹ Since the optical transparency of the samples changed due to ion irradiation, the absolute RL intensity of the bands cannot be compared. Consequently, the relative intensity of the peaks was compared to investigate possible changes due to ion irradiation. These results can be found in *Table 4.3*.

Table 4.3: Intensity ratio of RL peaks in pristine and irradiated MgAl₂O₄ samples.

Sample	Peak Ratio		
	400 nm/515 nm	400 nm/687 nm	515 nm/687 nm
Non-irradiated	0.35	0.15	0.42
H ⁺	0.17	0.10	0.61
He ⁺	0.21	0.11	0.52
O ⁺	0.22	0.14	0.64

Table 4.3 reveals that the intensity of all bands changed due to ion irradiation and thus none of them can be used as a fixed reference for the others. This limited the analysis of the RL measurements to the identification of the luminescence bands present in the samples only.

4.5 – Thermoluminescence

TL measurements were conducted to investigate how traps were affected by ion irradiation.

The results of these measurements can be found in *Figure 4.8* below.

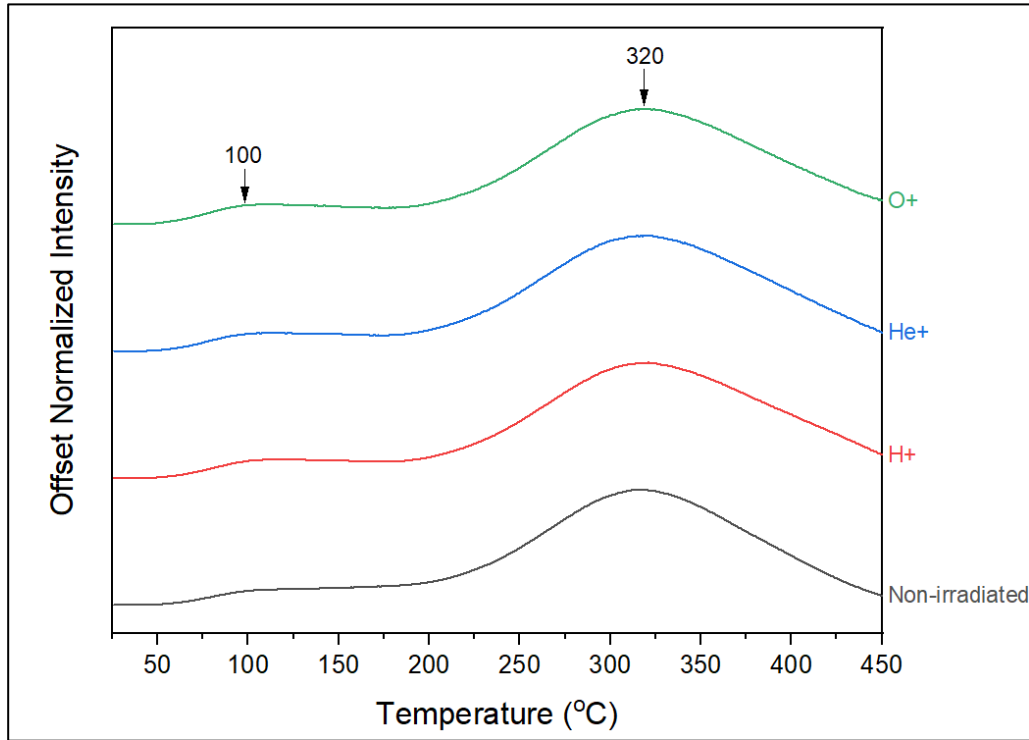


Figure 4.8: Glow curves of pristine and irradiated MgAl₂O₄ samples..

From these results, two distinct glow peaks were observed in each MgAl₂O₄ sample, one at ~100 °C and the other at ~320 °C. Previous literature has reported these two distinct peaks in MgAl₂O₄ at ~70 °C and ~290 °C when using the same heating rate of 1 °C/s. The identity of these peaks have been previously investigated and suggested to be: the 70 °C glow peak was attributed to the escape of electrons from shallow traps (~ 1 eV deep) caused by Al³⁺ on Mg²⁺ sites (*i.e.*, anti-site defects), and the 290 °C glow peak to be attributed to electron hole release and recombination at Cr³⁺ sites.⁷⁻⁹ No significant peak shifts due to ion irradiation were observed. Like in the case of

RL, the changes in the optical transparency of the samples due to ion irradiation hindered the comparison of the absolute TL intensity of the bands. Consequently, the relative intensity of the peaks was compared to investigate possible changes due to ion irradiation. The relative intensity of the ratio of peak I (at 100 °C) to peak II (at 320 °C) was analyzed and is presented in *Table 4.4*.

Table 4.4: Intensity ratio of TL peak I to peak II for MgAl₂O₄ samples.

Sample	Non-irradiated	H ⁺	He ⁺	O ⁺
Ratio	0.15	0.17	0.17	0.19

These results show a systematic increase of the relative intensity from H⁺ to He⁺ to O⁺ that agrees with the increase of dpa.

TL spectroscopy measurements were conducted to determine the identity of the recombination centers leading to the two distinct peaks seen in the TL measurements (*Figure 4.8*). The results of these measurements can be found in *Figure 4.9*.

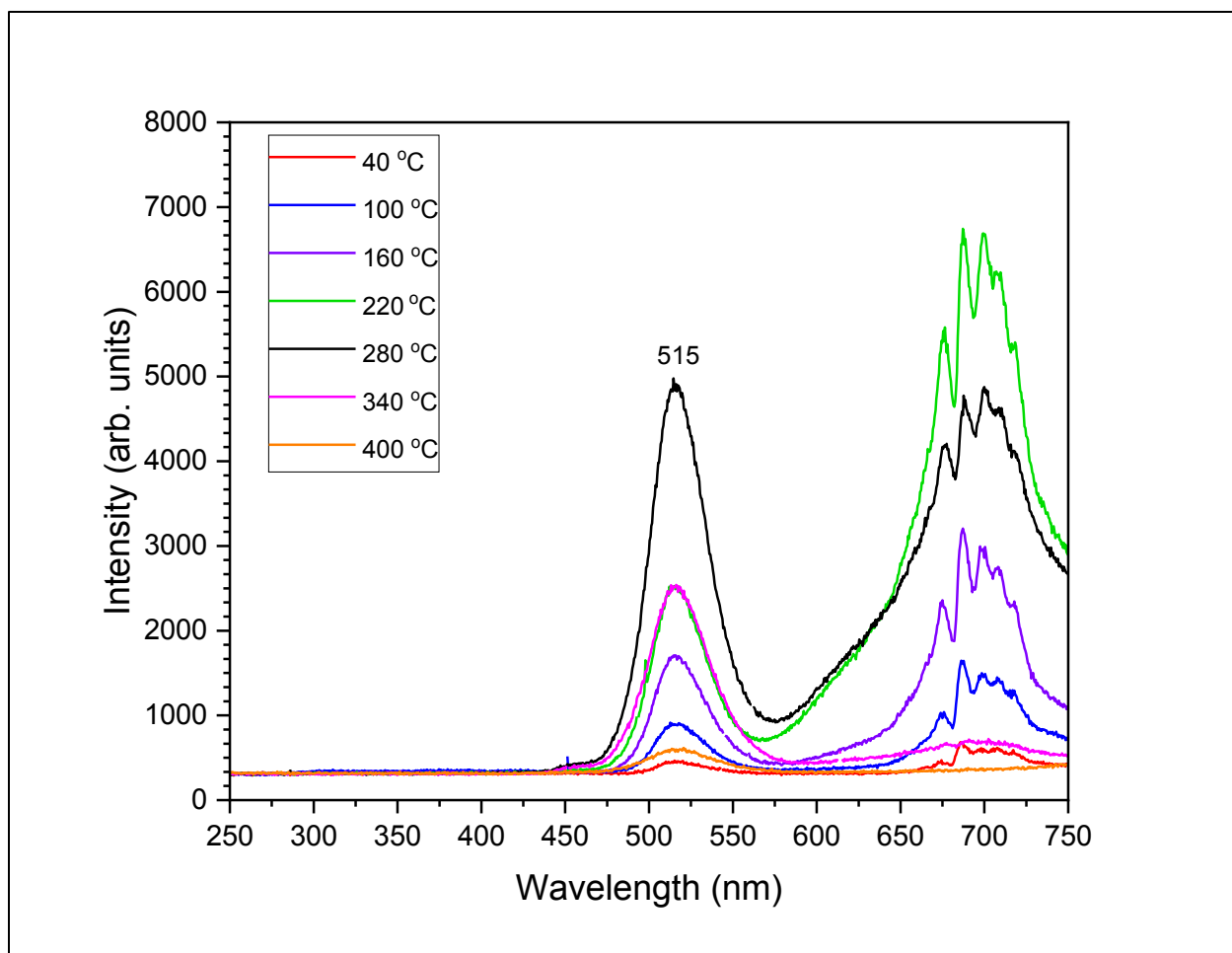


Figure 4.9: TL spectroscopy results of pristine MgAl_2O_4 .

These results show for all temperatures up to 400 °C a peak at 515 nm due to Mn^{2+} along with several peaks composing a complex band previously identified as from Cr^{3+} impurities. The presence of color centers from Mg vacancies is evident in the ‘340 °C’ spectrum due to the thermal quenching of Cr^{3+} . When comparing these spectra with RL measurements (*Figure 4.7*), it is clear that Mn^{2+} and Cr^{3+} impurities participate in the TL process with no contributions from anti-site defects (broad band around 400 nm).

TL reproducibility measurements were conducted to determine the possibility of electron traps existing at deeper energies in the sample seeping electrons to lower energy traps and thus

changing the TL glow curves in time. The results of these measurements can be found in *Figure 4.10*.

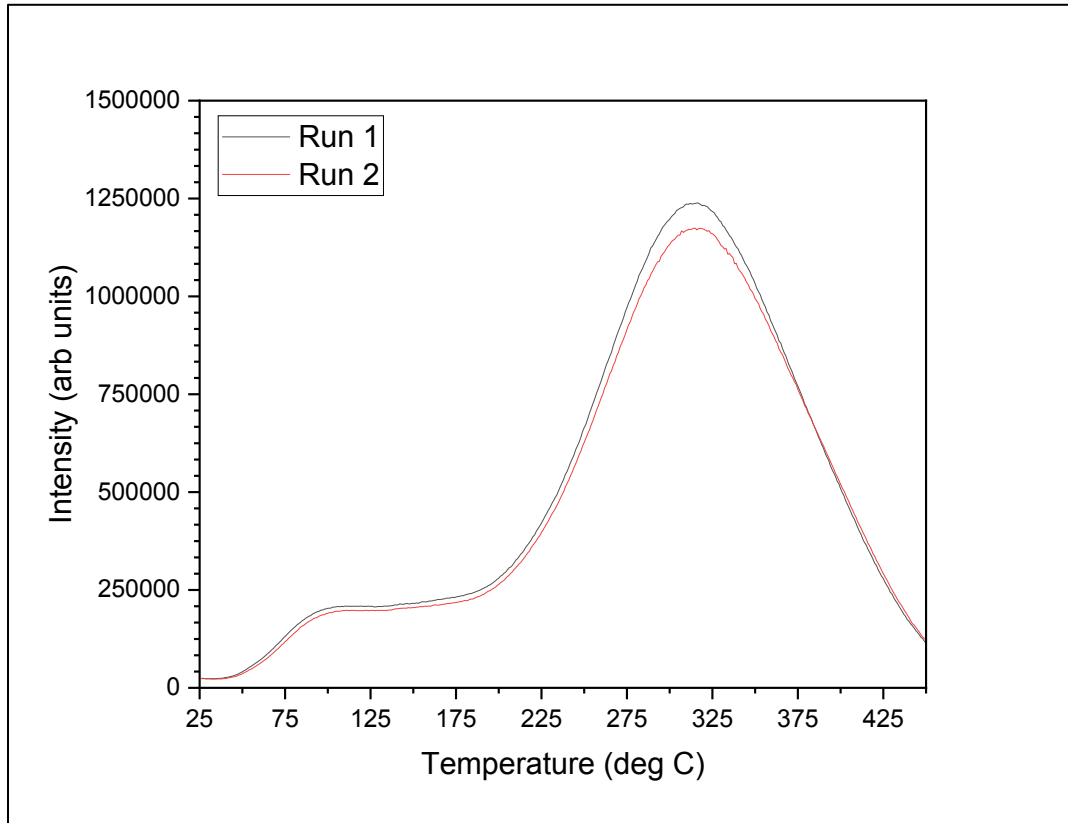


Figure 4.10: TL reproducibility measurements of pristine MgAl₂O₄.

From these TL curves, a change in peak intensity (~5%) is observed for both peaks. The decrease in peak intensity in such short period of time revealed substantial fading, *i.e.*, a phenomenon when trapped electrons are slowly released from their traps by room temperature thermal energy. As such, no inference of the contribution of deeper traps could be made. Also, the relative intensity of the bands changed, revealing TL response to be sensitive to the (X-ray) irradiation history.

4.6 – Summary of Results

In summary, Raman spectroscopy, optical absorption, and TL results showed clear effects of ion irradiation, particularly the creation of defects associated with oxygen vacancies and anti-site defects. While anti-site defects were more sensitive to irradiation with chemically reactive ions (H^+ and O^+), O vacancies were more effectively produced by H^+ and He^+ in opposition to O^+ ions, likely due to structural 'healing' by the O^+ ions.

CHAPTER FIVE

YTTRIUM ALUMINUM GARNET RESULTS AND DISCUSSION

5.1 – 2013 SRIM Calculations

5.1.1 – Calculated Range of Ions

Calculations of the projected longitudinal and latitudinal depth of irradiation ions in $Y_3Al_5O_{12}$ were executed with the 2013 SRIM code (*cf. Table 3.1*). 2013 SRIM Monte Carlo calculations of ion irradiation damage were also executed. In *Figure 5.1*, a total of 1000 ions were used to illustrate these calculations. 2013 SRIM assigns different colors to both the incident ion and the target elements in order to visually observe the effects of nuclear and electronic energy loss. For $Y_3Al_5O_{12}$, the 2013 SRIM code color assignments for different target atoms that are moving and stopped can be found in *Table 5.1*.

Table 5.1: Differentiating moving and stopped $Y_3Al_5O_{12}$ atoms by color.

Target Atom	Y	Al	O
Color	moving	orange	light blue
	stopped	green	dark blue
		purple	

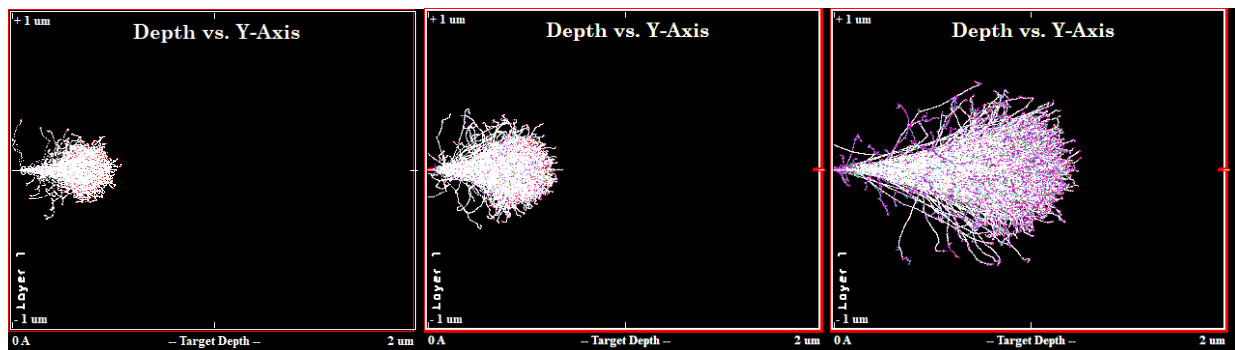


Figure 5.1: Ion trajectories in $Y_3Al_5O_{12}$ calculated using 2013 SRIM: H^+ (left), He^+ (middle), and O^+ (right).

5.1.2 – Nuclear and Electronic Energy Loss

The 2013 SRIM code was used to calculate the nuclear, electronic, and total energy loss of the incident ions in $Y_3Al_5O_{12}$. These results can be found in *Figure 5.2* below.

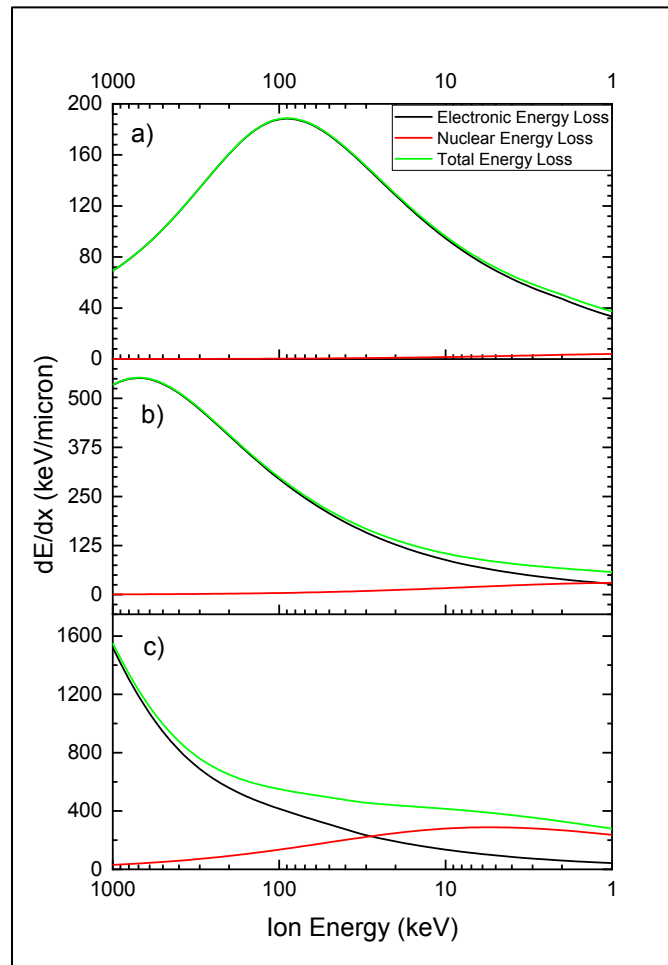


Figure 5.2: Electronic, nuclear, and total energy loss in $Y_3Al_5O_{12}$ for a) H^+ , b) He^+ , and c) O^+ ions.

From these results, it is apparent that O^+ ions in $Y_3Al_5O_{12}$ have the highest nuclear energy loss. For H^+ and He^+ , energy loss is dominated by the electronic energy loss for most of the energy range, while for O^+ nuclear energy loss dominates below about 30 keV. Also, as previously mentioned in Chapter 1, nuclear collisions are responsible for the creation of defects in the target

material. Therefore, these results explain the total dpa calculations for $Y_3Al_5O_{12}$ that list oxygen ions responsible for the most damage creation amongst all ions used in this work (*cf. Table 3.3*).

5.1.3 – Damage Depth Distribution

The 2013 SRIM code was used to calculate damage depth distribution in terms of dpa for each target element of $Y_3Al_5O_{12}$. These results can be found in *Figure 5.3*.

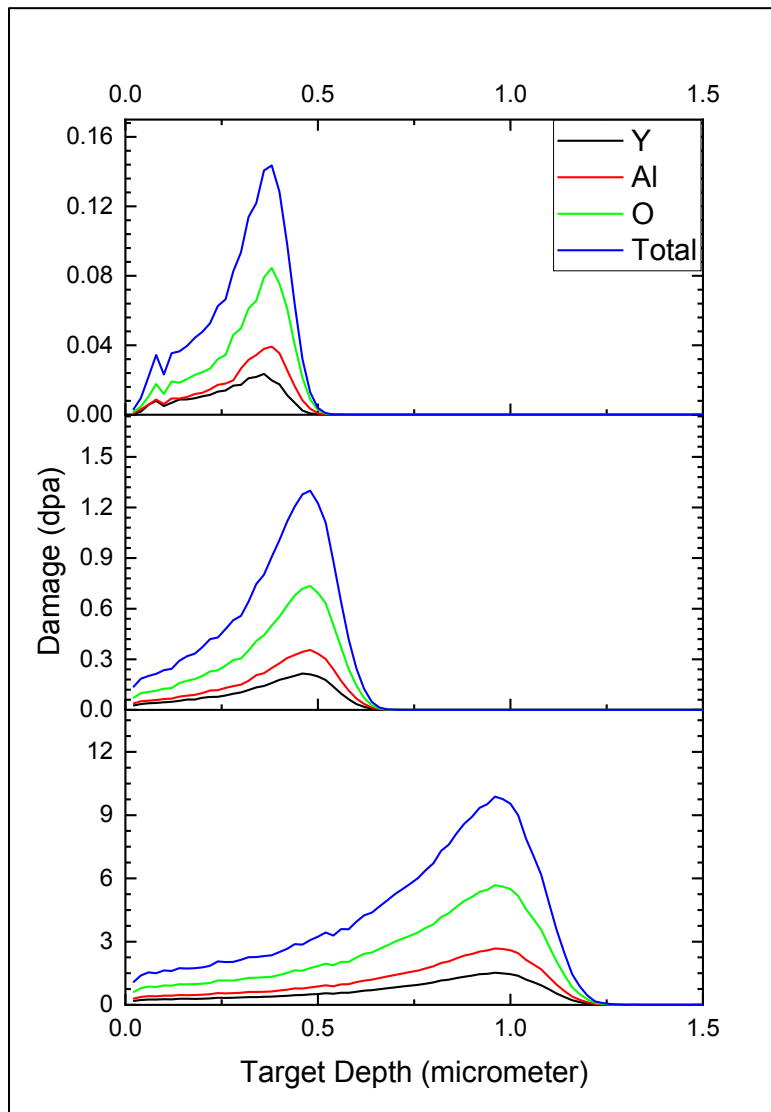


Figure 5.3: Damage depth distribution for a) H^+ , b) He^+ , and c) O^+ ion in $Y_3Al_5O_{12}$.

From these results, it is apparent that irradiation with oxygen ions leads to the furthest projected range in $Y_3Al_5O_{12}$, which supports previous calculations (*cf. Table 3.1*). For all three ions, it can be observed that the creation of vacancies from displaced oxygen target atoms is the leading cause of damage in $Y_3Al_5O_{12}$, with their percentages previously discussed in *Table 3.3*.

5.2 – Raman Spectroscopy

Raman spectroscopy measurements were obtained in order to evaluate the effects of ion irradiation on the structure of $Y_3Al_5O_{12}$. The results of these measurements can be found in *Figure 5.4*.

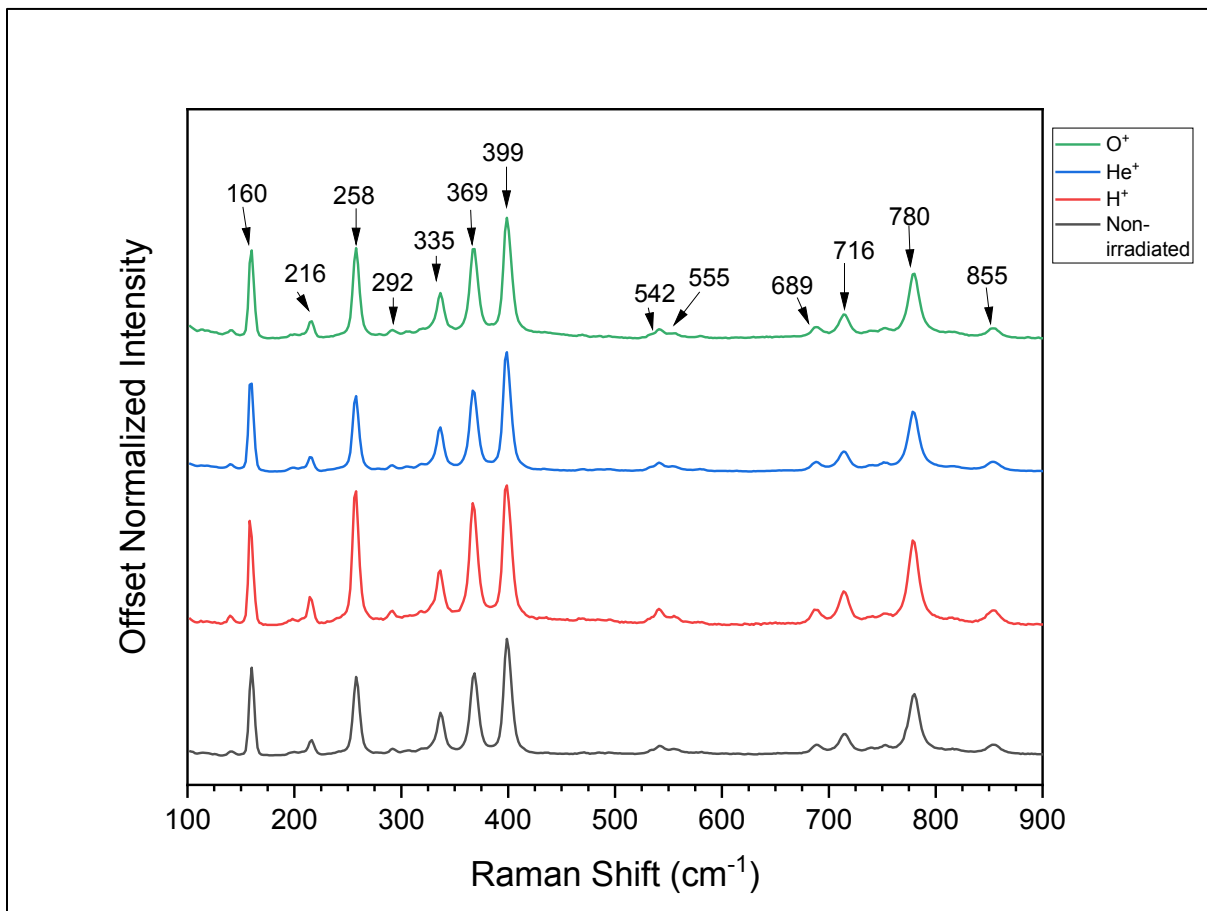


Figure 5.4: Raman spectra of pristine and irradiated $Y_3Al_5O_{12}$ samples offset by intensity.

From the Raman spectroscopy measurements, the presence of 13 major peaks were observed in each sample. These peaks were compared with previous literature to determine the identity of the vibrational modes that were observed. The peaks and their corresponding vibrational modes can be found in *Table 5.2*.¹

Table 5.2: Identification of the vibrational modes of $Y_3Al_5O_{12}$.¹

Raman Shift (cm^{-1})	Vibrations
160, 216	Y^{3+} translation
258, 292, 335, 369, 399	Translation + rotation of (AlO_4)
542, 555	Rotation of (AlO_4)
689, 716, 780, 855	Asymmetric bending + internal vibrations of (AlO_4)

Raman spectra of all $Y_3Al_5O_{12}$ samples were normalized to the peak of greatest intensity that had the least superposition from nearby peaks (160 cm^{-1}). The spectra were also corrected by the neon lamp reference towards the determination of possible shifts in peak position. Changes in the peak FWHM were also evaluated (*Figure 5.5*).

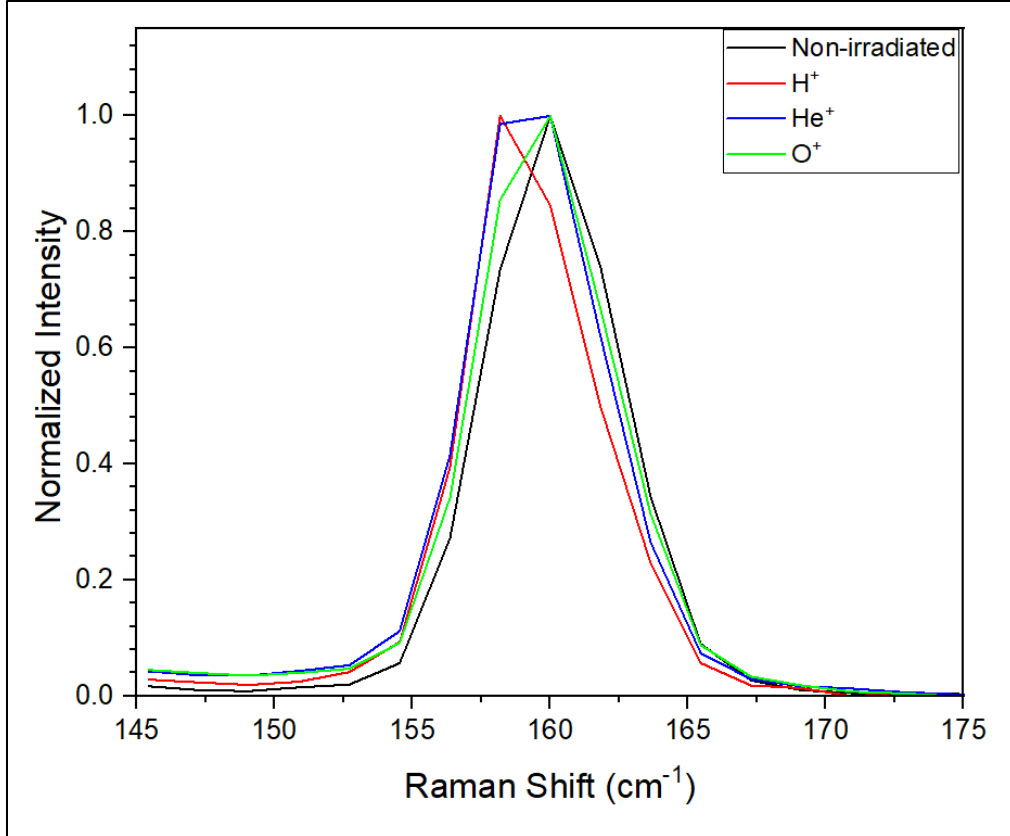


Figure 5.5: Overlay of pristine and irradiated $Y_3Al_5O_{12}$ Raman spectra after normalization and position correction.

Table 5.3: Changes in the peak location and peak FWHM for $Y_3Al_5O_{12}$ Raman spectra.

Sample	Peak Location (cm^{-1})	Peak FWHM (cm^{-1})
Non-irradiated	160.0	5.6
H ⁺	159.2	5.0
He ⁺	159.2	5.6
O ⁺	159.3	5.8

Analysis of the shifts in peak position due to ion irradiation of the $Y_3Al_5O_{12}$ samples revealed that the greatest shift was $\sim 0.8 \text{ cm}^{-1}$ between the pristine sample and the H⁺ and He⁺ irradiated samples (*Table 5.*). The analysis of the peak broadening did not reveal a significant change of the FWHM of the irradiated samples when compared to the non-irradiated one (*Table*

5.3). The magnitudes of the peak shift and of the changes in the peak FWHM were determined to be within the experimental uncertainty under these experimental conditions. Therefore, the strain created by ion irradiation, if any, was not significant.

5.3 – UV-Visible Optical Spectroscopy

UV-visible optical spectroscopy measurements were conducted in order to determine the effect of ion irradiation on the intensity of the absorbance bands in $Y_3Al_5O_{12}$ and general transmittance of light. The results of these measurements can be found in *Figure 5.6*.

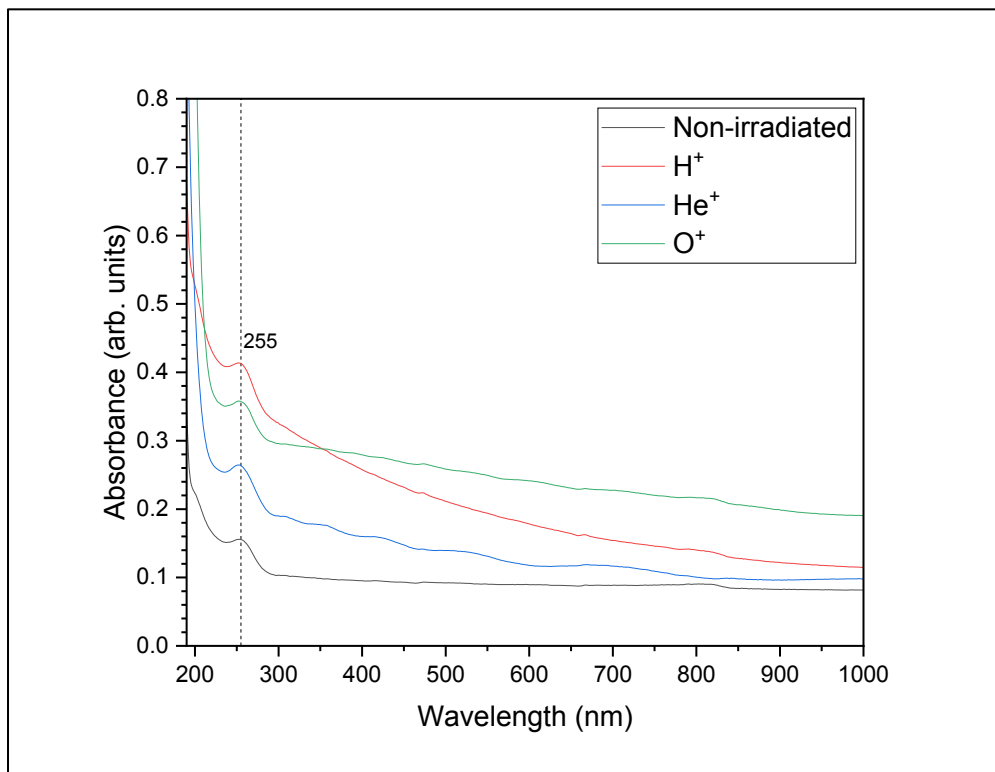


Figure 5.6: Optical absorption spectra of pristine and irradiated $Y_3Al_5O_{12}$ samples.

From these results, an absorption band at around 255 nm was observed in all samples. From the literature, an absorption/excitation band at 258 nm was attributed to F centers.² There is not a

clear increase or decrease in the absorption band intensity (in relation to the baseline of the respective spectrum) due to ion irradiation, therefore it is determined to be unaffected from the ion irradiation. All samples contain an intense absorption starting around 200 nm that has also been attributed to F centers.^{3,4} The oscillating pattern seen in the He⁺ irradiated Y₃Al₅O₁₂ has been attributed to light interference and should be disregarded.

An overall increase in the baseline absorption can be seen in all irradiated samples when compared to pristine Y₃Al₅O₁₂. This shift in absorption and its enhancement for lower wavelengths can be explained by an increase in Rayleigh scattering due to the creation of point defects due to ion irradiation as it was previously discussed in Chapter 4. An increase in absorption can be seen from the pristine sample to He⁺ followed by O⁺ irradiated samples in general agreement with total dpa. Presently, the behavior of the H⁺ irradiated sample is not well-understood.

5.4 – Radioluminescence

RL measurements were conducted to determine the identity and possible changes of relative intensity of the luminescence centers due to ion irradiation in Y₃Al₅O₁₂. These measurements can be found in *Figure 5.7*. Since the optical transparency of the samples changed due to ion irradiation, the absolute RL intensity of the bands cannot be compared.

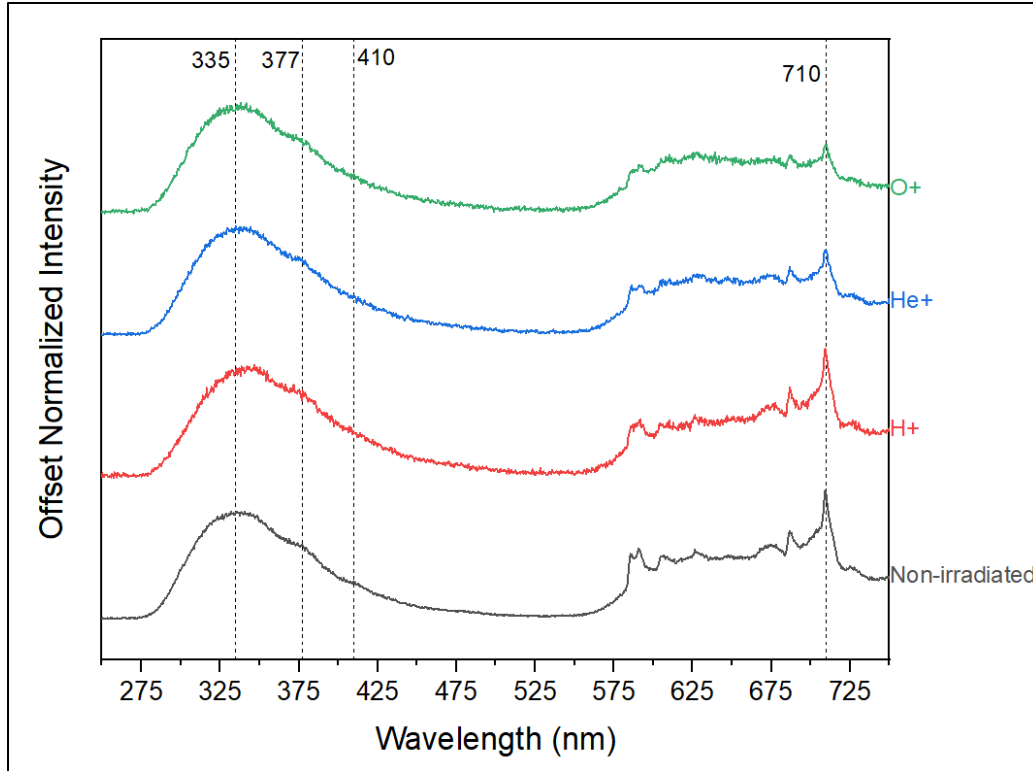


Figure 5.7: Offset RL spectra for pristine and irradiated $Y_3Al_5O_{12}$ samples.

The RL spectra can be divided into two distinct regions: a broad-band peak centered at ~ 335 nm with two shoulders at 377 and 410 nm, and a sharp peak at 710 nm together with multiple weaker peaks that compose a band within ~ 570 -730 nm. The identity of the broad-band peak at 335 nm has been attributed to anti-site defects⁵ while the 377 and 410 nm shoulders have been attributed to Y_{Al} anti-site defects and F^+ centers, respectively.^{2,4} The multiple peaks within ~ 650 -750 nm have been attributed to iron and/or chromium impurities.^{6,7} On the other hand, emission within ~ 570 -650 nm could not be identified.

It was possible to take advantage of the luminescence bands due to impurities, particularly the double feature around 585 nm and the peaks within ~ 680 -710 nm. Both features lose resolution and relative intensity in the irradiated samples when compared to the pristine sample, especially the O^+ irradiated sample, indicating structural damage.

5.5 – Thermoluminescence

TL measurements were conducted to investigate how traps were affected by ion irradiation.

The results of these measurements can be found in *Figure 5.8* below.

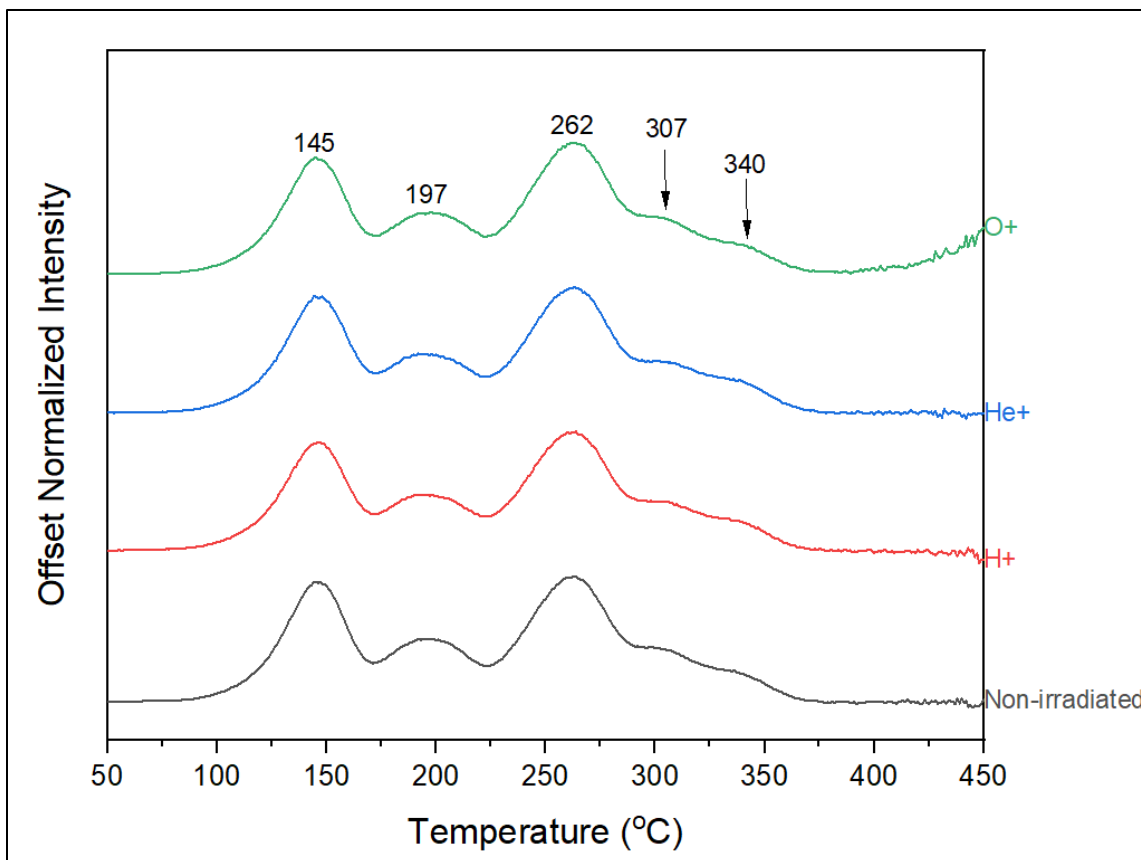


Figure 5.8: Glow curves of pristine and irradiated $Y_3Al_5O_{12}$ samples.

From the glow curve, the presence of three main glow peaks was observed at 145, 197 and 262 °C, with the final peak containing two shoulders at 307 and 340 °C. Previous literature on the glow curves of undoped $Y_3Al_5O_{12}$ have also identified the presence of these peaks, albeit, at slightly different temperatures due to differences in heating rates (10 °C/s).⁸ These experimental values compared to previous literature can be found in *Table 5.4*.⁸ The glow peak temperatures

observed in ref [8] were progressively at higher temperatures in agreement with the theory of TL. It is well-known that higher heating rates lead to TL glow peaks to be observed at higher temperatures.⁹ Visual analysis of each sample's glow curve revealed that no additional traps were created by ion irradiation.

Table 5.4: Peak (P) and shoulder (S) temperatures observed in the glow curve of $Y_3Al_5O_{12}$ in this work (heating rate = 1 °C/s) and from ref [8] (10 °C/s).

Parameter	Peaks				
	P1	P2	P3	S1	S2
This Work T (°C)	145	197	262	307	340
Literature T (°C)	157	209	259	323	389

The relative intensities of the glow curve peaks were analyzed to determine the effects of ion irradiation and the recombination center contribution and presented in *Table 5.5*.

Table 5.5: Intensity ratio of glow curve peaks in pristine and irradiated $Y_3Al_5O_{12}$ samples.

Sample	Peak Ratio		
	197 °C/145 °C	197 °C/262 °C	145 °C/262 °C
Non-irradiated	0.55	0.52	0.96
H ⁺	0.57	0.52	0.92
He ⁺	0.53	0.49	0.92
O ⁺	0.53	0.46	0.88

Overall, minor changes were observed in the relative intensity ratios related to the three main TL glow peaks in the glow curves of the pristine and irradiated samples. No changes were

observed in the relative intensities of the shoulders of the 262 °C peak. These results suggest the relative population of the traps not to be highly sensitive to radiation damage.

TL spectroscopy measurements were conducted to determine the identity of the recombination centers related to the distinct glow peaks observed in the glow curves (*Figure 5.8*).

The results of these measurements can be found in *Figure 5.9*.

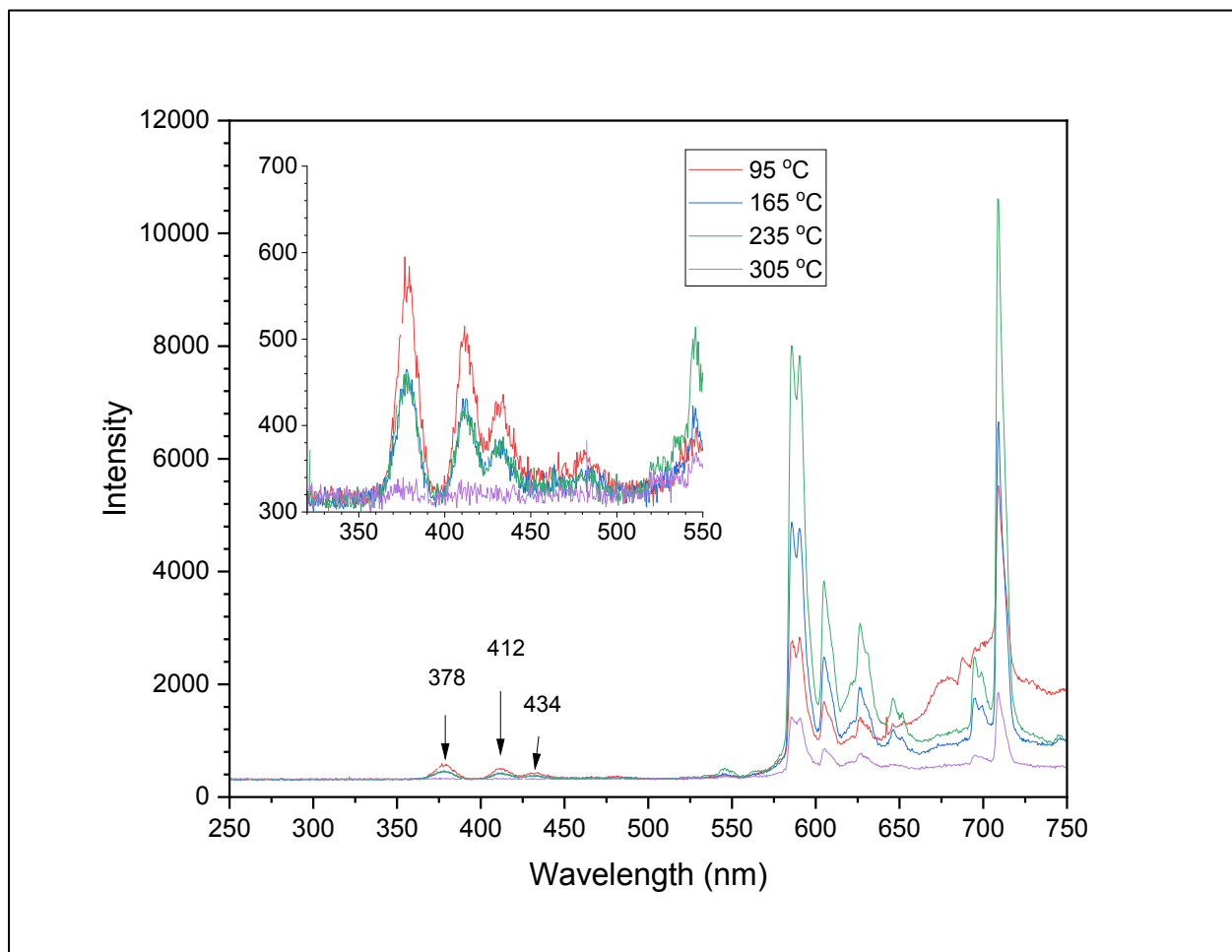


Figure 5.9: TL spectroscopy results of pristine $Y_3Al_5O_{12}$. The insert shows the same results at a different scale to highlight the luminescence bands within 325-550 nm.

From TL spectroscopy measurements, three weak luminescence centers were identified at 378, 412, and 434 nm, respectively, along with an additional broad range of peaks previously

identified as Cr^{3+}/Fe and other impurities (*cf. Figure 5.7*). A comparison with the previous RL spectra of $\text{Y}_3\text{Al}_5\text{O}_{12}$ samples determined the first two peaks to belong to the shoulders of the broad-band peak, identified as arising from Y_{Al} anti-site defects and F^+ centers, respectively. The third TL spectroscopy peak was not previously detected in the RL measurements likely for being a weak band on the tail of the intense 335 nm band, and its nature remains unknown. Analysis of the three peaks revealed a maximum luminescence contribution within 95-165 °C with a decreasing contribution with increasing temperature (thermal quenching). Above 305 °C, these three peaks were thermally quenched and, consequently, they no longer contributed to the TL process. These results showed that the anti-site defects related to the 335 nm band do not participate in the TL process. All other defects and impurities participate as recombination centers of the three main glow peaks with different efficiencies, depending on the temperature. However, only the impurities serve as recombination centers for the two high temperature shoulders (at 307 and 340 °C; *cf. Figure 5.8*) since they are still optically active at these high temperatures.

TL reproducibility measurements were conducted to determine the possibility of electron traps existing at deeper energies in the pristine $\text{Y}_3\text{Al}_5\text{O}_{12}$ sample affecting the glow curves. The results of these measurements can be found in *Figure 5.10*.

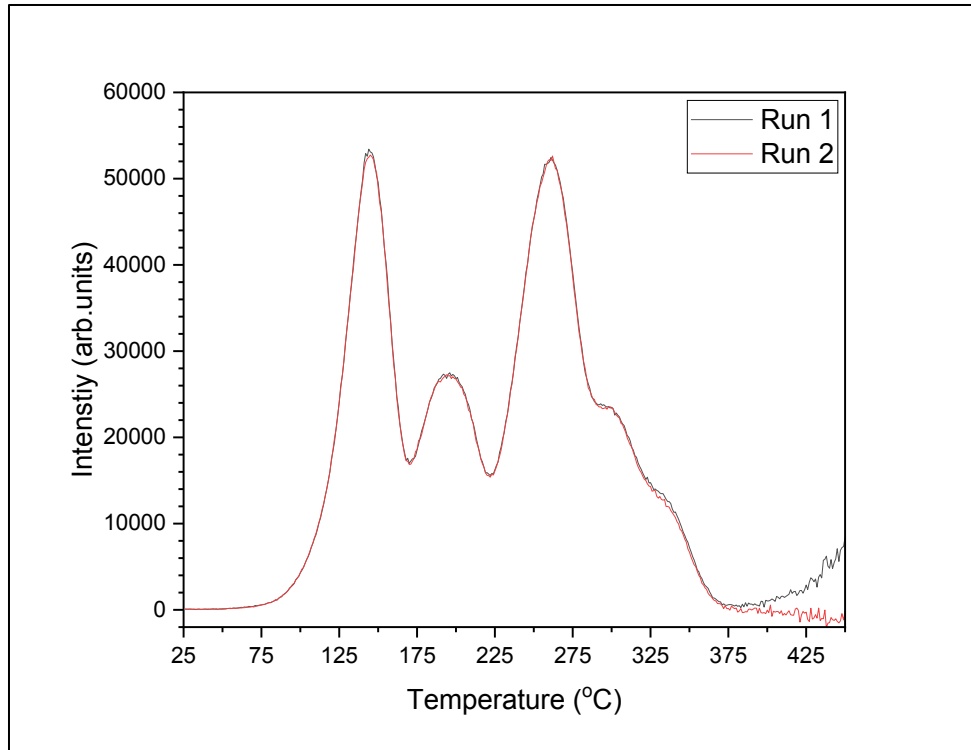


Figure 5.10: TL reproducibility measurements of pristine $Y_3Al_5O_{12}$.

The comparison of these TL glow curves reveals the absence of changes in the glow peaks. Therefore, no fading occurred and any possible electron traps at deeper energies do not influence the glow curves of $Y_3Al_5O_{12}$ within the timeframe of these measurements.

5.6 – Summary of Results

In summary, optical absorption and radioluminescence results showed clear effects of ion irradiation. TL and TL spectroscopy results were able to identify which defects and impurities serve as recombination centers of each of the main glow peaks.

CHAPTER SIX

ZINC OXIDE RESULTS AND DISCUSSION

6.1 – 2013 SRIM Calculations

6.1.1 – Calculated Range of Ions

Calculations of the projected longitudinal and latitudinal depth of irradiation ions in ZnO were executed with the 2013 SRIM code (*cf. Table 3.1*). 2013 SRIM Monte Carlo calculations of ion irradiation damage were also executed. In *Figure 6.1*, a total of 1000 ions were used to illustrate these calculations. 2013 SRIM assigns different colors to both the incident ion and the target elements in order to visually observe the effects of nuclear and electronic energy loss. For ZnO, the 2013 SRIM code color assignments for different target atoms that are moving and stopped can be found in *Table 6.1*.

Table 6.1: Differentiating moving and stopped ZnO atoms by color.

Target Atom	Zn	O
Color	moving	stopped
	orange	light blue
	green	dark blue

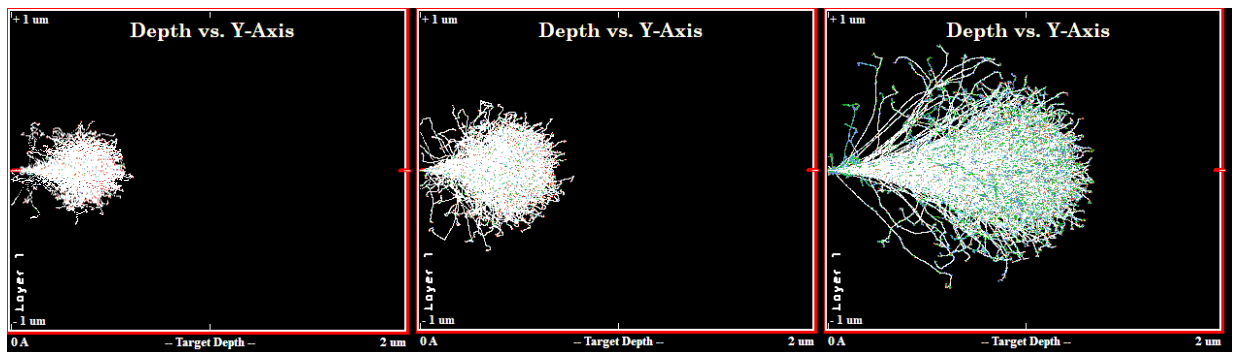


Figure 6.1: Ion trajectories in ZnO calculated using 2013 SRIM: H⁺ (left), He⁺ (middle), and O⁺ (right).

6.1.2 – Nuclear and Electronic Energy Loss

The 2013 SRIM code was used to calculate the nuclear, electronic, and total energy loss of the incident ions in ZnO. These results can be found in *Figure 6.2* below.

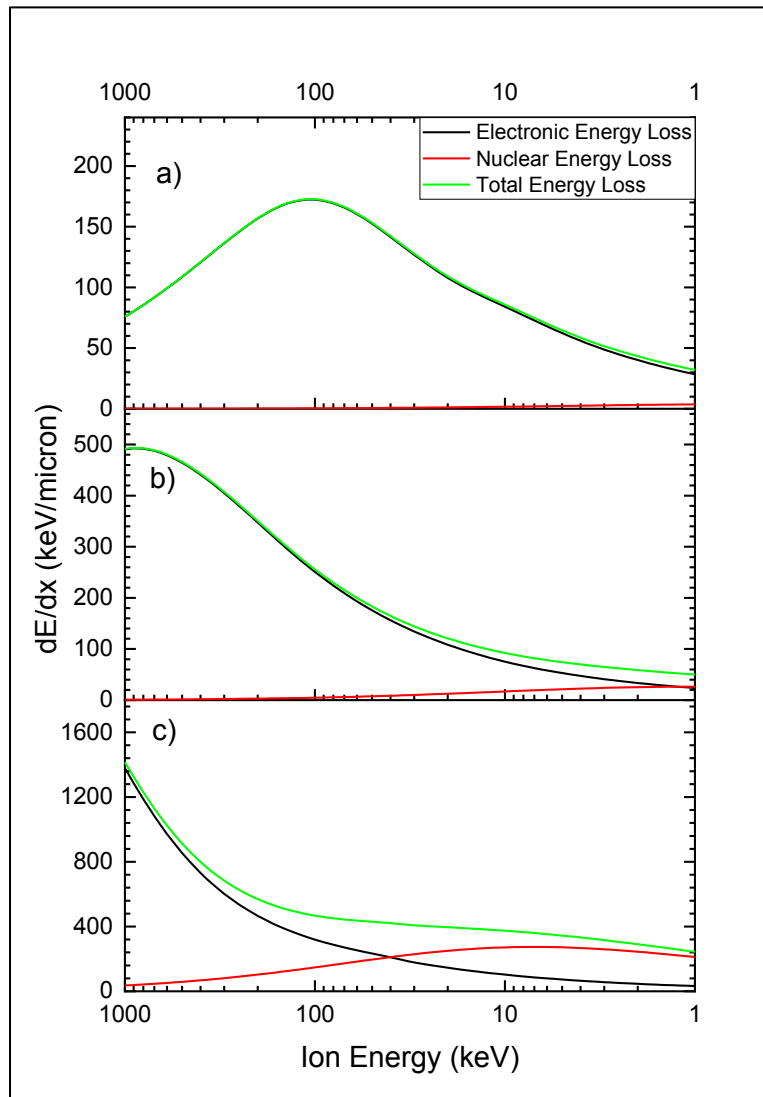


Figure 6.2: Electronic, nuclear, and total energy loss in ZnO for a) H^+ , b) He^+ , and c) O^+ ions.

From these results, it is apparent that O^+ ions in ZnO have the highest nuclear energy loss. For H^+ and He^+ , energy loss is dominated by the electronic energy loss for most of the energy

range, while for O^+ nuclear energy loss dominates below about 40 keV. Also, as previously mentioned in Chapter 1, nuclear collisions are responsible for the creation of defects in the target material. Therefore, these results explain the total dpa calculations for ZnO that list O^+ ions responsible for the most damage creation amongst all ions investigated (*cf. Table 3.3*).

6.1.3 – Damage Depth Distribution

The 2013 SRIM code was used to calculate damage depth distribution in terms of dpa for each target element of ZnO. These results can be found in *Figure 6.3*.

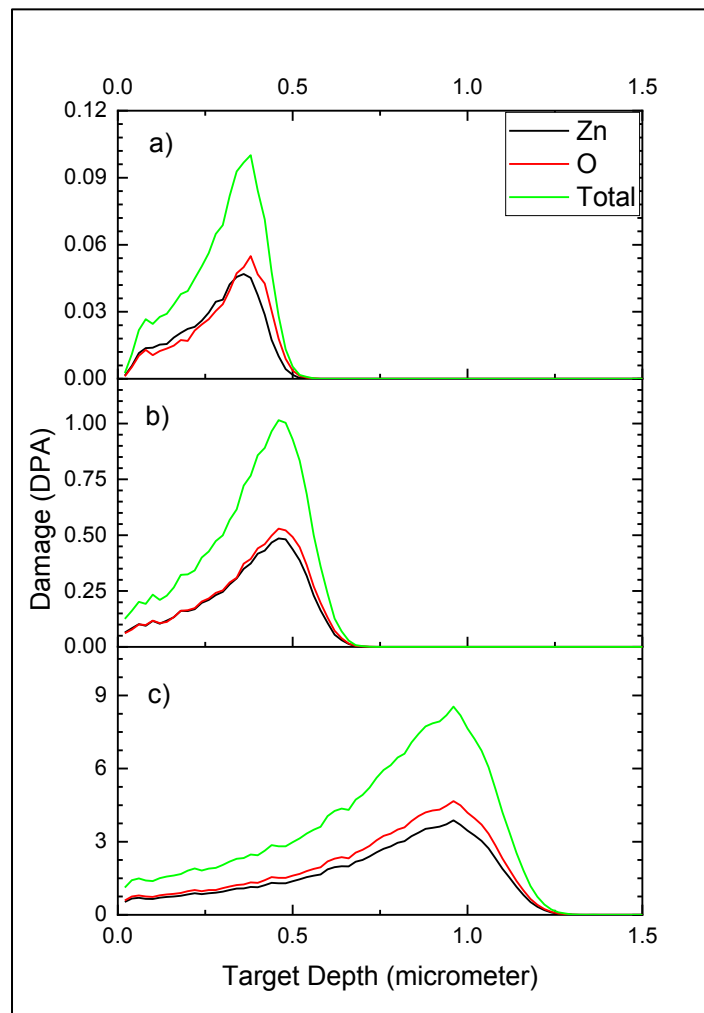


Figure 6.3: Damage depth distribution of a) H^+ , b) He^+ and c) O^+ ion irradiations in ZnO.

From these results, it is apparent that irradiation with O^+ ions leads to the furthest projected range in ZnO, which supports previous calculations (*cf. Table 3.1*). For all three ions, it can be observed that the creation of vacancies from displaced oxygen target atoms is the leading cause of damage in ZnO, with their percentages previously discussed in *Table 3.3*. However, Zn target atoms contribute almost equally to the vacancy formation from O target atoms in all irradiated samples.

6.2 – Raman Spectroscopy

Raman spectroscopy measurements were obtained in order to evaluate the effects of ion radiation on the structure of ZnO. The results of these measurements can be found in *Figure 6.4*.

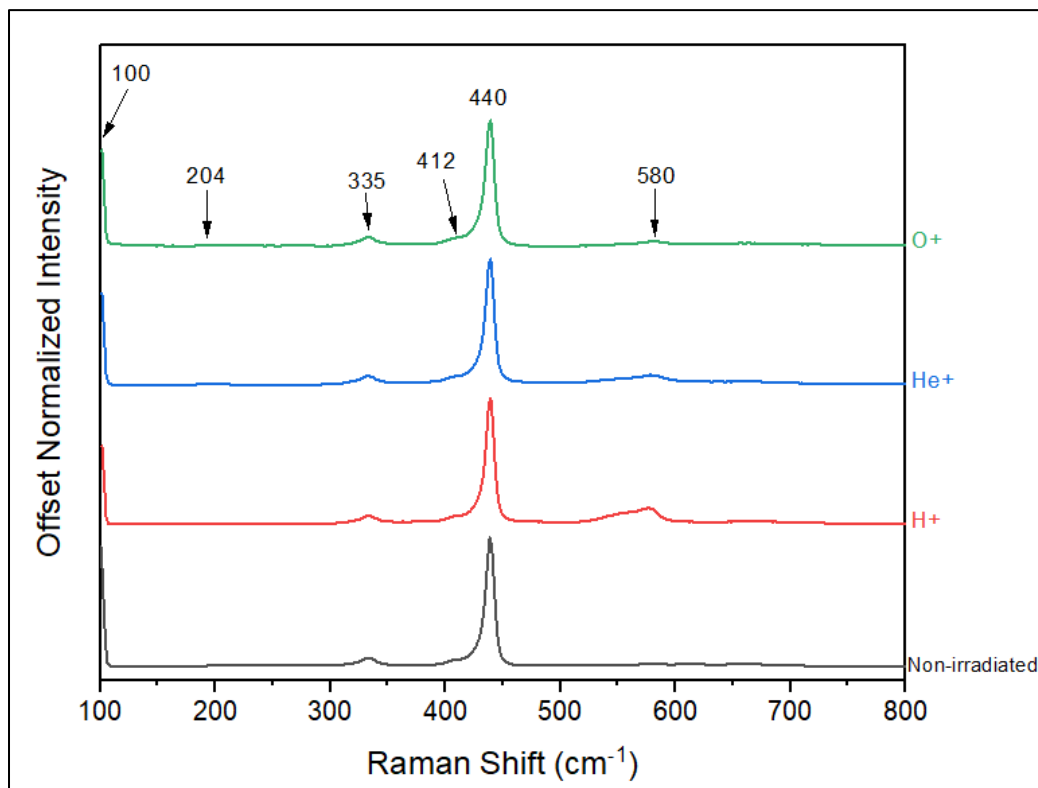


Figure 6.4: Raman spectra of pristine and irradiated ZnO samples offset by intensity.

From the Raman spectroscopy measurements, the presence of six peaks was observed in each sample. The six observed peaks were compared with previous literature to determine the identity of the vibrational modes that were measured and are presented in *Table 6.2*.¹⁻⁴

Table 6.2: Detected vibrations from Raman in all ZnO samples.¹⁻⁴
LO and TO are longitudinal optical and transverse optical, respectively.

Shift Position (cm ⁻¹)					Vibrations
This Work	Ref [1]	Ref [2]	Ref [3]	Ref [4]	
100	101	101	101	99	Zn sublattice
204	---	208	---	203	TO phonons, 2 nd order transitions
---	---	---	---	284	TO phonons
335	---	332	---	333	Zn and O sublattice
---	380	380	380	378	TO phonons
---	---	---	395/398	---	Quasi – TO phonons
412	407	408	413	410	LO phonons
440	437	437	444	438	O sublattice
---	---	---	---	483	TO phonons
577	574	574	579	574	TO phonons
---	583	584	585	---	Quasi - LO phonons
---	---	---	591	590	LO phonons

Previous studies on the vibrational modes in wurtzite ZnO have discovered that the peak at 100 cm⁻¹ is influenced by Zn²⁺ vacancies in the structure and the peak at 440 cm⁻¹ is influenced by O²⁻ vacancies.⁵ The very weak peak at ~580 cm⁻¹ has been associated with oxygen deficiencies and disorder in the ZnO lattice.^{5,6} Due to instrumental limitations of this work, the peak at 100 cm⁻¹ could not be analyzed for Zn²⁺ vacancy created, therefore, analysis was focused on the 440 cm⁻¹

peak. Raman spectra of all ZnO samples were normalized to the peak at 440 cm^{-1} in order to determine its possible shift in peak position and changes in its peak FWHM (Figure 6.5). Changes in the peak position after being corrected by the neon lamp reference can be found in Table 6.3.

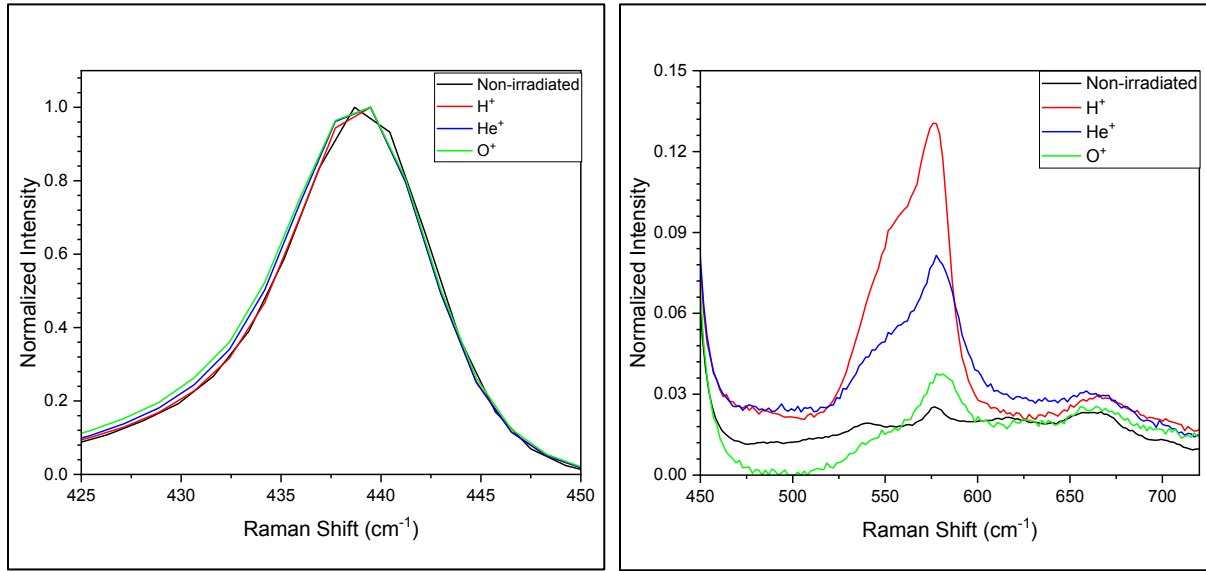


Figure 6.5: Overlay of selected Raman bands of pristine and irradiated ZnO Raman spectra after position correction and normalization at 440 cm^{-1} .

Table 6.3: Changes in peak position and FWHM for ZnO Raman spectra.

Sample	Peak Position	Peak FWHM
Non-irradiated	439.6	8.9
H ⁺	438.7	8.8
He ⁺	438.6	8.9
O ⁺	438.6	9.1

Analysis of the shifts in peak location due to ion irradiation of the ZnO samples revealed that the greatest shift was $\sim 1.0\text{ cm}^{-1}$ between the pristine sample and the He⁺ and O⁺ irradiated samples. While it is possible that some peak shift may have happened in ZnO due to ion irradiation, this variation is at the upper limit of the experimental uncertainty and thus the magnitude of the

strain caused by ion irradiation is expected to be low. Changes in the peak FWHM revealed a maximum change of $\sim 0.2 \text{ cm}^{-1}$ between the pristine and O^+ irradiated samples and thus no significant structural disorder was created.

After normalization to the 440 cm^{-1} peak, an increase in relative intensity for the peak and shoulder band can be seen around 550 cm^{-1} . Previous work has reported this increase in relative intensity from As^+ -implanted ZnO and attributed it to the appearance of a Raman forbidden mode due to the loss of long range order and symmetry breakdown in the ZnO coordination shell.⁷ Our Raman results showed an increase in relative intensity of these bands when compared with the non-irradiated sample, in agreement with the previous report. However, it was not possible to directly correlate these results with dpa suggesting that chemical effects related to the nature of the ion may play a relevant role.

6.3 – UV-Visible Optical Spectroscopy

UV-visible optical spectroscopy measurements were conducted in order to determine the effects of ion irradiation on the creation and intensity of absorbance bands in ZnO and on the general transmittance of light. The results of these measurements can be found in *Figure 6.6*.

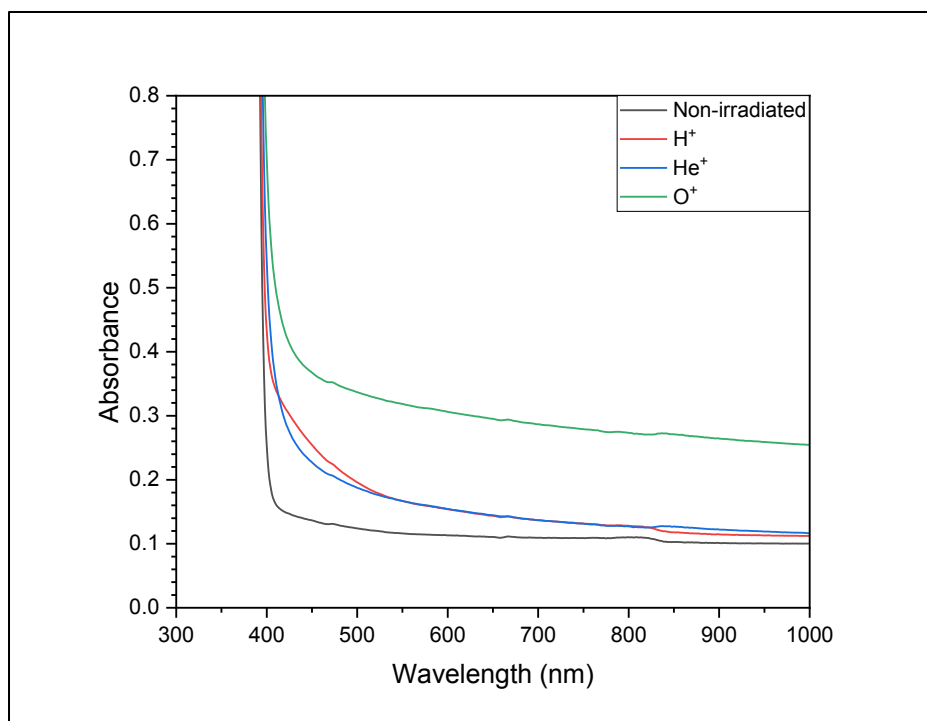


Figure 6.6: Optical absorption spectra of pristine and irradiated ZnO samples.

From these results, there is no clear evidence for the creation of an absorbance band due to ion irradiation. An overall increase in the baseline absorption (loss of optical transparency) can be seen in all irradiated samples when compared to pristine ZnO. This shift in absorption and its enhancement for lower wavelengths can be explained by an increase in Rayleigh scattering due to the creation of point defects as previously discussed in Chapter 4. While an overall increase of absorption for increasing dpa determined from 2013 SRIM calculations (*Table 3.3*) further supports this result, the similarity between of the absorption results for H⁺ and He⁺ suggests chemical effects to play an important role.

6.4 – Radioluminescence

RL measurements were conducted to determine the identity and possible change of relative intensities of luminescence bands (and thus of the concentrations of luminescence centers) due to ion irradiation of ZnO. These measurements can be found in *Figure 6.7*.

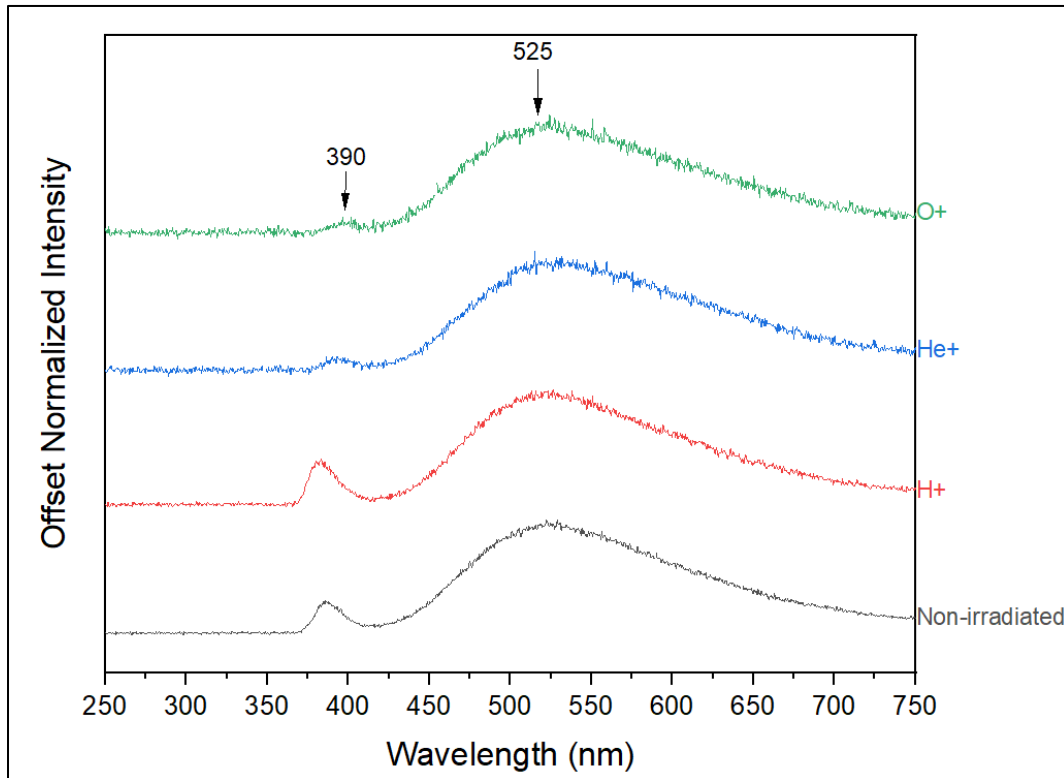


Figure 6.7: Offset RL spectra of pristine and irradiated ZnO samples.

From these results, two distinct luminescence bands were observed including a broad-band centered at ~525 nm and a narrower band at ~390 nm. The 390 nm band has an excitonic nature, while the nature of the 525 nm band is still not fully understood. It has been attributed to Cu^{2+} impurities, Zn vacancies, O vacancies, Zn interstitials, Zn_O anti-sites, and electronic transitions between a shallow donor to a deep acceptor, likely a Zn vacancy.⁸ Since the optical transparency of the samples changed due to ion irradiation, the absolute RL intensity of the bands cannot be

compared. Consequently, the relative intensity of the peaks was compared to investigate possible changes due to ion irradiation. These results can be found in *Table 6.4*.

Table 6.4: Intensity ratio of RL peaks in pristine and irradiated ZnO samples.

Sample	Peak Ratio (390 nm/525 nm)
Non-irradiated	0.29
H ⁺	0.38
He ⁺	0.13
O ⁺	0.13

Visual inspection of *Figure 6.7* and the results summarized in *Table 6.4* reveal that the intensity of the 390 nm band strongly decreases in relation to the 525 nm band for both the He⁺ and O⁺ irradiations of ZnO. An exciton, that corresponds to an electrostatically bonded electron (in the conduction band)-hole (in the valance band) pair, is known to be fragile. In ZnO, its binding energy is only 0.06 eV⁸ that is relatively close to room temperature thermal energy 0.025 eV. The presence of defects is known to facilitate the non-radiative recombination of excitons explaining the relative decrease of the intensity of the 390 nm band for the irradiated samples with the highest dpa (*cf. Figure 6.3*). Some authors⁴ proposed that hydrogen could react with defects, $[V_{Zn}]^{2-} + H_2 \rightarrow 2[Hzn]^-$, creating new defects and thus affecting the luminescent properties of ZnO.^{9,10} This may be the reason for the increase of the luminescence intensity ratio shown in *Table 6.4*. This result is supportive of the interpretation that chemical effects play a relevant role in H⁺ irradiation of ZnO. Further work is necessary to confirm this hypothesis.

6.5 – Thermoluminescence

TL measurements were conducted to investigate how traps were affected by ion irradiation.

The results of these measurements can be found in *Figure 6.8* below.

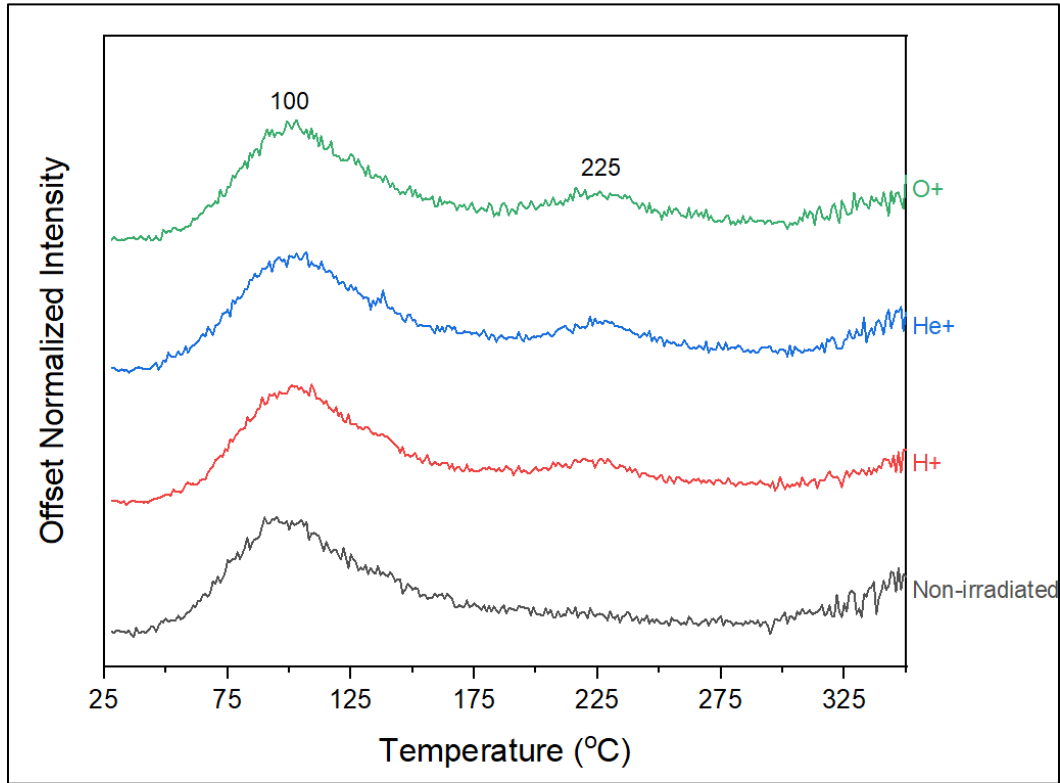


Figure 6.8: Glow curves of the pristine and irradiated ZnO samples.

From the glow curves, two luminescence peaks were observed at 100 and 225 °C in all samples. Visual analysis of the glow curves led to the observation of a change in relative peak intensity due to ion irradiation. Therefore, this relative change in peak intensity from ion irradiation was analyzed and can be in *Table 6.4*.

Table 6.4: Intensity ratio of TL peaks for ZnO samples.

Sample	Non-irradiated	H ⁺	He ⁺	O ⁺
Ratio (225 °C/100 °C)	0.19	0.35	0.42	0.39

These results show that ion irradiation of ZnO crystals resulted in an increase of relative peak intensity for the 225 °C luminescence center, with the relative intensity of the 225 °C glow peak overall increasing with dpa.

TL spectroscopy measurements were conducted to determine the identity of the recombination centers leading to the two distinct peaks seen in the TL measurements (*Figure 6.8*).

The results of these measurements can be found in *Figure 6.9*.

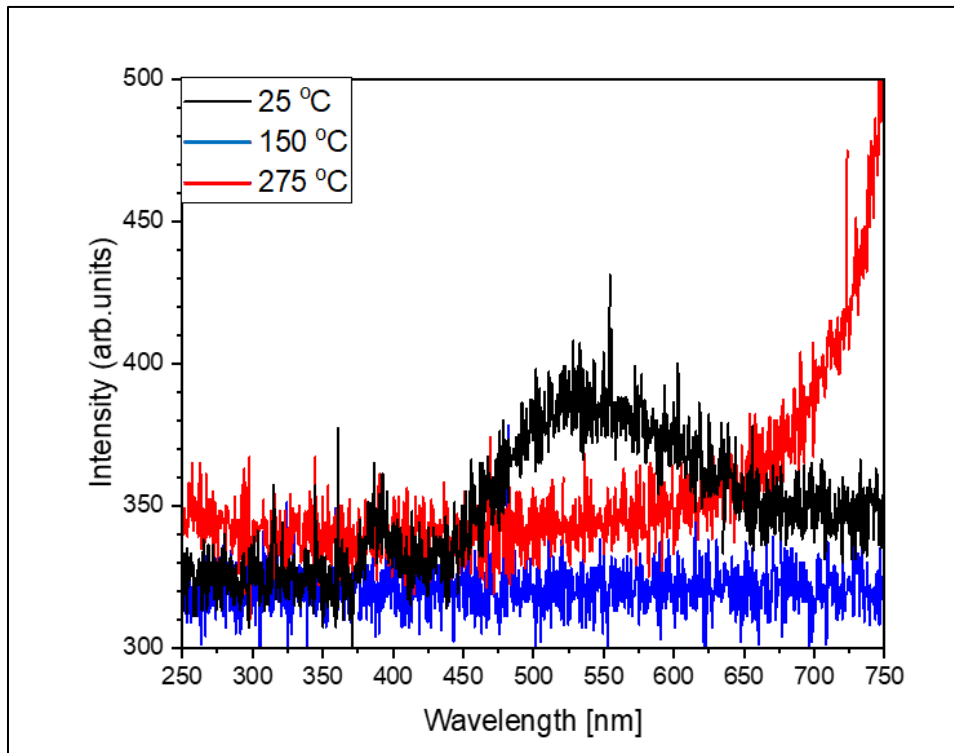


Figure 6.9: TL spectroscopy results of pristine ZnO. The increase in intensity of the 275-400 °C spectrum corresponds to the contribution of the blackbody radiation of the system.

These results show that two luminescence centers, a weak peak around 400 nm and a broad-band peak centered around 550 nm, contribute within 25-150 °C, *i.e.*, they correspond to the recombination process of the TL main glow peak in pristine ZnO glow (*Figure 6.9*). The second glow peak at 225 °C had a lower intensity and thus no emission was detected.

TL reproducibility measurements were conducted to determine the possibility of electron traps existing at deeper energies in the sample seeping electrons to lower energy traps and thus changing the TL glow curves in time. The results of this measurement can be found in *Figure 6.10*.

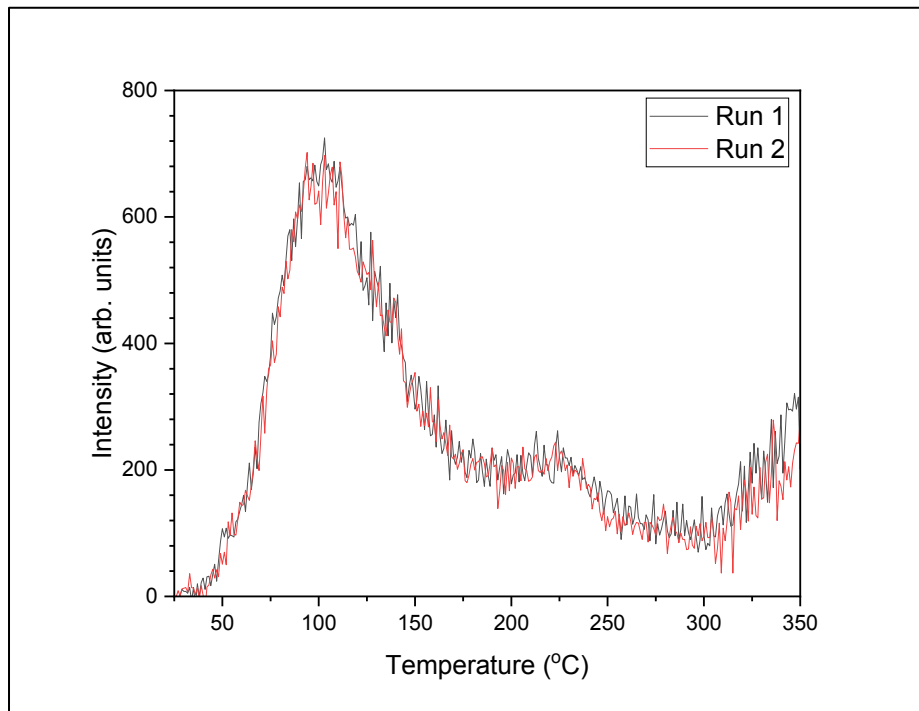


Figure 6.10: TL reproducibility measurements of pristine ZnO.

The comparison of these TL glow curves reveals the absence of changes in the glow curves. Therefore, any possible electron traps at deeper energies do not influence the glow curves of ZnO. However, the relative intensity of the two glow peaks changed when compared to *Figure 6.8*. Thus,

the TL response of ZnO showed indication for having sensitivity to its irradiation history and of limited use for the desired radiation damage analysis.

6.6 – Summary of Results

In summary, Raman spectroscopy, optical absorption, radioluminescence, and thermoluminescence measurements all showed clear effects of ion irradiation in ZnO. Results suggest that chemical effects related to the irradiation with H^+ may play a relevant role in the optical functionalities of this material.

CHAPTER SEVEN

YTTRIUM VANADATE RESULTS AND DISCUSSION

7.1 – 2013 SRIM Calculations

7.1.1 – Calculated Range of Ions

Calculations of the projected longitudinal and latitudinal depth of irradiation ions in YVO_4 were executed with the 2013 SRIM code (*cf. Table 3.1*). 2013 SRIM Monte Carlo calculations of ion irradiation damage were also executed. In *Figure 7.1*, a total of 1000 ions were used to illustrate these calculations. 2013 SRIM assigns different colors to both the incident ion and the target elements in order to visually observe the effects of nuclear and electronic energy loss. For YVO_4 , the 2013 SRIM code color assignments for different target atoms that are moving and stopped can be found in *Table 7.1*.

Table 7.1: Differentiating moving and stopped YVO_4 atoms by color.

Target Atom		Y	V	O
Color	moving	orange	light blue	pink
	stopped	green	dark blue	purple

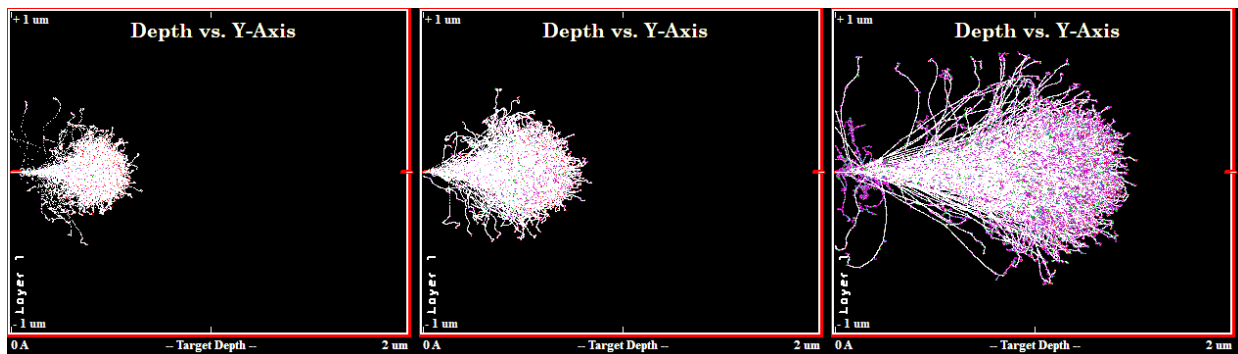


Figure 7.1: Ion trajectories in YVO_4 calculated using 2013 SRIM: H^+ (left), He^+ (middle), and O^+ (right).

7.1.2 – Nuclear and Electronic Energy Loss

The 2013 SRIM code was used to calculate the nuclear, electronic, and total energy loss of the incident ions in YVO_4 . These results can be found in *Figure 7.2* below.

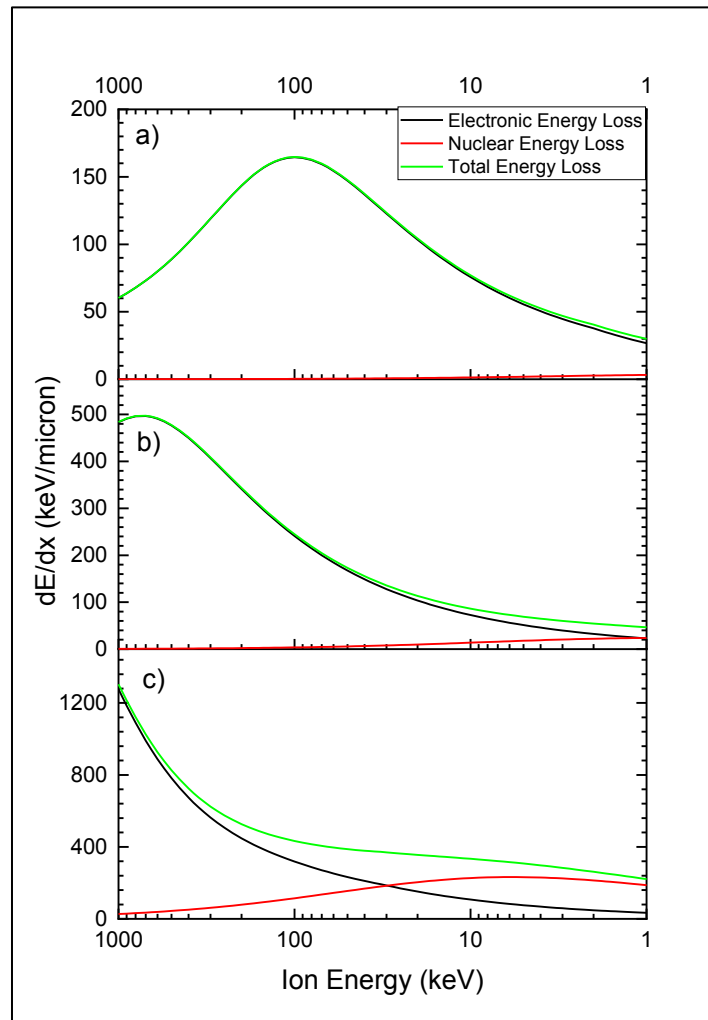


Figure 7.2: Electronic, nuclear, and total energy loss in YVO_4 for a) H^+ , b) He^+ , and c) O^+ ions.

From these results, it is apparent that O^+ ions in YVO_4 have the highest nuclear energy loss. For H^+ and He^+ , energy loss is dominated by the electronic energy loss for most of the energy range, while for O^+ nuclear energy loss dominates below about 30 keV. Also, as previously

mentioned in Chapter 1, nuclear collisions are responsible for the creation of defects in the target material. Therefore, these results explain the total dpa calculations for YVO_4 that list O^+ ions responsible for the most damage creation amongst all ions investigated (*cf. Table 3.3*).

7.1.3 – Damage Depth Distribution

The 2013 SRIM code was used to calculate damage depth distribution in terms of dpa for each target element of YVO_4 . These results can be found in *Figure 7.3*.

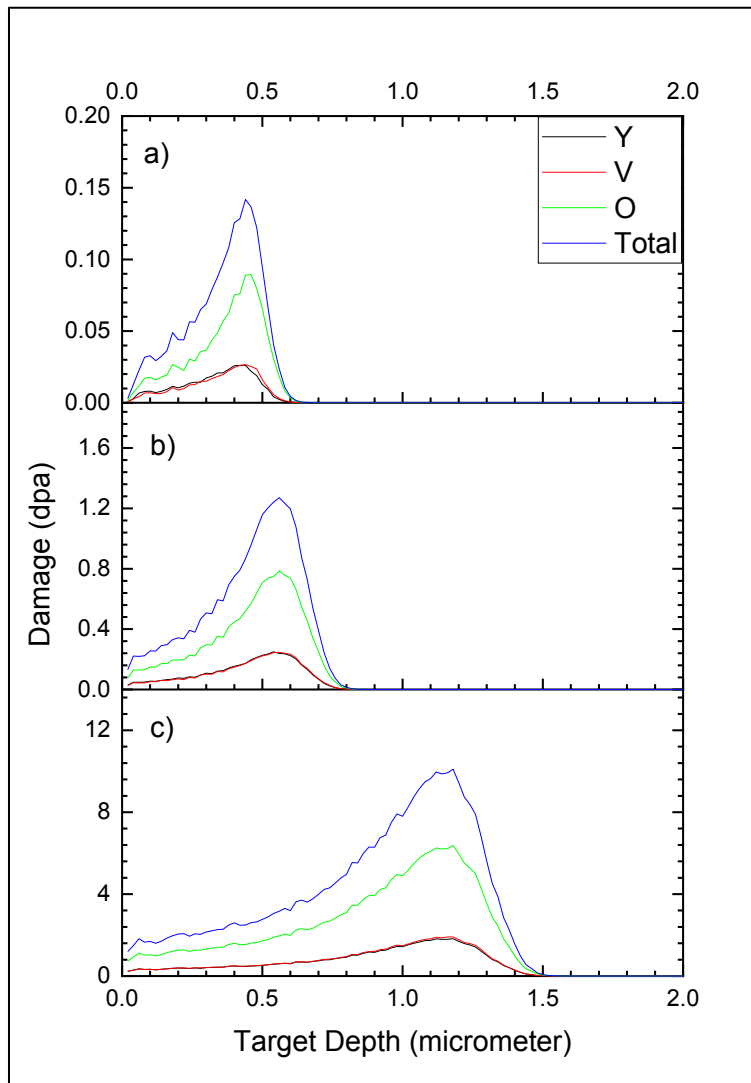


Figure 7.3: Damage depth distribution of a) H^+ , b) He^+ and c) O^+ ions in YVO_4 .

From these results, it is apparent that irradiation with O^+ ions leads to the furthest projected range in YVO_4 , which supports previous calculations (*cf. Table 3.1*). For all three ions, it can be observed that the creation of vacancies from displaced oxygen target atoms is the leading cause of damage in YVO_4 , with their percentages previously discussed in *Table 3.3*.

7.2 – Raman Spectroscopy

Raman spectroscopy measurements were obtained in order to evaluate the effects of ion radiation on the structure of YVO_4 . The results of these measurements can be found in *Figure 7.4*.

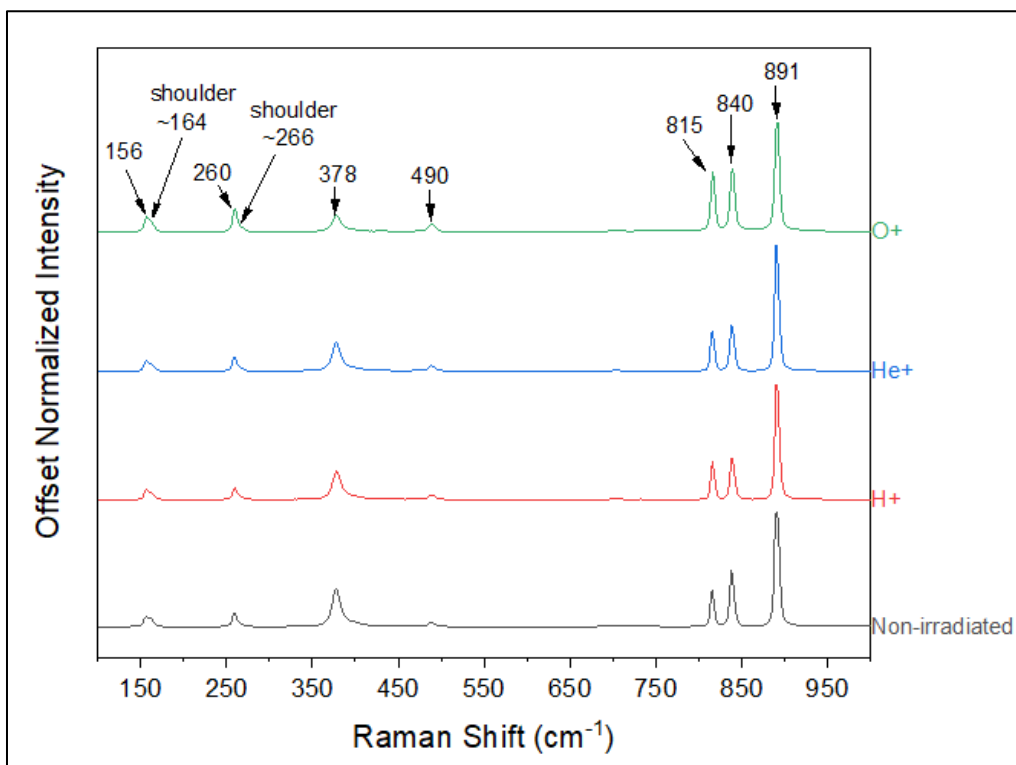


Figure 7.4: Raman spectra of pristine and irradiated YVO_4 samples offset by intensity.

Raman spectroscopy measurements revealed the presence of seven peaks in all samples in addition to two weaker peaks that are observed as shoulders of the peaks at ~ 164 and ~ 266 cm^{-1} , respectively. These peaks were compared with previous literature to determine the identity of the vibrational modes that were measured. The summary of this analysis can be found in *Table 7.2*.¹⁻⁴

Table 7.2: Detected vibrational modes from Raman in all YVO_4 samples.¹⁻⁴
External corresponds to YVO_4 . Internal corresponds to anion $[\text{VO}_4]^{3-}$.

Shift Position (cm^{-1})					Vibrations
This work	Ref [1]	Ref [2]	Ref [3]	Ref [4]	
---	---	---	137	---	Internal vibrations
156	154	156	156/157	156.8	External translation
164	161	162	163/164	163.2	External translation
260	260	259/260	260	259.6	External translation/internal vibrations
266	---	---	265/267	---	External vibrations
378	375	377	378	378.4	External vibrations
---	---	---	444	---	External translations
490	487	487	490	489.3	Internal vibrations
815	816	816	817	816	Internal vibrations
840	840	838	839/840	838.8	Internal vibrations
891	889	891	891	891.1	Internal vibrations

The presence of two additional peaks at 444 cm^{-1} and 137 cm^{-1} , corresponding to $E_g(\text{IV})$ internal vibrations and external translations respectively, have been identified in YVO_4 before.³ However, these two vibration modes were not detected in every measurement reported in the literature and were not detected in our measurements either. Raman spectra for all YVO_4 samples were normalized to the peak of greatest intensity (891 cm^{-1}), after correction by the neon lamp

reference, in order to determine possible shifts in peak position and changes in the peak FWHM. The results of this analysis can be found in *Figure 7.5* and *Table 7.3*.

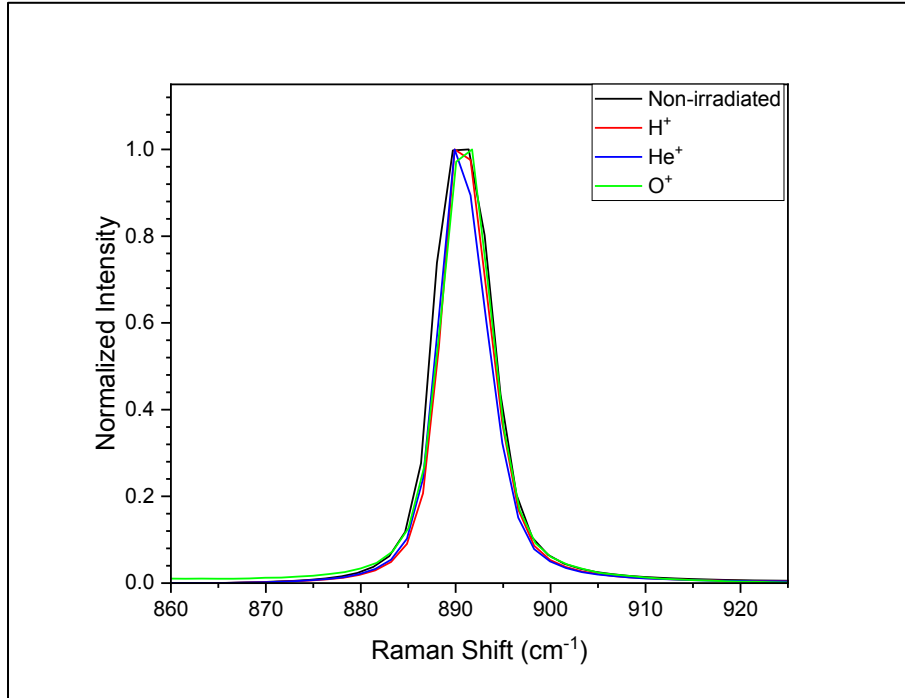


Figure 7.5: Overlay of pristine and irradiated YVO₄ Raman spectra after normalization and position correction.

Table 7.3: Changes in peak position and FWHM for YVO₄ Raman spectra.

Sample	Peak Location (cm ⁻¹)	Peak FWHM (cm ⁻¹)
Non-irradiated	890.5	7.3
H ⁺	890.7	6.2
He ⁺	890.6	6.2
O ⁺	890.8	6.5

Analysis of the shifts in peak location due to ion irradiation of the YVO₄ samples revealed that the greatest shift was ~0.3 cm⁻¹ between the pristine sample and the O⁺ irradiated sample (*Table 7.3*). The analysis of the peak broadening due to ion irradiation revealed a minor decrease

in the FWHM of the peaks of the irradiated samples compared to the non-irradiated sample (*Table 7.3*). The observed peak shift and the changes of peak FWHM were determined to be within experimental uncertainty under the experimental conditions. Therefore, ion irradiation induced minimal strain, if any, in the structure of YVO_4 .

7.3 – UV-Visible Optical Spectroscopy

UV-visible optical spectroscopy measurements were conducted in order to determine the effect of ion irradiation on the creation and intensity of the absorbance bands in YVO_4 and general transmittance of light. The results of these measurements can be found in *Figure 7.6*.

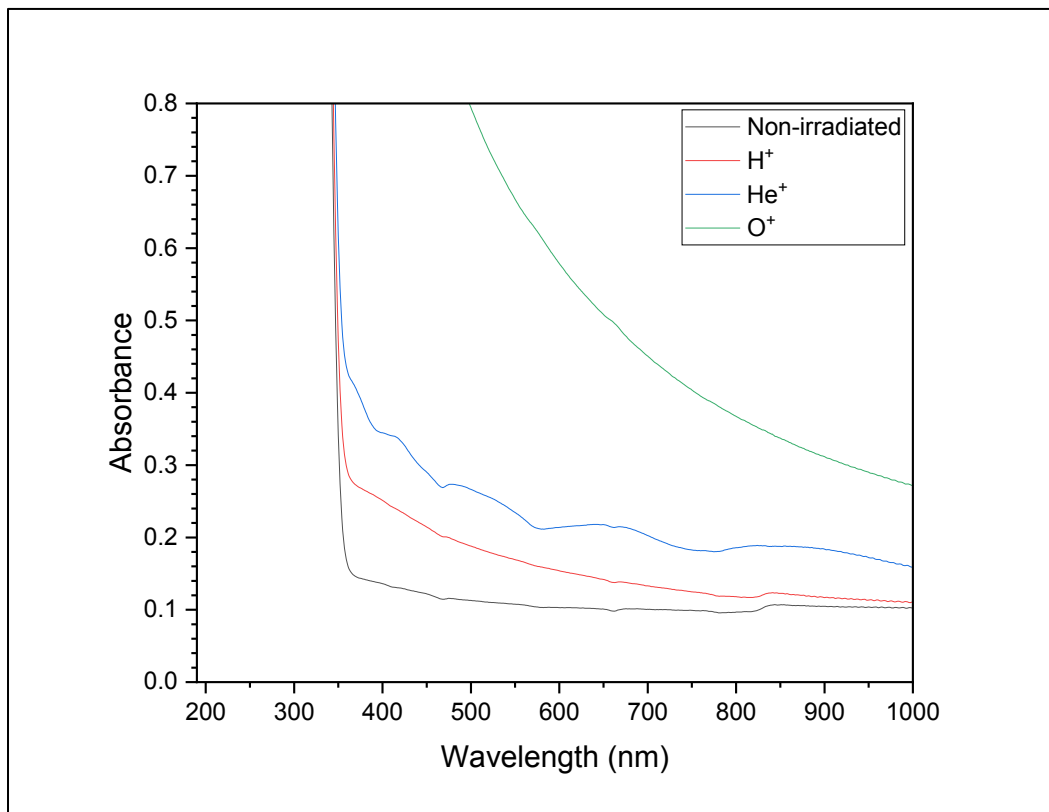


Figure 7.6: Optical absorption spectra of pristine and irradiated YVO_4 samples.

From these results, no clear absorption bands can be identified in the pristine YVO₄ or in the irradiated samples. The oscillating pattern seen in the He⁺ irradiated YVO₄ has been attributed to light interference and should be disregarded. A clear absorption edge for the non-irradiated, H⁺, and He⁺ YVO₄ samples was observed at ~334 nm in agreement with previous literature reporting the absorption edge between 330 – 340 nm for YVO₄ crystals.⁵

An overall increase in the baseline absorption can be seen in all irradiated samples when compared to pristine YVO₄. This shift in absorption and its enhancement for lower wavelengths can be explained by an increase in Rayleigh scattering due to the creation of point defects from irradiation as it was previously discussed in Chapter 4. From the results, it is apparent that the number of scattering centers is highest in the O⁺ irradiated sample, with He⁺ following and H⁺ last. This trend is supported by the trend of increasing dpa for H⁺, He⁺, and O⁺ ions as previously discussed in Chapter 3 (*cf. Table 3.3*).

7.4 – Radioluminescence

RL measurements were conducted to determine the identity and possible change of relative intensities of luminescence bands (and thus of the concentrations of luminescence centers) due to ion irradiation of YVO₄. These measurements can be found in *Figure 7.7*.

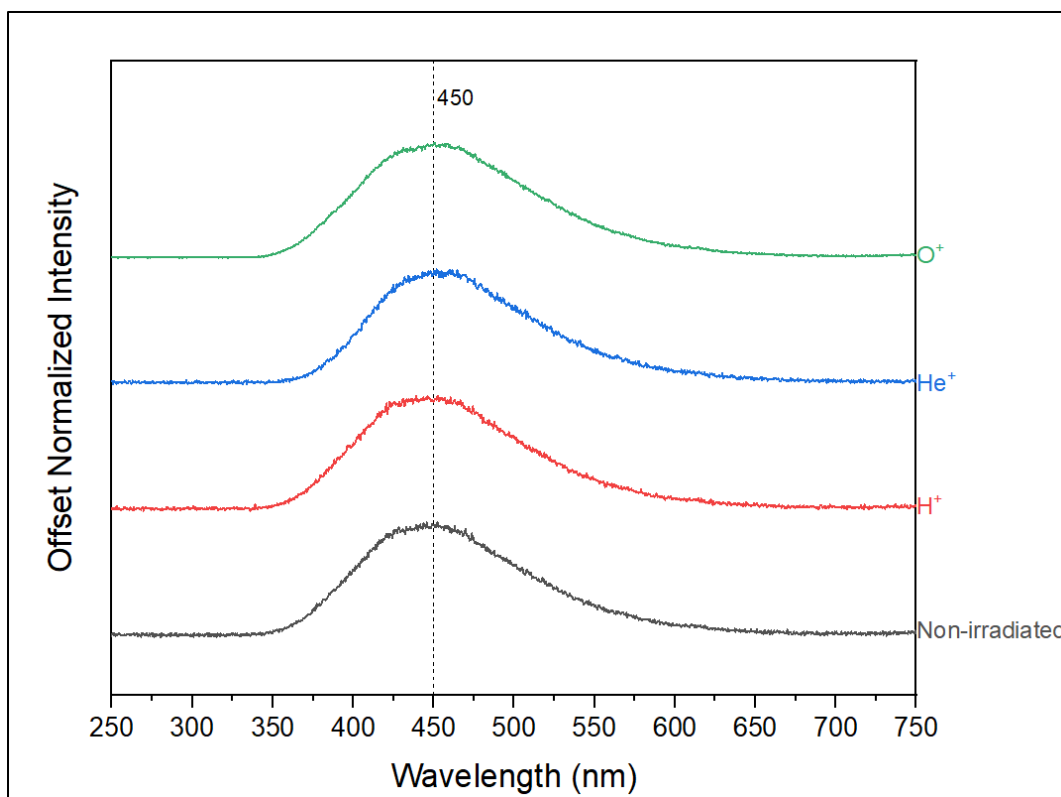


Figure 7.7: Offset RL spectra of pristine and irradiated YVO₄ samples.

From these results, only one broad luminescence band was detected and centered at ~450 nm for all samples. This band has been previously experimentally measured and attributed to an electronic transition within the molecular complex [VO₄]³⁻.⁶ Inspection of the RL spectra does not show a shift in the RL peak location due to ion irradiation. Since the optical transparency of the samples changed due to ion irradiation, the absolute RL intensity of the bands cannot be compared. Consequently, since there are no other luminescence bands to serve as a reference, no definitive conclusions can be made about the effect of ion irradiation on YVO₄ luminescence through RL measurements.

7.5 – Thermoluminescence

TL measurements were conducted to investigate how traps were affected by ion irradiation.

The results of these measurements can be found in *Figure 7.8* below.

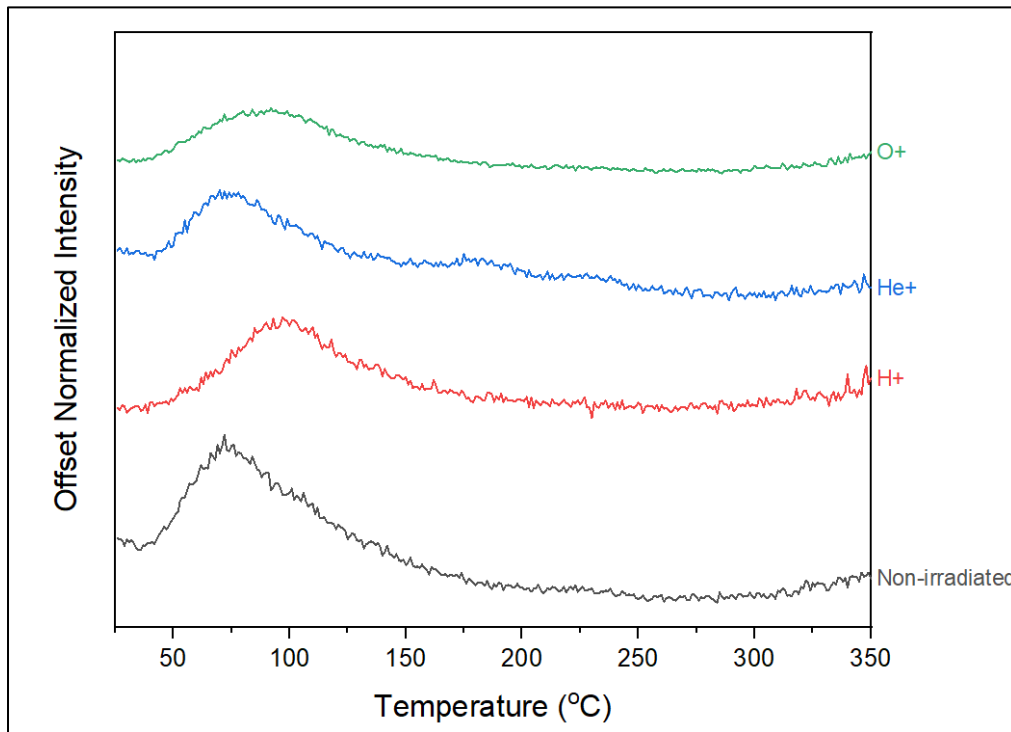


Figure 7.8: Glow curves of pristine and irradiated YVO₄ samples.

The glow curves were all somewhat different from that of the pristine crystal. The TL glow peak of the H⁺ and O⁺ irradiated crystals were shifted to higher temperatures, and the TL glow curve of the He⁺ irradiated crystal presented two additional glow peaks within 150-250 °C but no shift of the main TL glow peak. These results suggest the chemical nature of the ion plays a role in affecting the traps, but the analysis of these complex effects goes beyond the proposed goals of this work.

TL spectroscopy measurements were conducted to determine the identity of the recombination centers related to the glow peaks observed in the glow curves (*Figure 7.8*). The results of these measurements can be found in *Figure 7.9*.

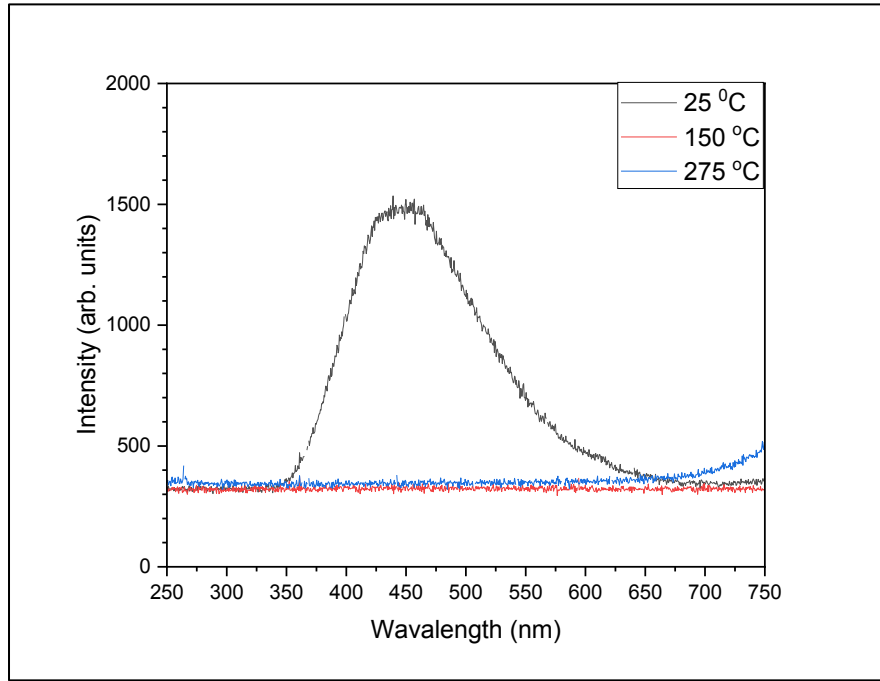


Figure 7.9: TL spectroscopy results of pristine YVO₄.

From TL spectroscopy measurements, emission was observed only up to 150 °C in agreement with the TL glow curve of the non-irradiated crystal where no emission was observed above this temperature. Emission corresponded the same band previously observed in the RL measurements (*cf. Figure 7.7*). The emission of the higher temperature glow peaks were not able to be detected.

TL reproducibility measurements were conducted to determine the possibility of electron traps existing at deeper energies in the pristine YVO₄ sample affecting the glow curves. The results of this measurement can be found in *Figure 7.10*.

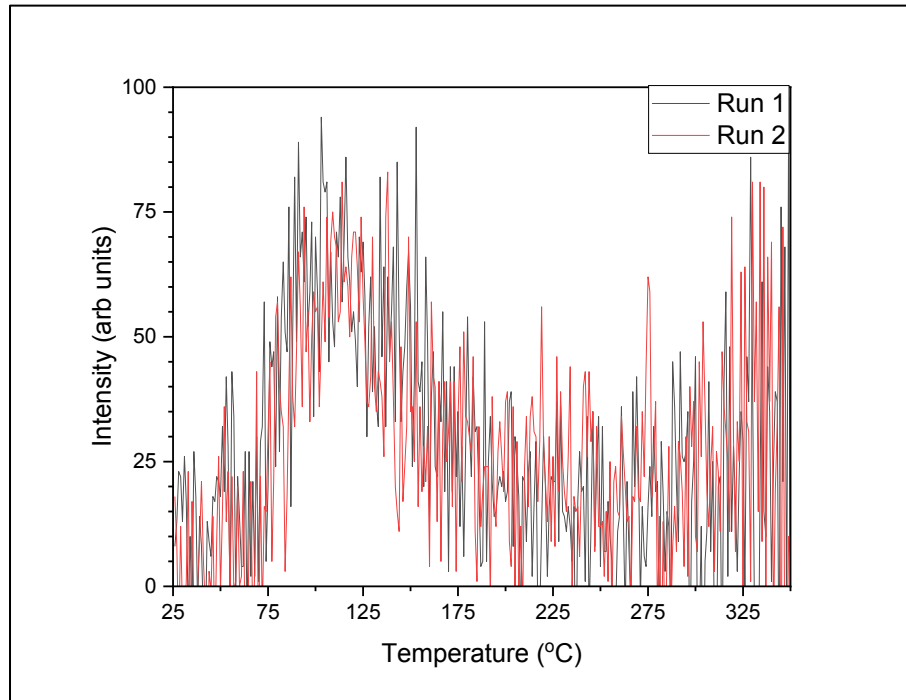


Figure 7.10: TL reproducibility measurements of pristine YVO₄.

The comparison of these TL glow curves reveals the absence of changes in the glow peaks, albeit, at considerably lower signal-to-noise ratios. However, both glow peaks were observed shifted to higher temperatures than in the glow curve reported in *Figure 7.8*. Therefore, the TL response of YVO₄ showed indication for having sensitivity to its irradiation history and thus of limited use for the desired radiation damage analysis.

7.6 – Summary of Results

In summary, optical absorption and TL results showed clear effects of ion irradiation, and perhaps chemical effects related to the nature of the irradiating ion. However, all the techniques used for this investigation revealed themselves of limited use in the quantification of the radiation damage suffered by YVO₄.

CHAPTER EIGHT

LITHIUM NIOBATE RESULTS AND DISCUSSION

8.1 – 2013 SRIM Calculations

8.1.1 – Calculated Range of Ions

Calculations of the projected longitudinal and latitudinal depth of irradiation ions in LiNbO₃ were executed with the 2013 SRIM code (*cf. Table 3.1*). 2013 SRIM Monte Carlo calculations of ion irradiation damage were also executed. In *Figure 8.1*, a total of 1000 ions were used to illustrate these calculations. 2013 SRIM assigns different colors to both the incident ion and the target elements in order to visually observe the effects of nuclear and electronic energy loss. For LiNbO₃, the 2013 SRIM code color assignments for different target atoms that are moving and stopped can be found in *Table 8.1*.

Table 8.1: Differentiating moving and stopped LiNbO₃ atoms by color.

Target Atom	Li	Nb	O
Color moving	orange	light blue	pink
Color stopped	green	dark blue	purple

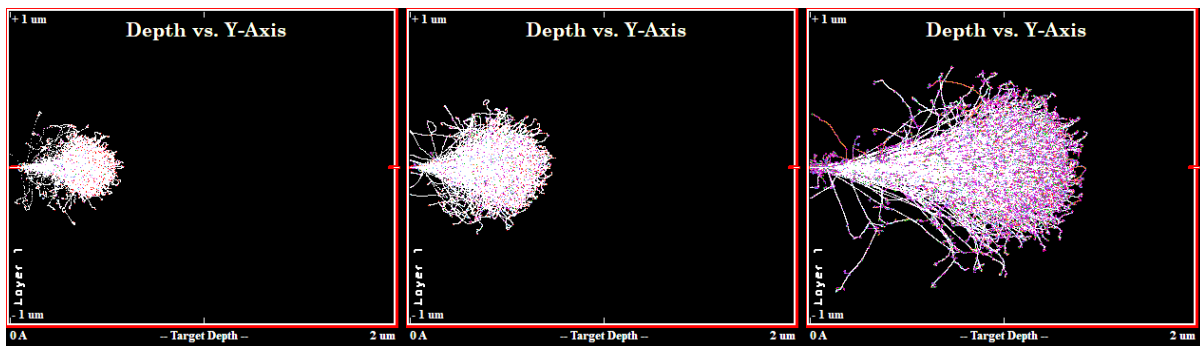


Figure 8.1: Ion trajectories in LiNbO₃ calculated using 2013 SRIM: H⁺ (left), He⁺ (middle), and O⁺ (right).

8.1.2 – Nuclear and Electronic Energy Loss

The 2013 SRIM code was used to calculate the nuclear, electronic, and total energy loss of the incident ions in LiNbO_3 . These results can be found in *Figure 8.2* below.

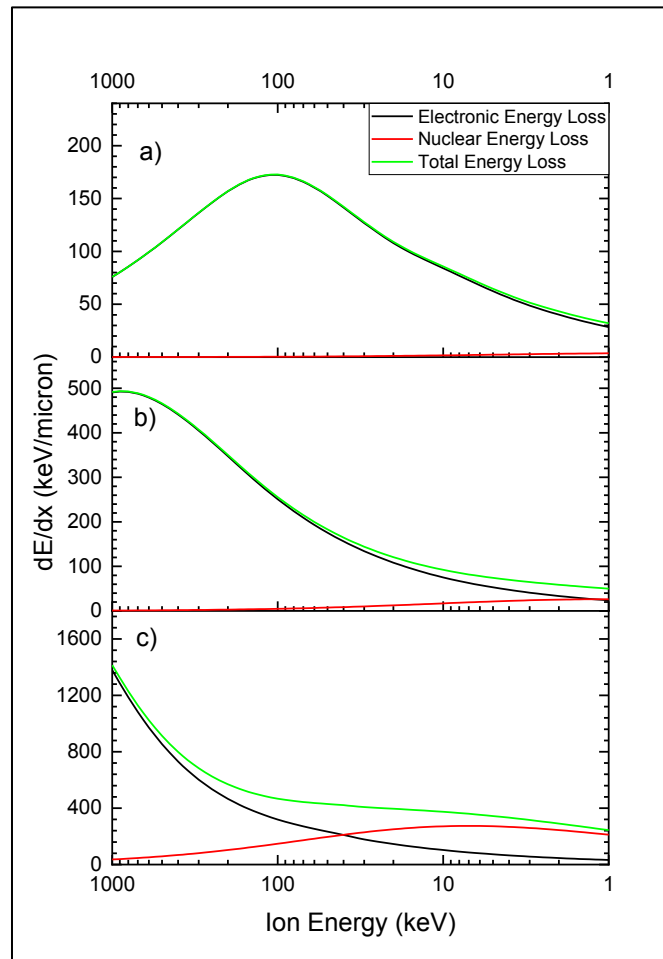


Figure 8.2: Electronic, nuclear, and total energy loss in LiNbO_3 for a) H^+ , b) He^+ , and c) O^+ ions.

From these results, it is apparent that O^+ ions in LiNbO_3 have the highest nuclear energy loss. For H^+ and He^+ , energy loss is dominated by the electronic energy loss for most of the energy range, while for O^+ nuclear energy loss dominates below about 40 keV. Also, as previously mentioned in Chapter 1, nuclear collisions are responsible for the creation of defects in the target

material. Therefore, these results explain the total dpa calculations for LiNbO₃ that list O⁺ ions responsible for the most damage creation amongst all ions investigated (*cf. Table 3.3*).

8.1.3 – Damage Depth Distribution

The 2013 SRIM code was used to calculate the damage depth distribution in terms of dpa for each target element of LiNbO₃. These results can be found in *Figure 8.3*.

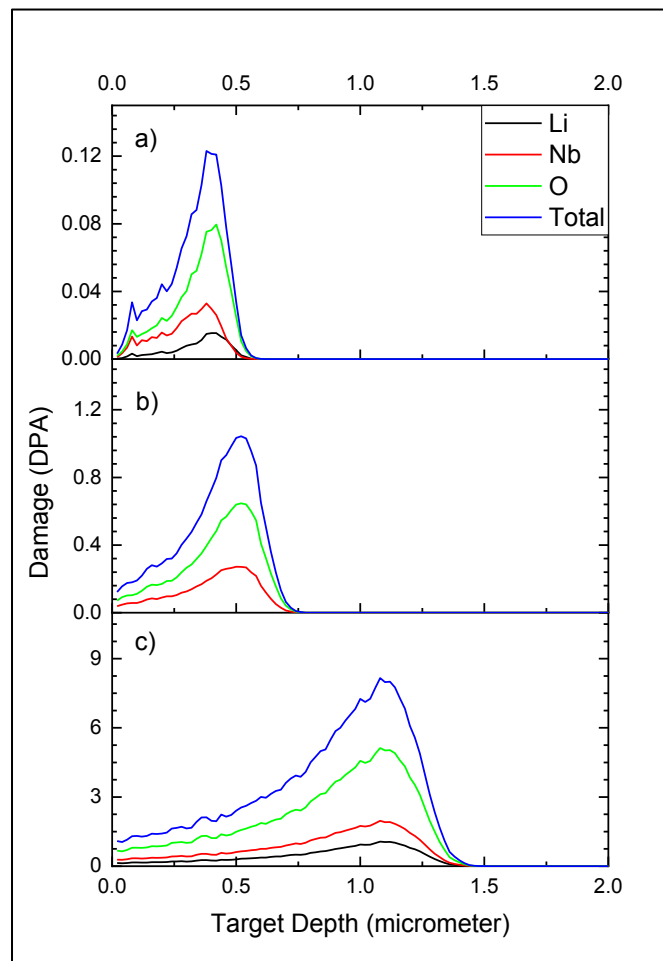


Figure 8.3: Damage depth distribution of a) H⁺, b) He⁺ and c) O⁺ ion irradiations in LiNbO₃.

From these results, it is apparent that irradiation with O⁺ ions leads to the furthest projected range in LiNbO₃, which supports previous calculations (*cf. Table 3.1*). For all three ions, it can be

observed that the creation of vacancies from displaced oxygen target atoms is the leading cause of damage in LiNbO_3 , with their percentages previously discussed in *Table 3.3*.

8.2 – Raman Spectroscopy

Raman spectroscopy measurements were obtained in order to evaluate the effects of ion radiation on the structure of LiNbO_3 . The results of these measurements can be found in *Figure 8.4*.

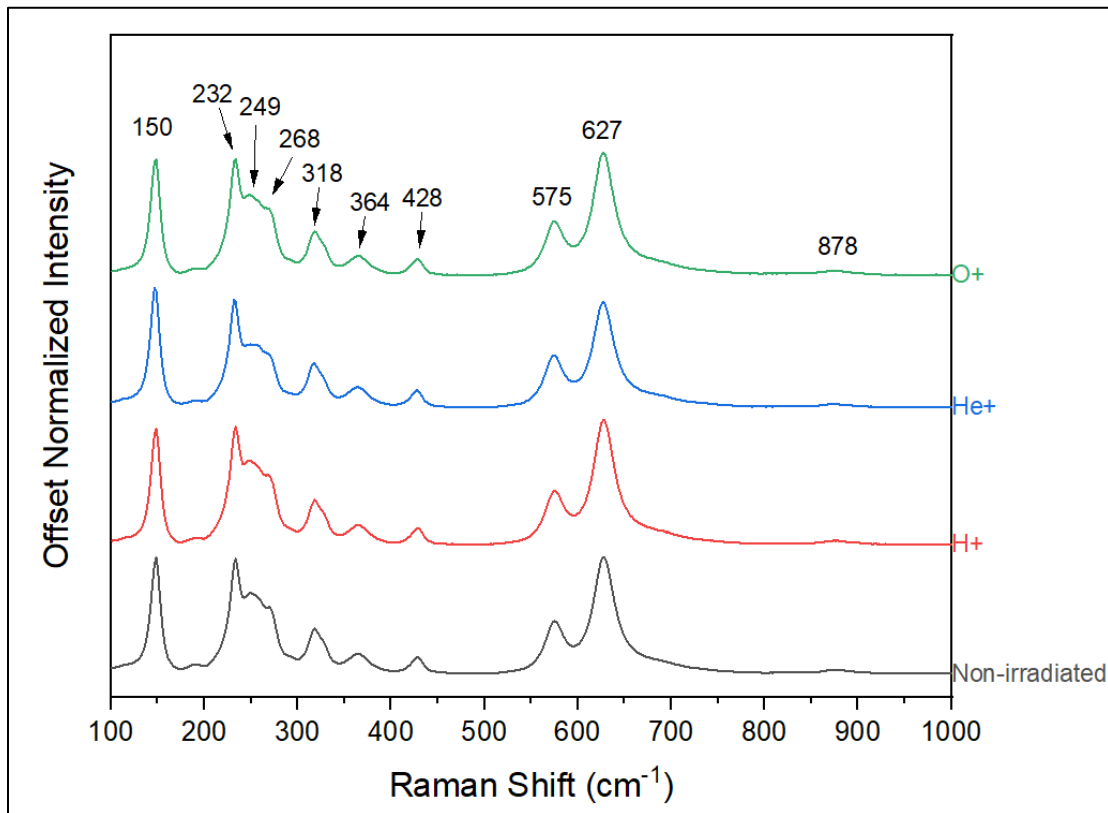


Figure 8.4: Raman spectra of pristine and irradiated LiNbO_3 samples offset by intensity.

From the Raman spectroscopy measurements, the presence of ten peaks was observed in each sample, therefore ion irradiation did not create or destroy any vibrational modes. The

observed peaks were compared with previous literature to determine the identity of the vibrational modes that were measured. These identified vibrational modes can be found in *Table 8.2*.^{1,2}

Table 8.2: Identified Raman vibrations of LiNbO₃.^{1,2}

This Work (cm⁻¹)	Literature (cm⁻¹)	Vibrations
150	156	Symmetric O vibrations
232	240	Degenerative O vibrations
249	253	Symmetric O vibrations
268	268	Degenerative O vibrations
318	324	Degenerative O vibrations
364	371	Degenerative O vibrations
428	434	Degenerative O vibrations
575	576	Degenerative O vibrations
627	632	Symmetric O vibrations
878	875	Valence bridge vibrations of Li-O-Nb

Raman spectra of all LiNbO₃ samples were normalized to the peak of greatest intensity that had the least superposition from nearby peaks (150 cm⁻¹). The spectra were also corrected by the neon lamp reference towards the determination of possible shifts in peak position. Changes in the peak FWHM were also evaluated (*Figure 8.5*).

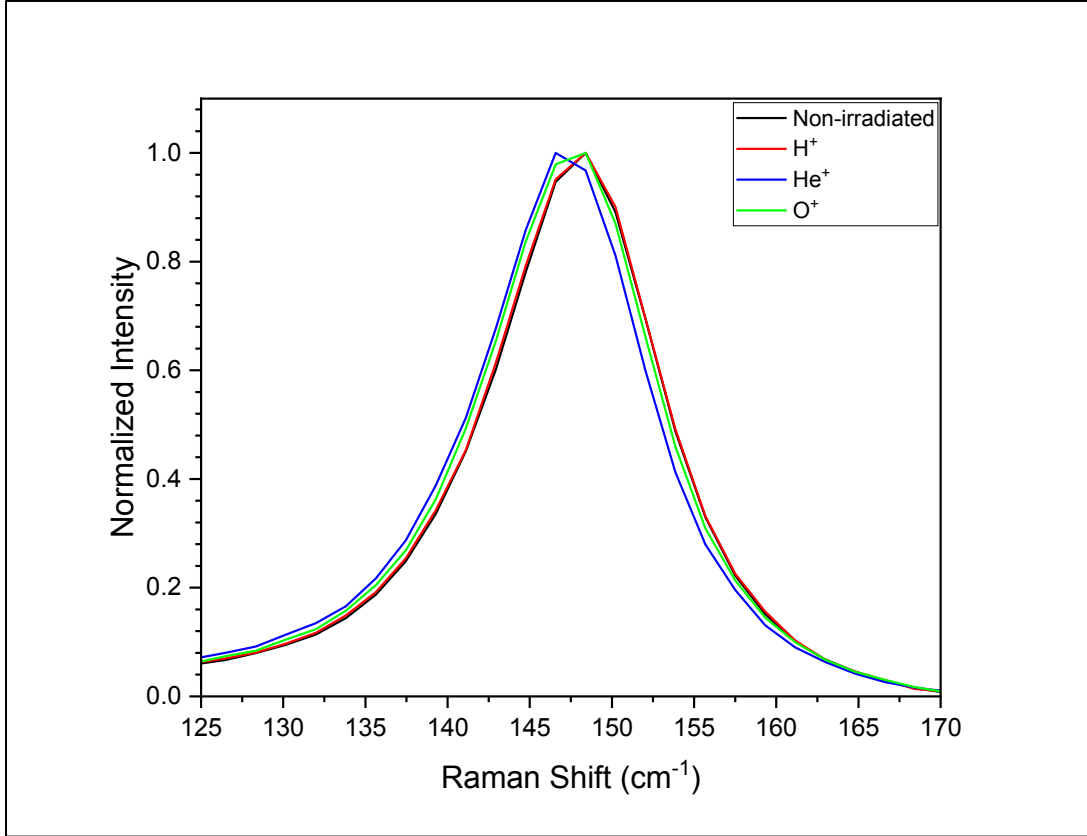


Figure 8.5: Overlay of pristine and irradiated LiNbO₃ Raman spectra after normalization and position correction.

Table 8.3: Changes of the Raman peak position and FWHM for irradiated LiNbO₃.

Sample	Peak Position (cm ⁻¹)	Peak FWHM (cm ⁻¹)
Non-irradiated	148.3	12.1
H ⁺	148.3	12.1
He ⁺	147.5	12.1
O ⁺	147.7	12.3

Analysis of the shifts in peak position due to ion irradiation of the LiNbO₃ samples revealed that the greatest shift was ~ 0.8 cm⁻¹ between the pristine sample and the He⁺ irradiated sample (Table 8.3). The analysis of the peak broadening revealed no increase of the FWHM of the irradiated samples when compared to the non-irradiated sample (Table 8.3). The magnitude of the

peak shift was determined to be within the experimental uncertainty under these experimental conditions. Therefore, the strain created by ion irradiation, if any, was minor.

8.3 – UV-Visible Optical Spectroscopy

UV-visible optical spectroscopy measurements were conducted in order to determine the effect of ion irradiation on the intensity of the absorbance bands in LiNbO_3 and general transmittance of light. The results of these measurements can be found in *Figure 8.6*.

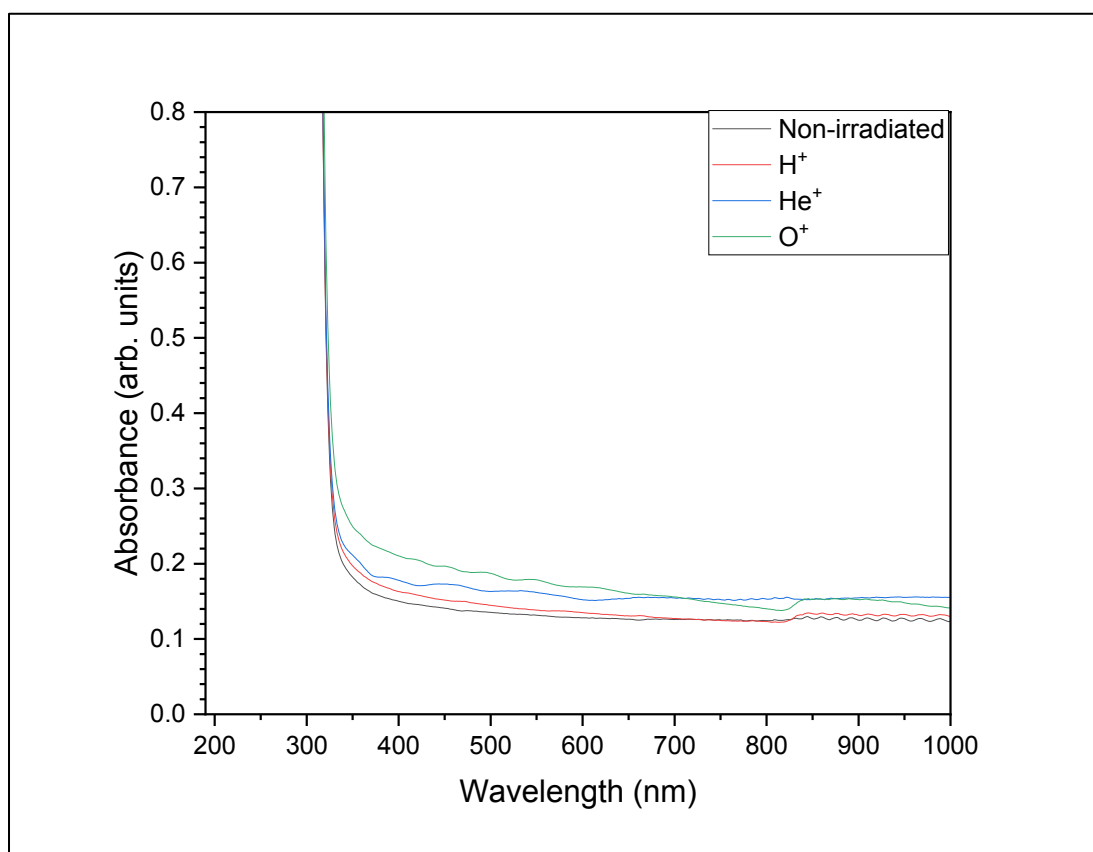


Figure 8.6: Optical absorption spectra of pristine and irradiated LiNbO_3 samples.

From these results, no absorption bands were observed in the pristine and in the irradiated LiNbO_3 samples. An intense absorption at ~ 320 nm is observed for all samples that has also been

previously determined to arise from the direct transition energy gap.³ The oscillating patterns seen in the spectra were attributed to light interference and should be disregarded.

An overall increase in the baseline absorption can be seen in all irradiated samples when compared to pristine LiNbO₃. This shift in absorption and its enhancement for lower wavelengths can be explained by an increase in Rayleigh scattering due to the creation of point defects due to ion irradiation as it was previously discussed in Chapter 4. This interpretation is supported since the increase in absorption was in general agreement with the total dpa, increasing from the H⁺ irradiated sample to the O⁺ irradiated one.

8.4 – Radioluminescence

RL measurements were conducted to determine the identity and possible changes of relative intensity of the luminescence centers due to ion irradiation in LiNbO₃. These measurements can be found in *Figure 8.7*.

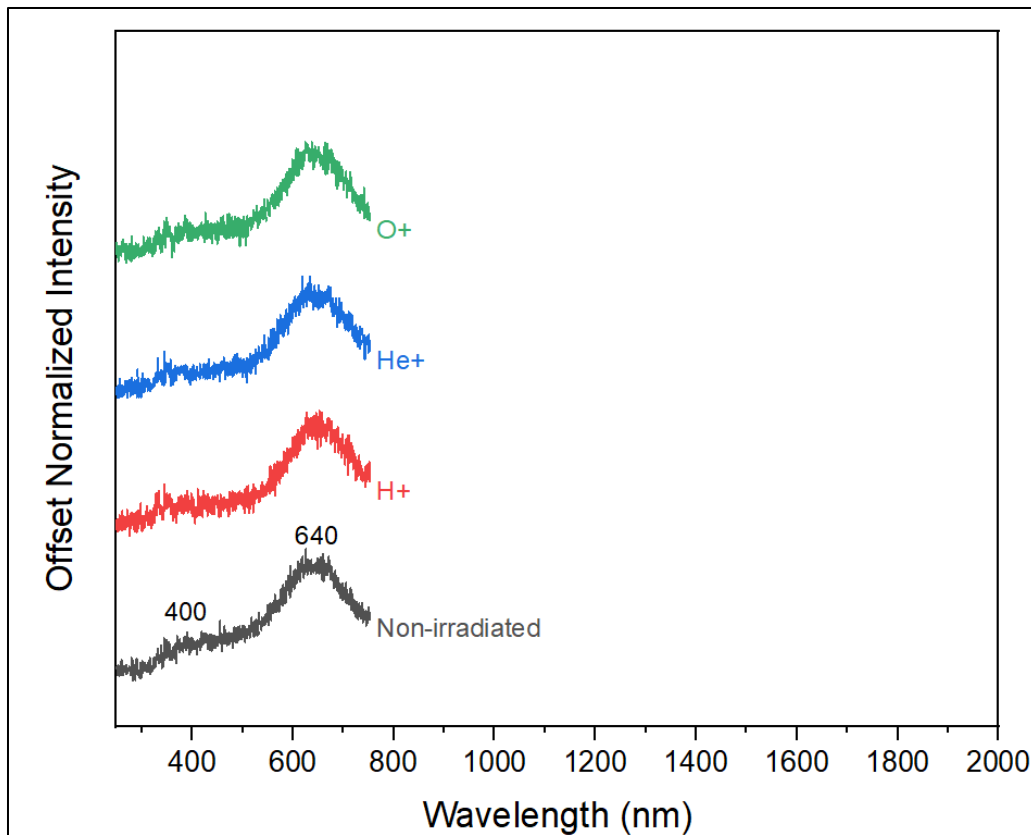


Figure 8.7: Offset RL spectra for pristine and irradiated LiNbO₃ samples.

From these results, two luminescent bands were observed including a broad-band centered at ~640 nm and a weak-band that is centered around 400 nm. Previous literature reported the ~400 nm band to be related to an electron-hole recombination in a niobate group⁴, while the band at 640 nm could not be identified. Since the optical transparency of the samples changed due to ion irradiation, the absolute RL intensity of the bands cannot be compared. The weak nature of the 400 nm band hindered further comparative analysis.

8.5 – Thermoluminescence

TL measurements were conducted to investigate how traps were affected by ion irradiation. The results of these measurements can be found in *Figure 8.8* below.

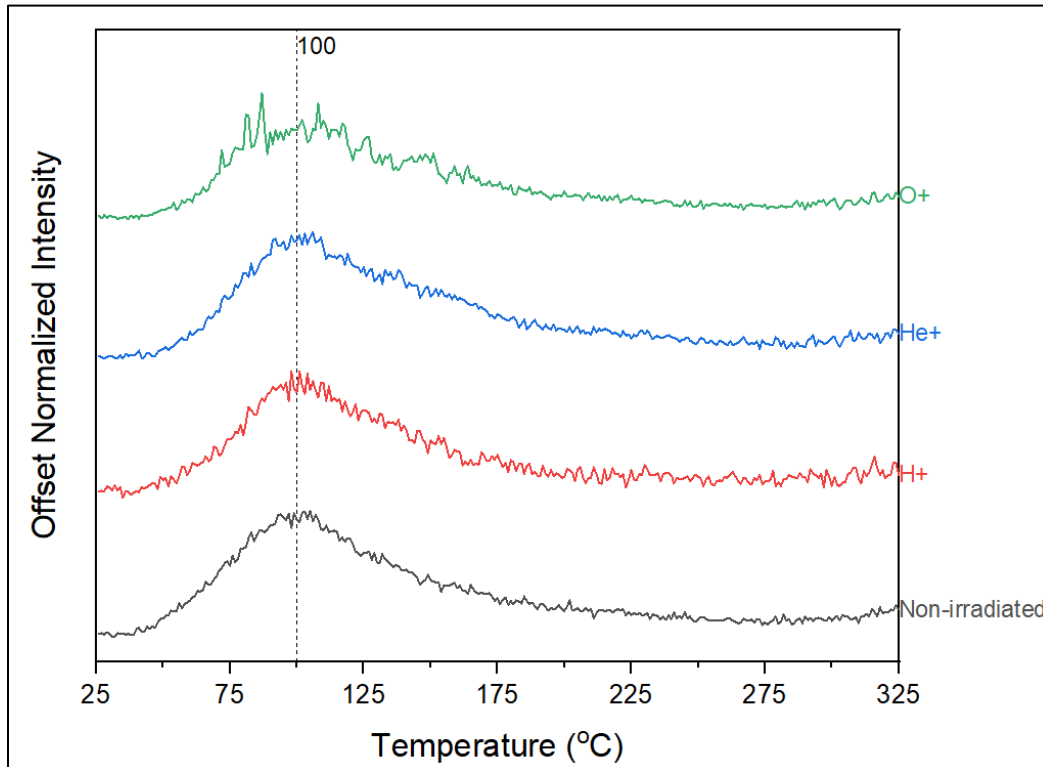


Figure 8.8: Glow curves of pristine and irradiated LiNbO₃ samples.

From the glow curves, the presence of one glow peak was observed at 100 °C in all irradiated samples and in the pristine sample. Visual analysis of the normalized glow curves shows a similar peak shape and peak position for all LiNbO₃ samples. The changes in optical transparency of the samples due to ion irradiation, all different from one another, and the presence of only one glow band hindered any further analysis of the TL results.

TL spectroscopy measurements were conducted to determine the identity of the recombination centers leading to the distinct glow peak seen in the glow curves (*Figure 8.8*). The results of these measurements can be found in *Figure 8.9*.

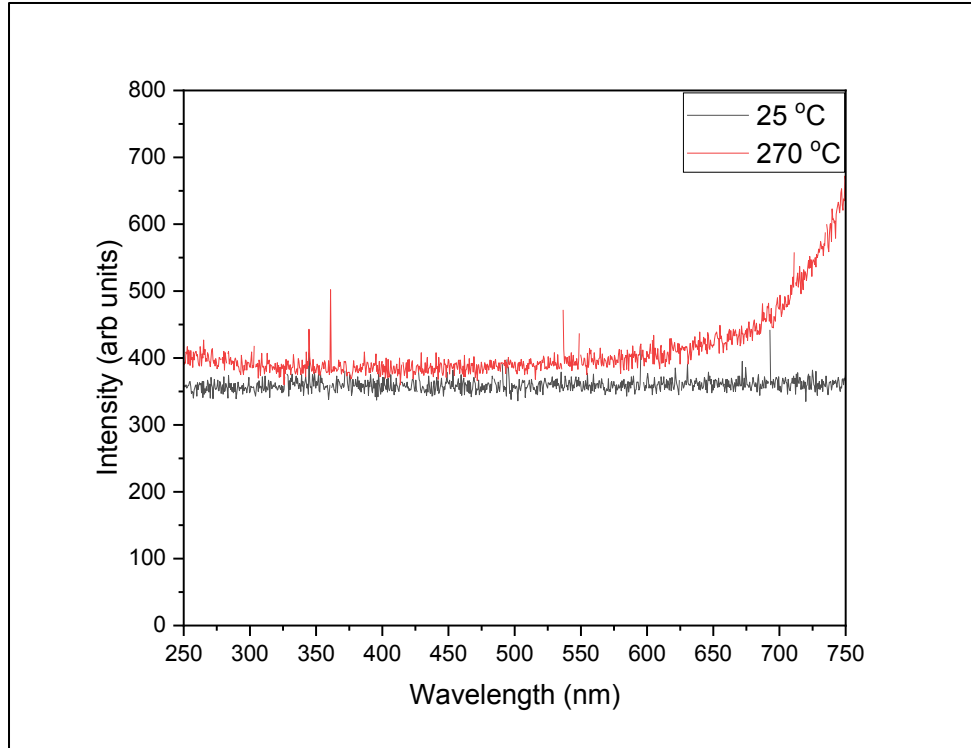


Figure 8.9: TL spectroscopy results of pristine LiNbO₃. The increase in intensity of the 270-400 °C spectrum corresponds to the contribution of the blackbody radiation of the system.

From the results of TL spectroscopy measurements, no luminescence centers could be detected.

TL reproducibility measurements were conducted to determine the possibility of electron traps existing at deeper energies in the pristine LiNbO₃ sample. The results of these measurements can be found in *Figure 8.10*.

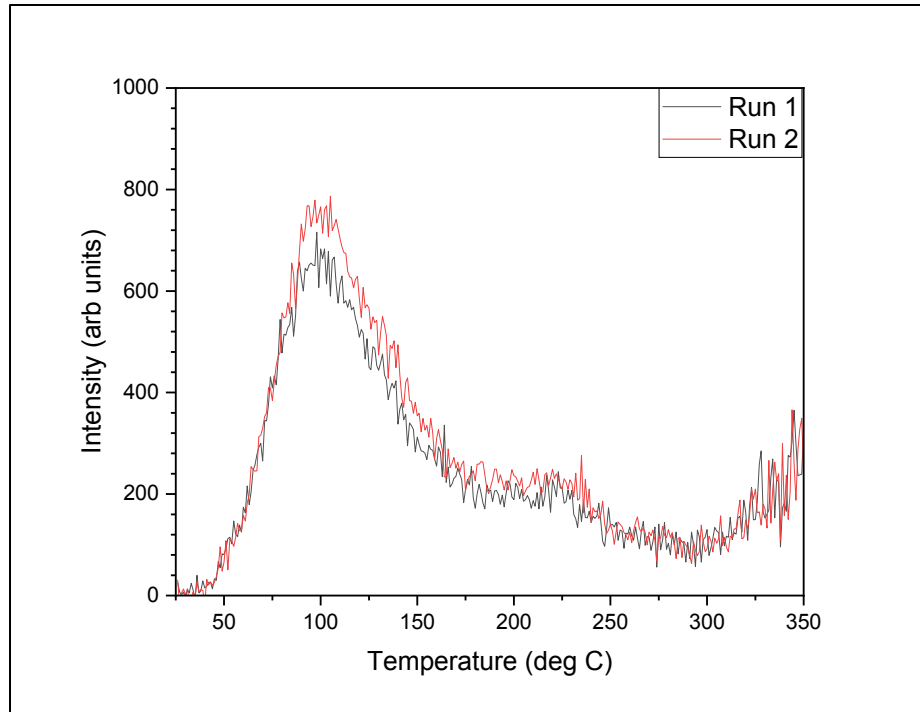


Figure 8.10: TL reproducibility measurements of pristine LiNbO₃.

From these TL curves, a minor change in peak intensity (~10%) is observed between the first and second run. Further, the relative intensity between the bands changed from the first set of measurements revealing some sensitivity of the TL response to the irradiation history. Consequently, TL was found to be of limited use for the desired radiation damage analysis.

8.6 – Summary of Results

In summary, optical absorption and TL measurements showed some general sensitivity to ion irradiation though none of the techniques used in this work could clearly characterize the effects of ion irradiation in this material.

CHAPTER NINE

SUMMARY, CONCLUSIONS, AND FUTURE WORK

Five functional ceramic materials underwent ion irradiation in order to study the effects of the near-Earth radiation environment on their structure and properties. 60 keV H⁺, 120 keV He⁺ and 1 MeV O⁺ ions with a total fluence of $5 \times 10^{16}/\text{cm}^2$ were used to irradiate single crystals of MgAl₂O₄, Y₃Al₅O₁₂, ZnO, YVO₄ and LiNbO₃. Monte-Carlo calculations were conducted using the 2013 SRIM software to characterize the interaction of ion irradiation with these materials, including the projected range and the total damage created. Raman spectroscopy was used to characterize structural changes, while radioluminescence, optical spectroscopy, and thermoluminescence were used to characterize their optical properties and the effects of ion irradiation on defects.

The first goal of this work was related to evaluating optical techniques, namely Raman spectroscopy, optical absorption/transmission, radioluminescence and thermoluminescence, to characterize radiation damage of ceramic materials. Overall, the characterization methods used in this work were able to successfully detect and characterize the effects of ion irradiation. However, optically active defects proved difficult to be used as markers for irradiation damage due to the change in optical transparency of the samples.

The other goal of this work was to evaluate the effects of ion irradiation on the structure and optical properties of ceramic materials. 2013 SRIM Monte Carlo calculations showed a general increase in projected range and damage creation (dpa) from H⁺ to He⁺ and O⁺. They provided detailed calculations on the contribution to damage of the target elements vacancies, and that damage tended to be higher in the oxygen sublattice for most materials. An exception was

MgAl₂O₄ where it happened in the Al sublattice. The Monte Carlo calculations also showed that sputtering was negligible in all cases.

In general, it was found that the ion irradiation effects on the optical properties were controlled by the dpa though, in some cases, chemical effects related to the nature of the bombarding ions may have played a role as well. Optical absorption and Raman spectroscopy were especially useful when specific bands related to defects were analyzed, though Raman spectroscopy revealed to be less useful for strain analysis than previously expected. However, specific conclusions are very dependent on the target material and the reader is directed to the summaries presented at the end of chapters 4 to 8 for details. Results from this work are currently being prepared for publication.

For future work, it is suggested to develop the hardware and methodology to transform both RL and TL into quantitative measurements where the absolute values can be analyzed, instead of being limited to relative intensity analysis. This will include correction for optical extinction and normalization of X-ray irradiation area. It is suggested to enhance the resolution of Raman spectroscopy measurements to be able to check for peak shifts below $\sim 1 \text{ cm}^{-1}$. In terms of the choice materials to be investigated, the specific technologies already in use in space technology or planned for use in future space missions should be considered. Meanwhile, irradiation conditions should be as close as possible to the conditions encountered in the specific space environment envisioned for the space mission under consideration. A natural expansion of this work would be to investigate the effects of high energy electron irradiation.

REFERENCES

CHAPTER ONE

1. Gershon, D. (1995). Down-to-earth medical benefits of Space Research. *Nature Medicine*, 1(5), 395–395. <https://doi.org/10.1038/nm0595-395>.
2. Xapsos, M. A., Stauffer, C., Jordan, T., Barth, J. L., & Mewaldt, R. A. (2007). Model for cumulative solar heavy ion energy and linear energy transfer spectra. *IEEE Transactions on Nuclear Science*, 54(6), 1985–1989. <https://doi.org/10.1109/tns.2007.910850>.
3. Naito, M., Kitamura, H., Koike, M., Kusano, H., Kusumoto, T., Uchihori, Y., Endo, T., Hagiwara, Y., Kiyono, N., Kodama, H., Matsuo, S., Mikoshiba, R., Takami, Y., Yamanaka, M., Akiyama, H., Nishimura, W., & Kodaira, S. (2021). Applicability of composite materials for space radiation shielding of spacecraft. *Life Sciences in Space Research*, 31, 71–79. <https://doi.org/10.1016/j.lssr.2021.08.004>.
4. Xapsos, O'Neill, & O'Brien, T. P. (2013). Near-earth space radiation models. *IEEE Transactions on Nuclear Science*, 60(3), 1691–1705. <https://doi.org/10.1109/tns.2012.2225846>.
5. Bourdarie, S. É., & Xapsos, M. (2008). The near-earth space radiation environment. *IEEE Transactions on Nuclear Science*, 55(4), 1810–1832. <https://doi.org/10.1109/tns.2008.2001409>.
6. Reeves, G. D., Spence, H. E., Henderson, M. G., Morley, S. K., Friedel, R. H., Funsten, H. O., Baker, D. N., Kanekal, S. G., Blake, J. B., Fennell, J. F., Claudepierre, S. G., Thorne, R. M., Turner, D. L., Kletzing, C. A., Kurth, W. S., Larsen, B. A., & Niehof, J. T. (2013). Electron acceleration in the heart of the Van Allen Radiation Belts. *Science*, 341(6149), 991–994. <https://doi.org/10.1126/science.1237743>.

7. Van Allen, J., Frank, L. (1959). Radiation Around the Earth to a Radial Distance of 107,400 km. *Nature* 183, 430–434. <https://doi.org/10.1038/183430a0>.
8. Schwadron, N.A., Cooper, J.F., Desai, M. *et al.* (2017). Particle Radiation Sources, Propagation, and Interactions in Deep Space, at Earth, the Moon, Mars, and Beyond: Examples of Radiation Interactions and Effects. *Space Sci Rev* 212, 1069–1106. <https://doi.org/10.1007/s11214-017-0381-5>.
9. Kovtyukh, A.S. (2018). Ion Composition of the Earth's Radiation Belts in the Range from 100 keV to 100 MeV/nucleon: Fifty Years of Research. *Space Sci Rev* 214, 124. <https://doi.org/10.1007/s11214-018-0560-z>
10. Johnson, R. G. (1983). Energetic ion composition in the Earth's magnetosphere. *Review of Geophysics and Space Physics* 17(4), 696-705. <https://doi.org/10.1007/978-94-009-7105-9>.
11. M. Maalouf, M. Durante and N. Foray. (2011). Biological Effects of Space Radiation on Human Cells: History, Advances and Outcomes. *Journal of Radiation Research* 52(2). 126-146. <http://doi.org/10.1269/jrr.10128>.
12. European Space Agency. (2020). Types of orbits. *ESA*. Retrieved March 20, 2022, from https://www.esa.int/Enabling_Support/Space_Transportation/Types_of_orbits
13. Suparta, W., & Zulkeple, S. K. (2014). Spatial analysis of galactic cosmic ray particles in low Earth orbit/near Equator Orbit using Spenvis. *Journal of Physics: Conference Series*, 495, 012040. <https://doi.org/10.1088/1742-6596/495/1/012040>.
14. The International Space Station Space Radiation. *NASA*. (n.d.). Retrieved March 20, 2022, from <https://ntrs.nasa.gov/citations/20200001591>

15. A systematic view of remote sensing. (2020). *Advanced Remote Sensing*, 2, 1–57.
<https://doi.org/10.1016/b978-0-12-815826-5.00001-5>
16. E.R Benton, E.V Benton. (2001). Space radiation dosimetry in low-Earth orbit and beyond. *Nuclear Instruments and Methods in Physics Research Section B: Beam Interactions with Materials and Atoms*, 184, 255-294. [https://doi.org/10.1016/S0168-583X\(01\)00748-0](https://doi.org/10.1016/S0168-583X(01)00748-0).
17. U. J. Nwankwo, V., N. Jibiri, N., & T. Kio, M. (2020). The impact of space radiation environment on satellites operation in near-earth space. *Satellites Missions and Technologies for Geosciences*. InTechOpen. <https://doi.org/10.5772/intechopen.90115>.
18. National Academies of Sciences, Engineering, and Medicine. (2018). Testing at the Speed of Light: The State of U.S. Electronic Parts Space Radiation Testing Infrastructure. Washington, DC: The National Academies Press. <https://doi.org/10.17226/24993>.
19. The European Space Agency. (2011). *Catastrophic 'latch-up' due to heavy ion*. ESA. Retrieved March 20, 2022, from https://www.esa.int/ESA_Multimedia/Images/2011/06/Catastrophic_latchup_due_to_heavy_ion
20. Hoffpauir, D. (2016). *Understanding the potential dangers of spacecraft charging*. NASA. Retrieved March 20, 2022, from <https://www.nasa.gov/offices/nesc/articles/understanding-the-potential-dangers-of-spacecraft-charging/>
21. Nastasi, M., Mayer, J., & Hirvonen, J. (1996). *Ion-Solid Interactions: Fundamentals and Applications* (Cambridge Solid State Science Series). Cambridge: Cambridge University Press. doi:10.1017/CBO9780511565007

22. Maurer, Richard & Fraeman, Martin & Martin, Mark & Roth, David. (2008). Harsh Environments: Space Radiation Environment, Effects, and Mitigation. *John Hopkins Technical Digest*. 28. 17-29.
23. J. R. Srour and J. W. Palko. (2013). Displacement Damage Effects in Irradiated Semiconductor Devices. *IEEE Transactions on Nuclear Science*. 60(3). 1740-1766. <http://doi.org/10.1109/TNS.2013.2261316>.
24. Pearton, S. J., Aitkaliyeva, A., Xian, M., Ren, F., Khachatryan, A., Ildefonso, A., Islam, Z., Jafar Rasel, M. A., Haque, A., Polyakov, A. Y., & Kim, J. (2021). Review-Radiation Damage in Wide and Ultra-Wide Bandgap Semiconductors. *ECS Journal of Solid State Science and Technology*, 10(5), [055008]. <https://doi.org/10.1149/2162-8777/abfc23>.
25. Miyahira, T., Johnston, A.H., Becker, H.N., Lalumondiere, S.D., & Moss, S.C. (2001). Catastrophic latchup in CMOS analog-to-digital converters. *IEEE Transactions on Nuclear Science*, 48, 1833-1840.
26. J. R. Srour and J. M. McGarrity. (1988). Radiation effects on microelectronics in space. *Proceedings of the IEEE*, 76(11). 1443-1469. <http://doi.org/10.1109/5.90114>.
27. Stone, E. & Cohen, C. & Cook, W. & Cummings, A.C. & Gauld, B. & Kecman, Branislav & Leske, R.A. & Mewaldt, Richard & Thayer, M. & Dougherty, B. & Grumm, R. & Milliken, B. & Radocinski, R. & Wiedenbeck, M. & Christian, Eric & Shuman, S. & Rosenvinge, T. (1998). The Solar Isotope Spectrometer for the Advanced Composition Explorer. *Space Science Reviews*. 86. 357-408. <http://doi.org/10.1023/A:1005027929871>.
28. Hathaway, David. (2010). The Solar Cycle. *Living Reviews in Solar Physics*. 7. 10.1007/lrsp-2010-1.

29. Bisschoff, D., Potgieter, M. S., & Aslam, O. P. (2019). New very local interstellar spectra for electrons, positrons, protons, and light cosmic ray nuclei. *The Astrophysical Journal*, 878(1), 59. <https://doi.org/10.3847/1538-4357/ab1e4a>.
30. Fletcher, L., Dennis, B.R., Hudson, H.S. *et al.* (2011). An Observational Overview of Solar Flares. *Space Sci Rev* 159(19). 19-106. <https://doi.org/10.1007/s11214-010-9701-8>.
31. Ryan Manuel D. Guido, Jason B. Kalaw. (2019). Characterizing Coronal Mass Ejections in Solar Cycle Analysis, *International Journal of Astronomy*, 8(1), 1-7. <http://doi.org/10.5923/j.astronomy.20190801.01>.
32. Kilcik, A., Yurchyshyn, V. B., Abramenko, V., Goode, P. R., Gopalswamy, N., Ozguc, A., & Rozelot, J. P. (2011). Maximum coronal mass ejection speed as an indicator of solar and geomagnetic activities. *Astrophysical Journal*, 727(1). <https://doi.org/10.1088/0004-637X/727/1/44>.
33. Vencloviene, J., Babarskiene, R. & Slapikas, R. (2013). The association between solar particle events, geomagnetic storms, and hospital admissions for myocardial infarction. *Nature Hazards* 65, 1–12. <https://doi.org/10.1007/s11069-012-0310-6>.
34. Li, W., & Hudson, M. K. (2019). Earth's Van Allen radiation belts: From discovery to the Van Allen Probes era. *Journal of Geophysical Research: Space Physics*, 124, 8319– 8351. <https://doi.org/10.1029/2018JA025940>
35. Murty, K. L., & Charit, I. (2013). *An introduction to nuclear materials: Fundamentals and applications*. Wiley-VCH.
36. Crawford, J. H., Slifkin, L. M. (1972). Defect Creation by Radiation in Polar Crystals. *Point Defects in Solids*, 1. 90-201. Plenum Press.

37. Ziegler, J. F., Biersack, J., & Ziegler, M. D. (2015). *SRIM - The Stopping and Range of Ions in Matter*. SRIM.
38. Donahue, W., Newhauser, W. D., & Ziegler, J. F. (2016). Analytical model for ion stopping power and range in the therapeutic energy interval for beams of hydrogen and heavier ions. *Physics in medicine and biology*, *61*(17), 6570–6584.
<https://doi.org/10.1088/0031-9155/61/17/6570>.
39. Nordlund, Kai & Ghaly, Mai & Averback, R. & Caturla, María & Diaz de la Rubia, Tomas & Tarus, Jura. (1998). Defect production in collision cascades in elemental semiconductors and FCC metals. *Physics Review B*. *57*. 7556-7570.
<http://doi.org/10.1103/PhysRevB.57.7556>.
40. Kai Nordlund, Steven J. Zinkle, Andrea E. Sand, Fredric Granberg, Robert S. Averback, Roger E. Stoller, Tomoaki Suzudo, Lorenzo Malerba, Florian Banhart, William J. Weber, Francois Willaime, Sergei L. Dudarev, David Simeone. (2018). Primary radiation damage: A review of current understanding and models, *Journal of Nuclear Materials*, *512*, 450-479, ISSN 0022-3115, <https://doi.org/10.1016/j.jnucmat.2018.10.027>.
41. R.E Williford, R Devanathan, W.J Weber. Computer simulation of displacement energies for several ceramic materials. (1998). *Nuclear Instruments and Methods in Physics Research Section B: Beam Interactions with Materials and Atoms*, *141*(1-4). 94-98, ISSN 0168-583X, [https://doi.org/10.1016/S0168-583X\(98\)00066-4](https://doi.org/10.1016/S0168-583X(98)00066-4).
42. S.J. Zinkle, C. Kinoshita. (1997). Defect production in ceramics. *Journal of Nuclear Materials*, *251*, 200-217, ISSN 0022-3115, [https://doi.org/10.1016/S0022-3115\(97\)00224-9](https://doi.org/10.1016/S0022-3115(97)00224-9).

43. S. Agarwal, Y. Lin, C. Li, R.E. Stoller, S.J. Zinkle. (2021). On the use of SRIM for calculating vacancy production: Quick calculation and full-cascade options, *Nuclear Instruments and Methods in Physics Research Section B: Beam Interactions with Materials and Atoms*, 503, 11-29, ISSN 0168-583X, <https://doi.org/10.1016/j.nimb.2021.06.018>.
44. Kinchin, G. H., Pease, R. S. (1955). The displacement of atoms in solids by radiation. *Reports on Progress in Physics*, 18(1), 1–51. <https://doi.org/10.1088/0034-4885/18/1/301>
45. Nastasi, M., Mayer, J., & Hirvonen, J. (1996). Interatomic potentials. *Ion-Solid Interactions: Fundamentals and Applications* (Cambridge Solid State Science Series, pp. 14-38). Cambridge: Cambridge University Press. <http://doi.org/10.1017/CBO9780511565007.003>
46. S.J. Zinkle, C. Kinoshita. (1997). Defect production in ceramics, *Journal of Nuclear Materials*, 251, 200-217, ISSN 0022-3115, [https://doi.org/10.1016/S0022-3115\(97\)00224-9](https://doi.org/10.1016/S0022-3115(97)00224-9).LM.
47. Wang L.M., S.X. Wang, W.L. Gong, W.L. Gong, R.C. Ewing, and W.J. Weber. (1998). Amorphization of Ceramic Materials by Ion Beam Irradiation. *Materials Science and Engineering. A. Structural Materials: Properties, Microstructure and Processing* 253(1-2).106-113.
48. Chapter 4: Design for Radiation Tolerance. NASA. (2020). Retrieved March 20, 2022, from http://www.pld.guru/_hdl/2/_ref/nppp.jpl.nasa.gov/asic/Sect.3.4.html

CHAPTER TWO

1. R.E Williford, R Devanathan, W.J Weber. (1998). Computer simulation of displacement energies for several ceramic materials, *Nuclear Instruments and Methods in Physics Research Section B: Beam Interactions with Materials and Atoms*, 141(1–4), 94-98, ISSN 0168-583X, [https://doi.org/10.1016/S0168-583X\(98\)00066-4](https://doi.org/10.1016/S0168-583X(98)00066-4).
2. Weis, R.S., Gaylord, T.K. (1985). Lithium niobate: Summary of physical properties and crystal structure. *Appl. Phys. A* 37, 191–203. <https://doi.org/10.1007/BF00614817>.
3. Ibram, Ganesh. (2013). A Review on Magnesium Aluminate (MgAl₂O₄) Spinel: Synthesis, Processing and Applications. *International Materials Reviews*. 58. 63-112. <http://doi.org/10.1179/1743280412Y.0000000001>.
4. YVO₄ crystal. MTI Corp. (2021). Retrieved March 20, 2022, from <https://www.mtixtl.com/yvo411110x10x05mm1sp.aspx>.
5. ZnO crystal. MTI Corp. (2021). Retrieved March 20, 2022, from <https://www.mtixtl.com/zno00015x5x05mm2sp-1.aspx>.
6. Márius Pavlovič, Ivan Strašík. (2007). Supporting routines for the SRIM code. *Nuclear Instruments and Methods in Physics Research Section B: Beam Interactions with Materials and Atoms*, 257(1–2). 601-604, ISSN 0168-583X, <https://doi.org/10.1016/j.nimb.2007.01.047>.
7. Thierfelder, C., Sanna, S., Schindlmayr, A., & Schmidt, W. G. (2010). Do we know the band gap of lithium niobate? *Physica Status Solidi C*, 7(2), 362–365. <https://doi.org/10.1002/pssc.200982473>.
8. Yan, Wan & Li, Meiyu & Xie, Erjuan & Xu, Shoulei & Huang, Yuyang & Deng, Wen. (2017). Luminescent properties and first-principles calculations of (Cr,Ca):YAG crystals.

International Journal of Modern Physics B. 31. 1744070.

<http://doi.org/10.1142/S0217979217440702>.

9. Chandrashekar, C.K., Madhusudan, P., Shivaraju, H.P. *et al.* (2018). Synthesis of rare earth-doped yttrium vanadate polyscale crystals and their enhanced photocatalytic degradation of aqueous dye solution. *International Journal of Environmental Science and Technology* 15, 427–440. <https://doi.org/10.1007/s13762-017-1401-4>.
10. Srikant, V. & Clarke, David. (1998). On the Optical Band Gap of Zinc Oxide. *Journal of Applied Physics*. 83. 5447-5451. <http://doi.org/10.1063/1.367375>.
11. J. Friedrich, Methods for Bulk Growth of Inorganic Crystals: Crystal Growth, Reference Module. *Materials Science and Materials Engineering*, Elsevier, 2016, ISBN 9780128035818, <https://doi.org/10.1016/B978-0-12-803581-8.01010-9>.
12. S.-H. Feng, G.-H. Li, Chapter 4 - Hydrothermal and Solvothermal Syntheses, Editor(s): Ruren Xu, Yan Xu, *Modern Inorganic Synthetic Chemistry (Second Edition)*, Elsevier, 2017, Pages 73-104, ISBN 9780444635914, <https://doi.org/10.1016/B978-0-444-63591-4.00004-5>.
13. Accelerator Laboratory. Texas A&M University Engineering. (2016). Retrieved March 20, 2022, from <https://engineering.tamu.edu/nuclear/research/facilities/accelerator-laboratory.html>.
14. Interactions of ions with matter. James Ziegler – SRIM & TRIM. (2013). Retrieved March 20, 2022, from <http://srim.org>.
15. Ziegler, J. F., Biersack, J., & Ziegler, M. D. (2015). *SRIM - The Stopping and Range of Ions in Matter*. SRIM.

16. Nebu John, Sony George, Chapter 5 - Raman Spectroscopy, Editor(s): Sabu Thomas, Raju Thomas, Ajesh K. Zachariah, Raghvendra Kumar Mishra, *Micro and Nano Technologies, Spectroscopic Methods for Nanomaterials Characterization*, Elsevier, 2017, Pages 95-127, ISBN 9780323461405, <https://doi.org/10.1016/B978-0-323-46140-5.00005-4>.
17. Leng, Y. (2013). Chapter 9: Vibrational Spectroscopy for Molecular Analysis. In *Materials characterization: Introduction to microscopic and spectroscopic methods* (2). Print. Wiley.
18. L. Pan, S. Sholom, S.W.S. McKeever, L.G. Jacobsohn. (2021). Magnesium aluminate spinel for optically stimulated luminescence dosimetry. *Journal of Alloys and Compounds*, 880, 160503, ISSN 0925-8388, <https://doi.org/10.1016/j.jallcom.2021.160503>.
19. Ming Zhang & Ekhard K.H. Salje. (2003). Spectroscopic Characterization of Metamictization and Recrystallization in Zircon and Titanite, *Phase Transitions*, 76(1-2). 117-136. <http://doi.org/10.1080/0141159031000076093>.
20. Shimizu, Rentaro & Ogasawara, Yoshihide. (2014). Radiation damage to Kokchetav UHPM diamonds in zircon: Variations in Raman, photoluminescence, and cathodoluminescence spectra. *Lithos*. 206. <http://doi.org/10.1016/j.lithos.2014.07.002>.
21. Kim, S. B., Hammaker, R. M., & Fateley, W. G. (1986). Calibrating Raman spectrometers using a neon lamp. *Applied Spectroscopy*, 40(3), 412–415. <https://doi.org/10.1366/0003702864509231>.
22. Niamh NicDaéid, Forensic Sciences: Systematic Drug Identification, Editor(s): Paul Worsfold, Colin Poole, Alan Townshend, Manuel Miró, *Encyclopedia of Analytical*

- Science (Third Edition)*, Academic Press, 2019, Pages 75-80, ISBN 9780081019849, <https://doi.org/10.1016/B978-0-12-409547-2.14457-9>.
23. Granite, S. (2021). Beer Lambert law: Transmittance & Absorbance. *Edinburgh Instruments*. Retrieved February 22, 2022, from <https://www.edinst.com/blog/the-beer-lambert-law/>.
24. J.N. Demas, S.E. Demas. Luminescence, *Reference Module in Chemistry, Molecular Sciences and Chemical Engineering*, Elsevier, 2014, ISBN 9780124095472, <https://doi.org/10.1016/B978-0-12-409547-2.11000-5>.
25. R. Capelletti. Luminescence, *Reference Module in Materials Science and Materials Engineering*, Elsevier, 2017, ISBN 9780128035818, <https://doi.org/10.1016/B978-0-12-803581-8.01247-9>.
26. Tobias Schulz, Martin Albrecht, Klaus Irmscher. Chapter 7 - Spatially Resolved Thermoluminescence in a Scanning Electron Microscope, Editor(s): Peter W. Hawkes, *Advances in Imaging and Electron Physics*, Elsevier, *Volume 168*, 2011, Pages 337-359, ISSN 1076-5670, ISBN 9780123859839, <https://doi.org/10.1016/B978-0-12-385983-9.00007-7>.

CHAPTER THREE

1. Interactions of ions with matter. James Ziegler – SRIM & TRIM. (2013). Retrieved March 20, 2022, from <http://srim.org>.
2. Ziegler, J. F., Biersack, J., & Ziegler, M. D. (2015). *SRIM - The Stopping and Range of Ions in Matter*. SRIM.
3. Donahue, W., Newhauser, W. D., & Ziegler, J. F. (2016). Analytical model for ion stopping power and range in the therapeutic energy interval for beams of hydrogen and heavier ions. *Physics in medicine and biology*, *61*(17), 6570–6584.
<https://doi.org/10.1088/0031-9155/61/17/6570>.
4. Bird, J. R., & Williams, J. S. (1989). Chapter 1: Ion Beam Analysis. In *Ion Beams for materials analysis*. Print, Academic Press.
5. ZnO crystal. MTI Corp. (2021). Retrieved March 20, 2022, from <https://www.mtixtl.com/zno00015x5x05mm2sp-1.aspx>.
6. M. Vijayalakshmi. (2017). Chapter 17 - Materials Response Under Irradiation. Editor(s): A.K. Tyagi, S. Banerjee, *Materials Under Extreme Conditions*, Elsevier, 615-650, ISBN 9780128013007, <https://doi.org/10.1016/B978-0-12-801300-7.00017-6>.

CHAPTER FOUR

1. L. Pan, S. Sholom, S.W.S. McKeever, L.G. Jacobsohn. (2021). Magnesium aluminate spinel for optically stimulated luminescence dosimetry, *Journal of Alloys and Compounds*, 880, 160503, ISSN 0925-8388, <https://doi.org/10.1016/j.jallcom.2021.160503>.
2. Shimizu, Rentaro & Ogasawara, Yoshihide. (2014). Radiation damage to Kokchetav UHPM diamonds in zircon: Variations in Raman, photoluminescence, and cathodoluminescence spectra. *Lithos*. 206. <http://doi.org/10.1016/j.lithos.2014.07.002>.
3. Sawai, Shigeto; Uchino, Takashi (2012). Visible photoluminescence from MgAl₂O₄ spinel with cation disorder and oxygen vacancy. *Journal of Applied Physics*, 112(10), 103523. <http://doi.org/10.1063/1.4767228>.
4. Summers, G. P.; White, G. S.; Lee, K. H.; Crawford, J. H. (1980). Radiation damage in MgAl₂O₄. *Physical Review B*, 21(6), 2578–2584. <http://doi.org/10.1103/PhysRevB.21.2578>.
5. Li, Qiuyue; Liu, Tingyu; Xu, Xun; Wang, Xueli; Guo, Rui; Jiao, Xuping; Lu, Yazhou (2020). Study on the optical spectra of MgAl₂O₄ with oxygen vacancies. *Materials Technology*, 1, 1–7. <http://doi.org/10.1080/10667857.2020.1750163>.
6. Guo, R., & Lee, S. (2020). Mie scattering of phonons by point defects in IV-vi semiconductors PBTE and GETE. *Materials Today Physics*, 12, 100-177. <https://doi.org/10.1016/j.mtphys.2020.100177>.
7. E.M. Yoshimura, E.G. Yukihara. (2006). Optically stimulated luminescence of magnesium aluminate (MgAl₂O₄) spinel, *Radiation Measurements*, 41(2), 163-169, ISSN 1350-4487, <https://doi.org/10.1016/j.radmeas.2005.09.001>.

8. Ibarra, A., Mariani, D. F., & Jiménez de Castro, M. (1991). Thermoluminescent processes of MgAl_2O_4 irradiated at room temperature. *Physical Review B*, 44(22), 12158–12165. <http://doi.org/10.1103/physrevb.44.12158>.
9. A. Lorincz, M. Puma, F. J. James, and J. H. Crawford Jr. (1982). Thermally stimulated processes involving defects in γ - and x-irradiated spinel (MgAl_2O_4). *Journal of Applied Physics* 53, 927-932. <https://doi.org/10.1063/1.330562>.

CHAPTER FIVE

1. S. Kostić, Z.Ž. Lazarević, V. Radojević, A. Milutinović, M. Romčević, N.Ž. Romčević, A. Valčić. (2015). Study of structural and optical properties of YAG and Nd:YAG single crystals, *Materials Research Bulletin*, 63, 80-87, ISSN 0025-5408, <https://doi.org/10.1016/j.materresbull.2014.11.033>.
2. Yu. Zorenko, T. Voznyak, V. Gorbenko, E. Zych, S. Nizankovski, A. Dan'ko, V. Puzikov. (2011). Luminescence properties of Y₃Al₅O₁₂:Ce nanoceramics, *Journal of Luminescence*, 131(1), 17-21, ISSN 0022-2313, <https://doi.org/10.1016/j.jlumin.2010.08.015>.
3. Springis, M., Pujats, A., & Valbis, J. (1991). Polarization of luminescence of colour centres in yag crystals. *Journal of Physics: Condensed Matter*, 3(28), 5457–5461. <https://doi.org/10.1088/0953-8984/3/28/021>.
4. A. Pujats & M. Springis. (2001). The F-type centres in YAG crystals, *Radiation Effects and Defects in Solids*, 155(1-4), 65-69. <http://doi.org/10.1080/10420150108214094>.
5. Zorenko, Y., Voloshinovskii, A., Savchyn, V., Voznyak, T., Nikl, M., Nejezchleb, K., Mikhailin, V., Kolobanov, V. and Spassky, D. (2007), Exciton and antisite defect-related luminescence in Lu₃Al₅O₁₂ and Y₃Al₅O₁₂ garnets. *Phys. Stat. in Solids B*, 244, 2180-2189. <https://doi.org/10.1002/pssb.20064243>.
6. C. R. Varney, S. M. Reda, D. T. Mackay, M. C. Rowe, and F. A. Selim. (2011). Strong visible and near infrared luminescence in undoped YAG single crystals", *AIP Advances* 1, 042170. <https://doi.org/10.1063/1.3671646>.
7. Kinsman, K. M., McKittrick, J., Sluzky, E., and Hesse, K. (1994). Phase development and luminescence in chromium-doped yttrium aluminum garnet (YAG:CR) phosphors.

Journal of the American Ceramic Society, 77(11), 2866–2872. <https://doi.org/10.1111/j.1151-2916.1994.tb04516.x>.

8. R.A Rodríguez-Rojas, E De la Rosa-Cruz, L.A Díaz-Torres, P Salas, R Meléndrez, M Barboza-Flores, M.A Meneses-Nava, O Barbosa-García, (2004). Preparation, photo- and thermo-luminescence characterization of Tb³⁺ and Ce³⁺ doped nanocrystalline Y₃Al₅O₁₂ exposed to UV-irradiation. *Optical Materials*, 25(3). 285-293, ISSN 0925-3467. <https://doi.org/10.1016/j.optmat.2003.07.001>.
9. S., M. K. S. W. (1988). *Thermoluminescence of Solids*. Cambridge University Press.

CHAPTER SIX

1. Damen, T. C., Porto, S. P., & Tell, B. (1966). Raman effect in zinc oxide. *Physical Review*, *142*(2), 570–574. <https://doi.org/10.1103/physrev.142.570>.
2. Calleja, J. M., & Cardona, M. (1977). Resonant Raman scattering in ZnO. *Physical Review B*, *16*(8), 3753–3761. <https://doi.org/10.1103/physrevb.16.3753>.
3. Arguello, C. A., Rousseau, D. L., & Porto, S. P. (1969). First-order Raman effect in wurtzite-type crystals. *Physical Review*, *181*(3), 1351–1363. <https://doi.org/10.1103/physrev.181.1351>.
4. Cuscó, R., Alarcón-Lladó, E., Ibáñez, J., Artús, L., Jiménez, J., Wang, B., & Callahan, M. J. (2007). Temperature dependence of raman scattering in ZnO. *Physical Review B*, *75*(16). <https://doi.org/10.1103/physrevb.75.165202>.
5. Raphael Lucas de Sousa e Silva, A. Franco Jr. (2020). Raman spectroscopy study of structural disorder degree of ZnO ceramics, *Materials Science in Semiconductor Processing*, *119*, 105227, ISSN 1369-8001, <https://doi.org/10.1016/j.mssp.2020.105227>.
6. 2. Xiong, G., Pal, U., & Serrano, J. G. (2007). Correlations among size, defects, and photoluminescence in ZnO nanoparticles. *Journal of Applied Physics*, *101*(2), 024317. [doi:10.1063/1.2424538](https://doi.org/10.1063/1.2424538).
7. Šćepanović, M., Grujić-Brojčin, M., Vojisavljević, K., Bernik, S. and Srećković, T. (2010), Raman study of structural disorder in ZnO nanopowders. *J. Raman Spectrosc.*, *41*: 914-921. <https://doi.org/10.1002/jrs.2546>.
8. Rodnyi, P.A., & Khodyuk, I.V. (2011). Optical and luminescence properties of zinc oxide (Review). *Optics and Spectroscopy*, *111*, 776-785. <http://doi.org/10.1134/S0030400X11120216>.

9. Guoqiang Zhao, Menglin Qiu, Guangfu Wang, Tingshun Wang, Jinfu Zhang. (2022). Temperature dependence of ZnO crystals from ion-beam-induced luminescence, *Journal of Luminescence*, 241, 118465, ISSN 0022-2313, <https://doi.org/10.1016/j.jlumin.2021.118465>.
10. 4. E.D. Bourret-Courchesne, S.E. Derenzo, M.J. Weber. (2009). Development of ZnO:Ga as an ultra-fast scintillator, *Nuclear Instruments and Methods in Physics Research Section A: Accelerators, Spectrometers, Detectors and Associated Equipment*, 601(3), 358-363, ISSN 0168-9002, <https://doi.org/10.1016/j.nima.2008.12.206>.

CHAPTER SEVEN

1. A. Chaves, S.P.S. Porto. (1972). Raman scattering of YVO₄, *Solid State Communications*, 10(11). 1075-1077. ISSN 0038-1098, [https://doi.org/10.1016/0038-1098\(72\)90899-X](https://doi.org/10.1016/0038-1098(72)90899-X).
2. A. Jayaraman, G.A. Kourouklis, G.P. Espinosa, A.S. Cooper, L.G. Van Uitert, (1987). A high-pressure Raman study of yttrium vanadate (YVO₄) and the pressure-induced transition from the zircon-type to the scheelite-type structure, *Journal of Physics and Chemistry of Solids*, 48(8). 8755-759. ISSN 0022-3697. [https://doi.org/10.1016/0022-3697\(87\)90072-2](https://doi.org/10.1016/0022-3697(87)90072-2).
3. Voron'ko, Y.K., Sobol', A.A., Shukshin, V.E. et al. (2009). Raman spectroscopic study of structural disordering in YVO₄, GdVO₄, and CaWO₄ crystals. *Phys. Solid State* 51, 1886–1893. <https://doi.org/10.1134/S1063783409090200>.
4. Manjon, Francisco Javier & Rodriguez, Placida & Munoz, Alfonso & Romero, A.H. & Errandonea, D. & Syassen, K.. (2010). Lattice dynamics of YVO₄ at high pressures. *Physical Review B*. 81. <http://doi.org/10.1103/PhysRevB.81.075202>.
5. S. Erdei, B.M. Jin, F.W. Ainger. (1997). UV absorption edge position for characterization of YVO₄ crystals growth by Czochralski and TSSG techniques, *Journal of Crystal Growth*, 174(1–4). 328-330, ISSN 0022-0248. [https://doi.org/10.1016/S0022-0248\(97\)80016-4](https://doi.org/10.1016/S0022-0248(97)80016-4).
6. Yutaka Fujimoto, Takayuki Yanagida, Yuui Yokota, Valery Chani, Vladimir V. Kochurikhin, Akira Yoshikawa. (2011). Comparative study of optical and scintillation properties of YVO₄, (Lu_{0.5}Y_{0.5})VO₄, and LuVO₄ single crystals, *Nuclear Instruments and Methods in Physics Research Section A: Accelerators, Spectrometers, Detectors and*

Associated Equipment 635(1) 53-56, ISSN 0168-9002, <https://doi.org/10.1016/j.nima.2011.01.044>.

CHAPTER EIGHT

1. A.V. Syuy, N.V. Sidorov, M.N. Palatnikov, N.A. Teplyakova, D.S. Shtarev, N.N. Prokopiv. (2018). Optical properties of lithium niobate crystals. *Optik*, 156, 239-246, ISSN 0030-4026, <https://doi.org/10.1016/j.ijleo.2017.10.136>.
2. V.V. Galutskiy, S.S. Ivashko, E.V. Stroganova. (2020). Growth of lithium niobate and potassium niobate single crystals using the Czochralski method with liquid and ceramic charging. *Solid State Sciences* 108, 106-355, ISSN 1293-2558, <https://doi.org/10.1016/j.solidstatesciences.2020.106355>.
3. J. Castillo-Torres. (2013). Optical absorption edge analysis for zinc-doped lithium niobate, *Optics Communications*, 290, 107-109, ISSN 0030-4018, <https://doi.org/10.1016/j.optcom.2012.10.067>.
4. G. Blasse, L.G.J. De Haart. (1986). The nature of the luminescence of niobates MNbo₃ (M = Li, Na, K). *Materials Chemistry and Physics*, 14(5), 481-484, ISSN 0254-0584. [https://doi.org/10.1016/0254-0584\(86\)90050](https://doi.org/10.1016/0254-0584(86)90050).
5. Bollmann, W., & Gernand, M. (1972). On the disorder of Linbo₃ Crystals. *Physica Status Solidi A*, 9(1), 301–308. <https://doi.org/10.1002/pssa.2210090136>.